Check for updates

Journal of
Materials Chemistry A

Materials for energy and sustainability

rsc.li/materials-a

Volume 6
Number 12
28 March 2018
Pages 4883-5230

ROYAL SOCIETY
OF CHEMISTRY

COMMUNICATION
Zhenhai Wen *et al.*
An electrochemically neutralized energy-assisted low-cost
acid-alkaline electrolyzer for energy-saving electrolysis
hydrogen generation

ISSN 2050-7488

This is an Accepted Manuscript, which has been through the Royal Society of Chemistry peer review process and has been accepted for publication.

Accepted Manuscripts are published online shortly after acceptance, before technical editing, formatting and proof reading. Using this free service, authors can make their results available to the community, in citable form, before we publish the edited article. We will replace this Accepted Manuscript with the edited and formatted Advance Article as soon as it is available.

You can find more information about Accepted Manuscripts in the Information for Authors.

Please note that technical editing may introduce minor changes to the text and/or graphics, which may alter content. The journal's standard Terms & Conditions and the Ethical guidelines still apply. In no event shall the Royal Society of Chemistry be held responsible for any errors or omissions in this Accepted Manuscript or any consequences arising from the use of any information it contains.

ROYAL SOCIETY
OF CHEMISTRY

rsc.li/materials-a

1 **Recent Advances in Two-Dimensional Nanomaterials for**

2 **Photocatalytic Reduction of CO_2: Insights into Performance, Theories**

3 **and Perspective**

4 Deyu Qin[a,b], Yin Zhou[a,b], Wenjun Wang[a,b], Chen Zhang[a,b,*], Guangming Zeng[a,b,*],

5 Danlian Huang[a,b], Longlu Wang[c], Han Wang[a,b], Yang Yang[a,b], Lei Lei[a,b], Sha Chen[a,b],

6 Donghui He[a,b]

7 *a. College of Environmental Science and Engineering, Hunan University, Changsha*

8 *410082, P.R. China*

9 *b. Key Laboratory of Environmental Biology and Pollution Control (Hunan University),*

10 *Ministry of Education, Changsha 410082, P.R. China*

11 *c. College of Electronic and Optical Engineering & College of Microelectronics,*

12 *Nanjing University of Posts and Telecommunications, Nanjing, 210023, P.R. China*

13

---

*Corresponding author: College of Environmental Science and Engineering, Hunan University,

Changsha, Hunan 410082, China.

E-mail addresses: *zhangchen@hnu.edu.cn (C. Zhang),*

zgming@hnu.edu.cn (G. M. Zeng).

14 **Contents**

Journal of Materials Chemistry A Accepted Manuscript

46 **Abstract**

47   Global warming and energy shortage are two major stumbling blocks on the road

48 of human social progress, and gradually arouse people's sense of crisis. Artificial

49 photosynthesis is a two-pronged solution to both problems. However, due to the harsh

50 reaction conditions and low efficiency, traditional semiconductors cannot be satisfied.

51 Two-dimensional (2D) materials with larger specific surface areas, lower carrier

52 migration distances, more active surface atoms, and higher elastic strain tolerance, play

53 a critical role in the solar to chemical energy conversion scheme, and provide a novel

54 methodology for the synthesis of fine chemicals. This review details the principles of

55 photocatalytic reduction of CO_2, and highlights the reduction pathways and product

56 selectivity via experimental methods and theoretical calculations. The state-of-the-art

57 achievements of 2D materials in the field of photocatalytic reduction of CO_2 are

58 summarized, mainly including material structure, characteristics, and modification

59 strategies to improve the performance of CO_2 reduction. And the research on the

60 combination of 2D materials and single atoms is emphasized. Moreover, bottlenecks

61 and challenges in the design and application of 2D materials, as well as prospects of the

62 future development direction, will be highlighted in order to seek new breakthroughs

63 by exploring new materials design solutions.

1. Introduction

65

66   Global warming has plagued humans for many years, and CO_2, as the main

67   greenhouse gas, is the main factor leading to global warming. In February 2019, the

68   concentration of CO_2 in the atmosphere was 410.6 PPM (parts per million). According

69   to the Intergovernmental Panel on Climate Change (IPCC), the concentration of CO_2

70   will reach 590 PPM by the end of the 21st century, and the temperature of the earth will

71   rise by 1.9℃.[1] The main source of CO_2 gas in the earth is the combustion of fossil fuels,

72   which accounts for 40% of the total anthropogenic carbon emissions.[2-4] Developing

73   new energy technologies is conducive to the vigorous development of optimization

74   tools for energy and pollution issues, such as wind energy, hydropower, and nuclear

75   energy, but these new energy sources presently cannot fully replace fossil fuels. Hence,

76   the reduction of CO_2 into valuable fuels and chemicals will be a multiple efficacy

77   approach for dealing with the energy crunch and mitigating the greenhouse effect.[5, 6]

78   In nature, the way of CO_2 conversion is mainly plant photosynthesis. There are

79   also some researches on the artificial reduction of CO_2, among which the research

80   methods mainly include biological, electrochemical, and photocatalytic methods.[7-11]

81   Artificial photosynthesis and photocatalysis has been paid wide spread attention in

82   recent years with the ideal concept of harvesting and storing sustainable solar energy

83   and mimicking the natural photosynthetic process.[12] On the one hand, photocatalysis is

84   highly efficient and can reduce CO_2 to various products, including C_1 (CO, CH_3OH,

85   HCOOH, CH_4, etc.), C_2 (C_2H_4, CH_3CH_2OH, CH_3CHO, etc.), and a small amount of C_3

86   (CH_3CH_2CHO, $CH_3CH_2CH_2OH$, etc.) products. On the other hand, photocatalysis is a

87   low energy consumption process, and light energy is inexhaustible.[13] Except for

88   photocatalytic materials, there is almost no secondary pollution to the environment.[14,

89   15] The selection of photocatalyst is the core subject in the field of photocatalysis, which

90   directly determines the photocatalytic performance. In the process of photocatalytic

91   reduction of CO_2, different photocatalytic species have different photoexcitation

92   capabilities, which will lead to different reduction product yield and selectivity. In 1979,

93   Inoue and co-workers used semiconductors WO_3, TiO_2, ZnO, CdS, GaP, and SiC

94   powders to photoelectrocatalytic reduction of CO_2 to form organic matter for the first

95   time.[16] Since then, various photocatalysts are used in the study of CO_2 reduction. TiO_2

96   has been a major research object for a long time, and various methods have been used

97   to make up for the inherent energy band structure and photoelectric performance defects

98   of TiO_2 materials.[17-19] With further research, many new materials have begun to emerge

99   in the field of photocatalysis, such as Ag_3PO_4, CdS, ZnO, etc.[20-23] But it is worth noting

100   that there is no perfect photocatalyst, the photocatalytic activity may be limited by poor

101   visible light utilization, low specific surface area, carrier recombination and low

102   photocatalytic efficiency.

103   In 2004, with the successful separation of graphene by Novoselov and Geim, the

104   application of 2D materials attracted widespread attention.[24] Through the analysis of

105　data from Web of Science, there is a rapid growth of publications on the research of 2D

106　materials in the field of photocatalytic reduction of CO_2 (Fig. 1). The 2D materials are

107　defined as a free-form crystal with a plane size of more than 100 nm and a thickness of

108　only one or a few atomic layers.[25] 2D materials have a large specific surface area, which

109　provide many active sites.[26] In addition, the ultrathin thickness of 2D materials reduces

110　the distance that photogenerated carriers reach the surface of the material, thereby

111　greatly inhibiting the recombination of charge carriers.[27] Moreover, reducing the

112　dimension of the material can change the energy band structure. By adjusting the

113　positions of the conduction band (CB) and the valence band (VB), the visible light

114　response and photocatalytic performance of the material can be improved. It is worth

115　noting that 2D materials often have a higher elastic strain tolerance, thus, the energy

116　band structure of materials can also be effectively adjusted by elastic strain

117　engineering.[28] Besides, during the formation of some 2D materials, terminating groups

118　or dangling bonds will be formed on the surface, which is conducive to the adsorption

119　of CO_2 molecules by the material, thereby effectively improving the yield of chemical

120　products.[29, 30] Therefore, 2D materials has huge application potential in the field of

121　photoreduction of CO_2.

122
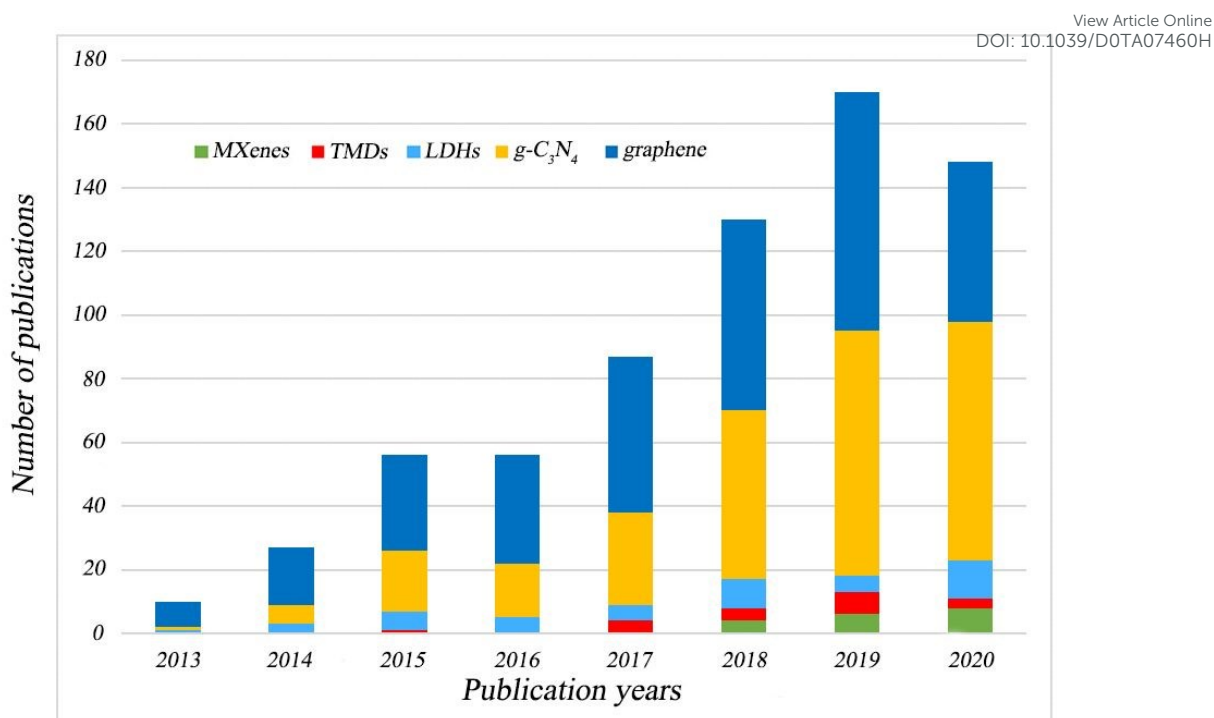
Fig. 1. Publications per year about typical 2D materials in the field of photocatalytic reduction of CO₂. The data are based on the search results from Web of Science (September, 2020).

Although some literature has been published in this field,[31-33] the introduction of 2D materials is not comprehensive or fails to focus on the application research of photocatalytic reduction of CO_2. At the same time, they often underestimate the introduction of CO_2 photoreduction theory and product selectivity, the elaboration of the reduction mechanism is not thorough and complete. In addition, as an important theoretical research tool, density functional theory (DFT) deserves further elaboration, this is rarely mentioned in previously published reviews. Therefore, we presented a critical review about the recent advances in 2D materials for CO_2 photoreduction and related theories. Herein, the basic principles of CO_2 photoreduction are introduced,

135   including the basic steps of photocatalysis, the conditions required for CO_2

136   photocatalysis and the challenges it faces. After that, this review highlights the main

137   pathways of CO_2 reduction, product selectivity, and DFT calculations. Then, several

138   typical 2D materials (such as MXenes, layered double hydroxides (LDHs), transition

139   metal dichalcogenides (TMDs), graphene, etc.) are summarized, including their

140   structures, properties, and applications in CO_2 photocatalytic reduction. The research

141   progress of 2D materials as single-atom carriers is emphasized. This review also

142   enumerates some methods to improve the photocatalytic performance of materials,

143   which includes elemental doping, morphology control, vacancy engineering, and

144   heterojunction engineering. In the last part, based on its current status, the conclusions

145   and perspectives of development in this field are introduced.

2. Basic principles of CO_2 photoreduction

147   The essence of CO_2 photoreduction is the energy conversion process, in which

148   solar energy is converted into chemical energy by photocatalyst and stored in various

149   photocatalytic products. This process involves three crucial steps: (i) The photocatalyst

150   absorbs photons with energy greater than or equal to the bandgap energy, and charge

151   carriers generate; (ii) The photogenerated carriers separate and transfer from the interior

152   to the surface of the photocatalyst; (iii) The photogenerated electrons reduce CO_2 into

153   value-added fuels and chemicals, and holes oxidize sacrificial reagents.[30, 34] After the

154   above three steps, the reduction products of CO_2 are desorbed from the surface of the

155   photocatalyst to facilitate subsequent reaction (Fig. 2).

156
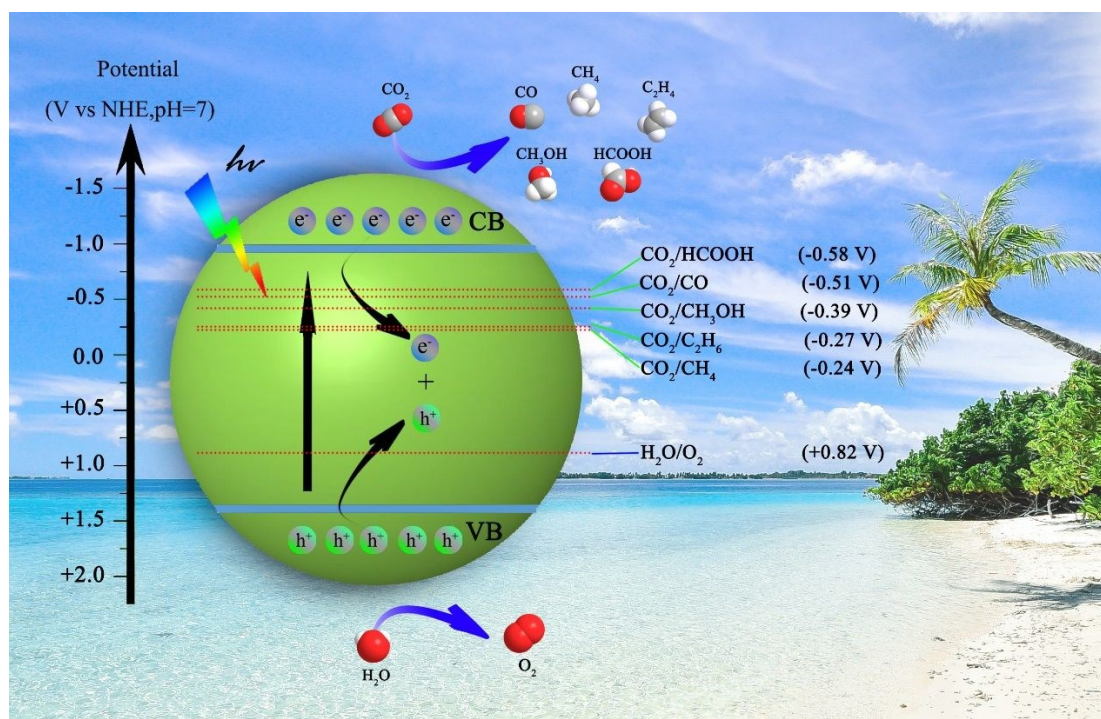
157   **Fig. 2. The schematic diagram of photocatalytic reduction of CO$_2$ with H$_2$O.**

158   In the third step above, the reduction of CO$_2$ with H$_2$O is a very complicated

159   process, which is generally considered to involve two mechanisms. The first

160   mechanism involves the single electron transfer process. Single electron activates CO$_2$

161   molecules, leading to the formation of CO$_2$*$^-$ intermediates.[35] This process requires a

162   negative equilibrium potential of -1.9 V versus normal hydrogen electrode (NHE). The

163   band structure of many semiconductor materials does not meet the requirements,[36, 37]

164   and there is not enough driving force to perform this single electron transfer process,

165   so this process is thermodynamic unfavorable. In addition, there is large recombination

166   energy between the linear CO$_2$ molecule and the CO$_2$*$^-$ radical anion, therefore this step

167 is generally considered to be a rate-limiting step. In addition to this mechanism, another

168 route is a multiple proton-coupled electron transfer process that bypasses the formation

169 of CO_2^{*-} intermediates.[16] As the number of transferred electrons and protons increases,

170 different reduction products are formed, such as CO, HCOOH, HCHO, CH_3OH, CH_4,

171 etc. (Table 1). For the formation process of multi-carbon products (CH_3CH_2OH, C_2H_6,

172 C_2H_4, etc.), in addition to the supply of electrons and protons, the difficulty of C-C

173 coupling is a more important factor restricting product yield and selectivity. In order to

174 form multi-carbon products, stable intermediates must be guaranteed to participate in

175 C-C coupling reactions.[38, 39]

176 **Table 1. Possible products of carbon dioxide and water reduction and the**

177 **corresponding reduction potential (versus NHE at pH 7 in aqueous solution) [30, 31,**

178 **40].**

Product	Reaction	E^0 (V $vs.$ NHE)	Equation
Hydrogen	$2\ H_2O + 2\ e^- \rightarrow 2\ OH^- + H_2$	-0.41	(1)
Carbon monoxide	$CO_2 + 2\ H^+ + 2\ e^- \rightarrow CO + H_2O$	-0.51	(2)
Formic acid	$CO_2 + 2\ H^+ + 2\ e^- \rightarrow HCOOH$	-0.58	(3)
Oxalic acid	$2\ CO_2 + 2\ H^+ + 2\ e^- \rightarrow H_2C_2O_4$	-0.87	(4)
Methanol	$CO_2 + 6\ H^+ + 6\ e^- \rightarrow CH_3OH + H_2O$	-0.39	(5)
Methane	$CO_2 + 8\ H^+ + 8\ e^- \rightarrow CH_4 + 2\ H_2O$	-0.24	(6)
Ethanol	$2\ CO_2 + 12\ H^+ + 12\ e^- \rightarrow C_2H_5OH + 3\ H_2O$	-0.33	(7)

| Ethane | $2\ CO_2 + 14\ H^+ + 14\ e^- \rightarrow C_2H_6 + 4\ H_2O$ | -0.27 | (8) |
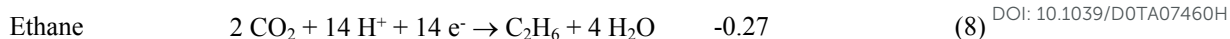
179   It is worth noting that in addition to the above CO_2 reduction mechanism, the

180   situation will be different when CO_2 is reduced by H_2 and CH_4 (Table 2).[41] Through the

181   reverse water gas shift reaction, CO_2 can be reduced to CO by H_2. There are two

182   mechanisms involved in the conversion of CO_2 to CO. One mechanism is that hydrogen

183   does not participate in the formation reaction of intermediates, but only acts as a

184   reducing agent. Another mechanism is that formate acts as an intermediate.[42] The

185   process of converting CO_2 and H_2 into CH_4 is called the Sabatier reaction. Whether CO

186   acts as an intermediate in this reaction determines two different reduction mechanisms.

187   The mechanism of the hydrogenation of CO_2 to CH_3OH is similar to that of CO_2

188   methanation.[43] On the one hand, CO_2 can be converted to CO first, and then CO can be

189   converted to CH_3OH. On the other hand, the entire process can also be without the

190   participation of CO. Moreover, CH_4 and CO_2 can react to form a mixture of CO and

191   H_2, a process known as a dry reforming of methane.[44] CH_4 is first decomposed into C

192   and H_2, and then C and O combine to form CO.

193   **Table 2. The reaction process in which CO_2 is reduced by H_2 and CH_4 and the**

194   **required $\Delta H_{298\ K}$ (kJ mol^{-1}).[45]**

Reaction	$\Delta H_{298\ K}$ (kJ mol^{-1})	Equation
$CO_2 + H_2 \rightarrow CO + H_2O$	41.2	(9)
$CO_2 + 4\ H_2 \rightarrow CH_4 + 2\ H_2O$	-252.9	(10)

$$CO_2 + 3 H_2 \rightarrow CH_3OH + H_2O \qquad -49.5 \qquad (11)$$

$$CO_2 + CH_4 \rightarrow 2 CO + 2 H_2 \qquad 247 \qquad (12)$$

195   Reducing CO_2 to valuable chemicals is a challenging process, and the challenges

196   are mainly reflected in the yield and selectivity of the product. Firstly, the dissociation

197   energy of C=O is higher than 750 kJ mol^{-1}, so CO_2 molecule is extremely stable in

198   thermodynamics. The conversion of CO_2 molecules requires a large amount of energy

199   input. Secondly, competing hydrogen evolution reaction (HER) may occur when water

200   is used as a reducing agent, and this process will consume H^+ and electrons to produce

201   H_2. It is worth noting that CO_2 has low solubility in water, so the reduction of water to

202   H_2 is more likely to occur than the reduction of CO_2, which will greatly reduce the

203   production of hydrocarbons. Thirdly, the carbon atom in CO_2 is at the highest oxidation

204   state, therefore, various products are formed during the CO_2 reduction process.

205   Thermodynamically, CO_2 tends to be reduced to methanol and methane due to less

206   potential energy required, in terms of kinetics, CO_2 is more inclined to be reduced to

207   CO and formic acid due to the lower number of electrons required.[46-48]

208   In order to effectively carry out the reduction of CO_2, the following conditions

209   must be satisfied. Photocatalyst must have appropriate band structure. On the one hand,

210   band position of the photocatalyst needs to match the potential required for CO_2

211   reduction. The CB edge potential is more negative than the reduction potential required

212   for CO_2 reduction, and the VB edge potential is more positive than the oxidation

213   potential of reducing agent. On the other hand, wider bandgap tends to imply a lower

214   visible light absorption range. Thus, the bandgap should be as close as possible to the

215   potential required for the redox reaction. For the photocatalytic reduction of carbon

216   dioxide, the ideal band gap of a photocatalyst is 1.75~3.0 eV.[32] The large amount of

217   CO_2 adsorption on the material is the basis for achieving excellent photocatalytic

218   reduction performance. When enough CO_2 molecules are adsorbed on the surface of

219   the photocatalyst, photogenerated electrons and CO_2 can be combined quickly to reduce

220   the recombination of carriers, thus obtaining a higher yield. The surface area and

221   surface energy of materials are important factors affecting the adsorption of CO_2

222   molecules. A larger surface area can provide more adsorption sites and accommodate

223   more CO_2 molecules. The surface energy of the material can be changed by adjusting

224   the chemical properties of the surface or exposing the high-energy facets.[34] In addition,

225   photogenerated electrons and holes should be rapidly transferred to the surface of the

226   material, thus reducing the recombination rate. Photogenerated electrons and holes

227   can recombine in just 10^{-9} s, whereas redox reaction time is generally between 10^{-8} s -

228   10^{-3} s,[49] so it is necessary to take appropriate measures to reduce carrier recombination.

229   Finally, the reduced products should be easily desorbed from the photocatalyst to

230   facilitate subsequent adsorption of the reactants. On the one hand, the products occupy

231   the adsorption space of the reactants, and on the other hand, the products adsorbed on

232   the surface may undergo side reactions.

233   After a series of reaction conditions are suitable, CO_2 molecules will undergo a

234   complex reduction process under the catalysis of the photocatalyst. During the

235   reduction process, different products, by-products and intermediates will be generated.

236   Therefore, exploring the reduction pathways of CO_2 is of great significance to control

237   the yield and selectivity of the target product.

238   3. Possible reaction pathways and product selectivity

239   3.1 CO_2 adsorption modes

240   The adsorption and activation of CO_2 molecules are the core steps in the whole

241   reduction process. The adsorption of CO_2 molecules on the photocatalyst surface is an

242   essential initial step in this process. As a linear molecule, CO_2 can be physiosorbed on

243   the photocatalyst surface, but in the subsequent activation process, the chemical

244   adsorption of CO_2 molecules is more important.[30] There are three main coordination

245   modes of CO_2 molecules on the surface of photocatalyst. Firstly, the O atom in the CO_2

246   molecule serves as an electron donor, and provides a lone pair electron to the surface

247   Lewis acid center. This method is called oxygen coordination, and there are two

248   different bidentate bonding structures (Fig. 3a). Secondly, the C atom acts as an electron

249   acceptor. When the Lewis acid takes electrons from the Lewis base center, it forms

250   something like carbonic acid. This method is called carbon coordination (Fig. 3b).

251   Thirdly, the O and C atoms in the CO_2 molecule receive and supply electrons at the

252   same time, which is called mixed coordination. This coordination also has two different

253   bidentate bonding structures (Fig. 3c).[50] It is worth noting that different coordination

254   modes will affect the formation of certain intermediates during the reduction process,

255   resulting in different reduction pathways. For example, it is well known that oxygen

256   coordination tends to form $HCOO^-$, while carbon coordination is beneficial to the

257   formation of carboxy intermediates (*COOH),[51] which affects the selectivity of the

258   products.

259
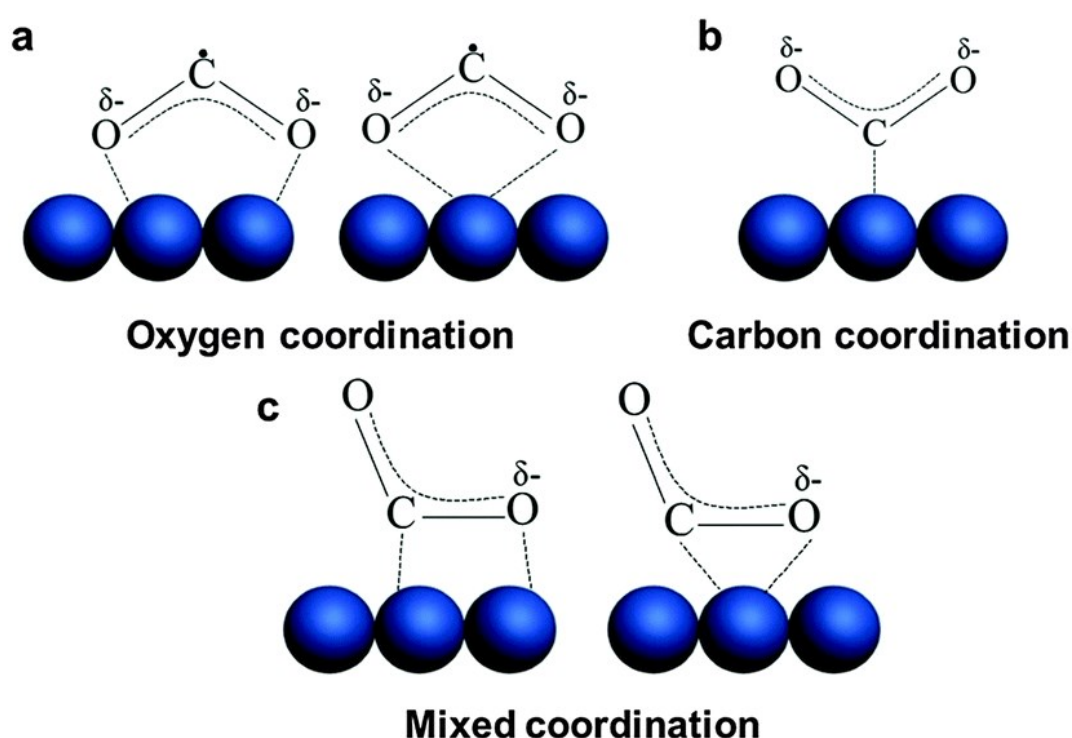
260   **Fig. 3. Schematic diagram reflects three different coordination modes of CO_2**

261   **molecule. Reproduced with permission from ref. [30]. Copyright 2016 Royal Society**

262   **of Chemistry.**

263   **3.2 Reaction pathways**

264   **3.2.1 Formation of C_1 products**

265   The formation of HCOO⁻ and HCOOH mainly involves three different pathways.

266   In the first path, CO_2 is inserted into a metal-hydrogen bond or protonated by H^+ to

267   form an intermediate. Then, the O atoms in the intermediate and the photocatalyst are

268   connected by monodentate or bidentate, and HCOOH is formed by proton-electron

269   transfer (Fig. 4a). The second path involves a CO_2^{*-} radical, which can form HCOO⁻

270   through O coordination and C coordination with the participation of HCO_3^-.[52] In

271   addition, *COOH intermediates will lead to the formation of HCOOH (Fig. 4b).[53]

272   Baruch *et al.*[54, 55] discovered the third path of CO_2 reduction by studying the mechanism

273   of CO_2 reduction by Tin electrode. The CO_2 molecule will initially react with Sn^{II}

274   oxyhydroxide to form surface-bound carbonate, and then surface-bound carbonate will

275   form HCOO⁻ through the transfer of two electrons and one proton (Fig. 4c).

276   CO formation involves an important *COOH intermediate. This intermediate

277   generates *CO through H^+/e^- transfer. Then, CO* is desorbed from the surface of the

278   material. The formation of *COOH has two different paths. One of the paths is that the

279   adsorbed CO_2 molecules generate *COOH through simple H^+/e^- transfer. In this process,

280   because the COOH binding is weak, it is not conducive to the direct conversion of CO_2

281   molecules to *COOH, so there is a second path. The CO_2 molecule is converted into

282   CO_2^{*-} radical by the reduction of single electron, and CO_2^{*-} radical receives another

283   proton to form a *COOH intermediate (Fig. 4d).[53, 55, 56]

284
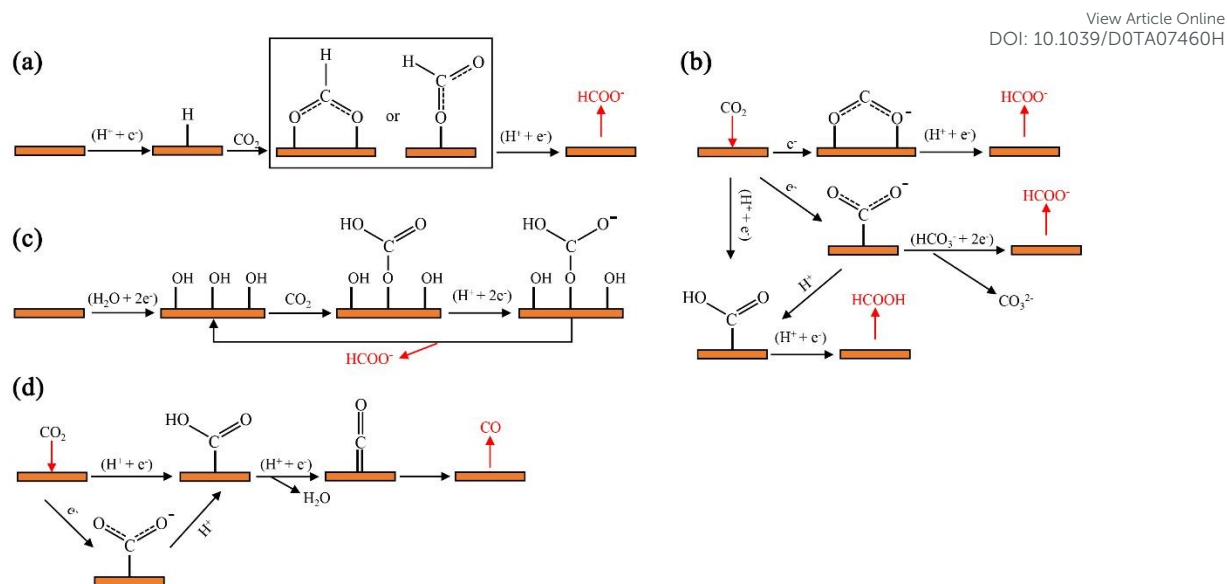
Fig. 4. (a)-(c) Possible reduction pathways for HCOOH and HCOO⁻ formation.

Reproduced with permission from ref. [53], copyright 2015 American Chemical

Society. (d) Possible reduction pathways for CO formation. Reproduced with

permission from ref. [54], copyright 2015 American Chemical Society.

285

286

287

288

289   There are many formation pathways of HCHO, CH_3OH, and CH_4. In the entire

290 reduction route, HCHO and CH_3OH can be intermediates of the final product, and can

291 also be directly desorbed as products, so the role of CH_3OH and HCHO directly affects

292 the formation of CH_4. The first path originates from *CO intermediates. The *HCO,

293 *H_2CO, and *H_3CO intermediates are gradually formed through the continuous

294 hydrogenation of *CO intermediates. The strength of the binding mode of HCHO and

295 CH_3OH determines whether the intermediate product will desorb. If the binding mode

296 of HCHO and CH_3OH is weak, it will lead to the formation of HCHO and CH_3OH.

297 Conversely, CH_4 is formed by further hydrogenation of *H_3CO (Fig. 5a).[57] The second

298   path is to convert *CO intermediate into *COH intermediate, then the combination of

299   *COH with couple of electron and proton generates important *C intermediates. As the

300   core special in this path, *C is gradually hydrogenated to generate *CH, $*CH_2$, and

301    $*CH_3$. Finally, $*CH_3$ can be combined with ·OH or H^+ to generate CH_3OH or CH_4,

302   respectively. The selectivity of CH_3OH and CH_4 depends on the oxophilicity of the

303   surface (Fig. 5b).[56] The third path is clearly different from the above two paths. This

304   path starts with CO_2*^- special. The CO_2*^- combines with couple of electron and proton

305   to generate a bidentate coordinated HCO_2* intermediate. H_2OCO* and *CHO are

306   gradually produced by hydrogenation or reduction. After that, the *CHO intermediate

307   is converted to glyoxal through the dimerization process, and the glyoxal can be further

308   hydrogenated to generate CH_2OHCHO and CH_3CHO. As the subsequent reaction

309   proceeds, the $*CH_3$ intermediate is formed, which is then converted to CH_4 by electron-

310   proton transfer (Fig. 5c).[50, 58] Recently, Ju and co-workers studied Fe-N-C single-site

311   catalysts for electrochemical reduction of CO_2, and the results showed that the reduction

312   pathway is different from the above three. This path is special because the *CHO

313   intermediate can generate $*CH_2OH$ through two-step electron-proton transfer. On the

314   one hand, $*CH_2OH$ can continue to combine with the couple of electron and proton,

315   thus releasing H_2O molecules to generate $*CH_2$, and then CH_4 is generated by two-step

316   electron-proton transfer. On the other hand, the $*CH_2OH$ intermediate can also be

317   directly hydrogenated and desorbed to form CH_3OH (Fig. 5d).[59]

318
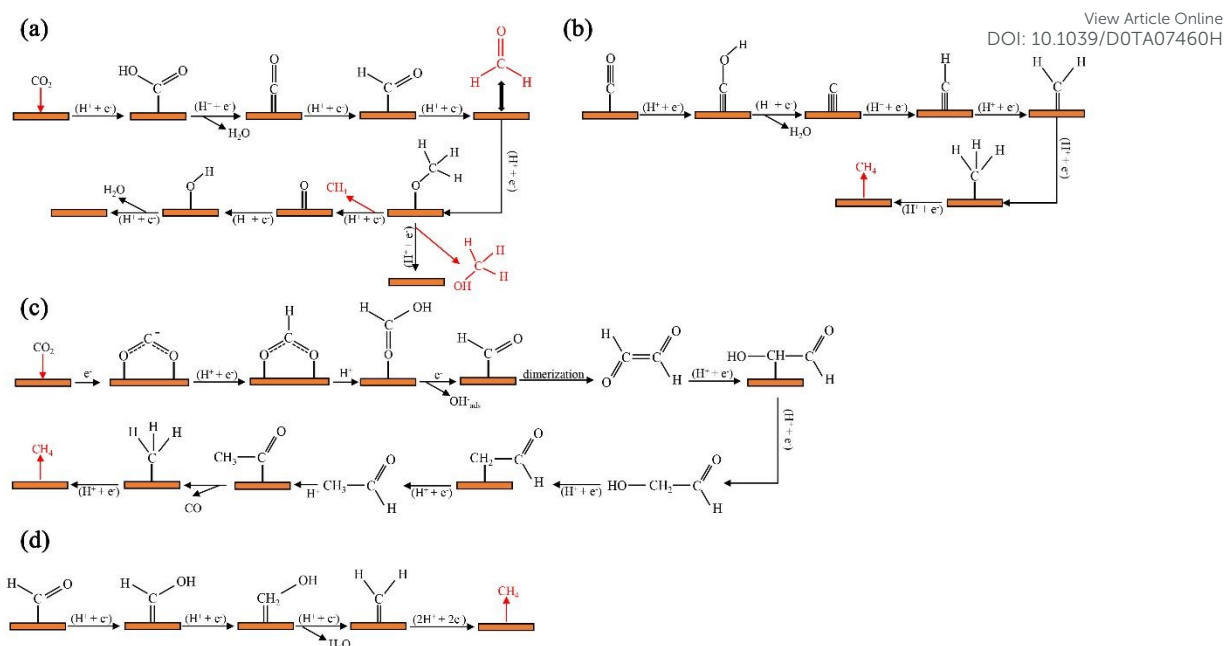
Fig. 5. Possible reduction pathways for HCHO, CH$_3$OH, and CH$_4$ formation.

Reproduced with permission from ref. [57], copyright 2010 Royal Society of

Chemistry; Reproduced with permission from ref. [56], copyright 2013 Wiley-VCH;

Reproduced with permission from ref. [58], copyright 2013 Wiley-VCH;

Reproduced with permission from ref. [59], copyright 2019 American Chemical

Society.

319

320

321

322

323

324

325   In addition to the C$_1$ pathway described above, there is a new concept called dual-

326   metal site. Dual-metal site photocatalyst has distinctive CO$_2$ coordination mode.

327   Recently, Li and co-workers introduced S vacancies in 2D CuIn$_5$S$_8$ layers (Vs-CuIn$_5$S$_8$)

328   for photocatalytic reduction of CO$_2$.[60] For CuIn$_5$S$_8$ without S vacancies, compared with

329   C-O bonds, M-C and M-O bonds were weaker and more prone to break, resulting in

330   the formation of CO and CH$_4$ after protonation (Fig. 6a). But when the S vacancies was

331   introduced, the S vacancies on the surface of CuIn$_5$S$_8$ caused low coordination

332 environment and electron accumulation around Cu and In metal atoms. The C and O

333 atoms in the CO_2 molecule were bonded to two metal sites respectively, and forming a

334 stable M-C-O-M intermediate. At this time, the M-C and M-O bonds were more

335 difficult to break, and the C atom tended to be protonated, which caused the C atom to

336 be saturated. Subsequently, the C-O and C-M bonds in the $M-CH_3-O-M$ intermediate

337 became weaker and fractured, leading to the formation of CH_4 (Fig. 6b). The selectivity

338 of CH_4 was close to 100%.

339
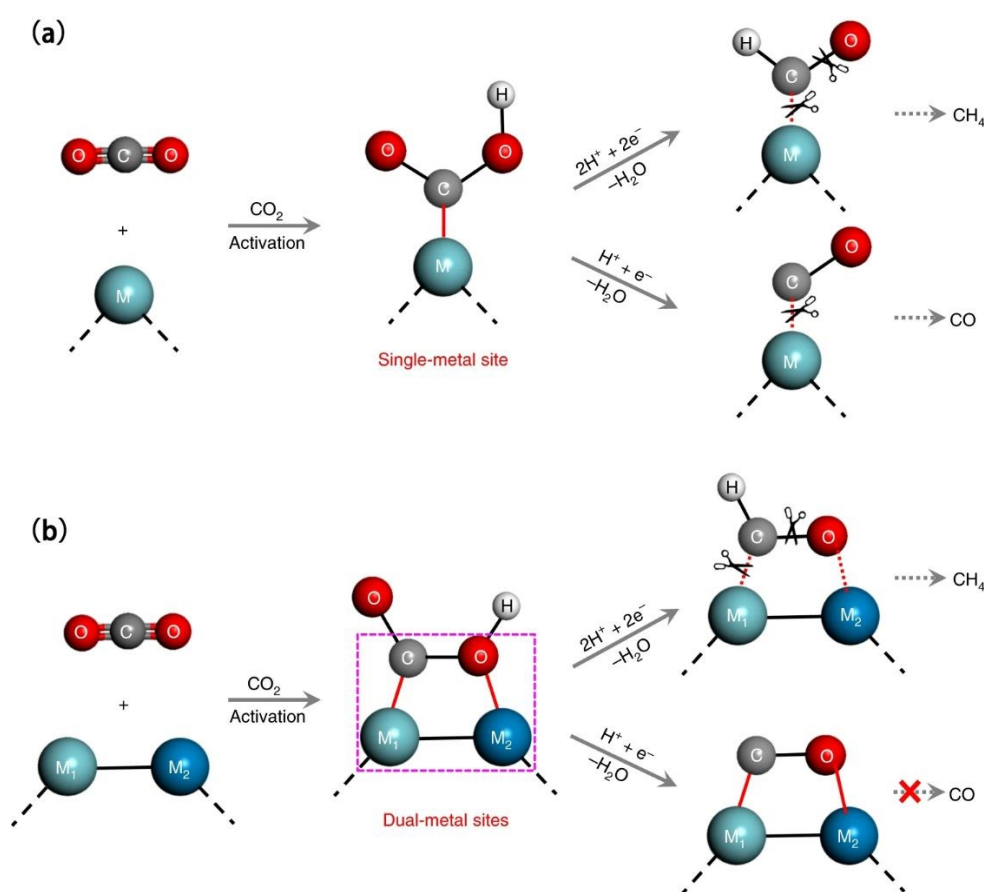
340 **Fig. 6. A reaction mechanism of photocatalytic CO_2 reduction on (a) single metal**

341 **site, and (b) dual-metal sites. Reproduced with permission from ref. [60]. Copyright**

342 **2019 Springer Nature.**

343 **3.2.2 Formation of C_2 products**

344   The reduction path of C_2 products is more complicated. Common C_2 products

345 mainly include ethanol, acetaldehyde, ethylene, acetic acid, and acetate. Garza et al.[61]

346 reported the formation pathway of C_2 products on Cu surface. In this route, *CO is first

347 converted into *CHO and *COCHO, where *COCHO plays a pivotal role in the entire

348 reduction route and determines whether the subsequent reaction follows the ethanol

349 route or the ethylene route. In the ethanol path, it can gradually hydrogenate and

350 generate glyoxal, ethylene glycol, acetaldehyde, and ethanol along the way. In the

351 ethylene pathway, in addition to the final formation of ethylene, the isomerization of

352 the *OCH_2COH intermediate will also lead to the formation of acetic acid (Fig. 7a).

353 Yoshio Hori et al.[62] summarized another reduction pathway for C_2 products. The C*

354 was converted to *CH by electron-proton transfer. After the two CH_2* were coupled,

355 C_2H_4 was formed by dimerization, or C_2H_4 was generated by CO insertion of *CH_2 (Fig.

356 7b). In addition, Yang et al.[247] discovered that the *$C_2O_2^-$ intermediates were formed in

357 two different coordination modes during the C_2 reduction process, which were

358 converted to *COCOH by hydrogenation, then converted to ethylene or acetaldehyde

359 by the transfer of five H^+/e^-, and converted to ethanol by the transfer of seven H^+/e^-

360 (Fig. 7c).[55, 63]
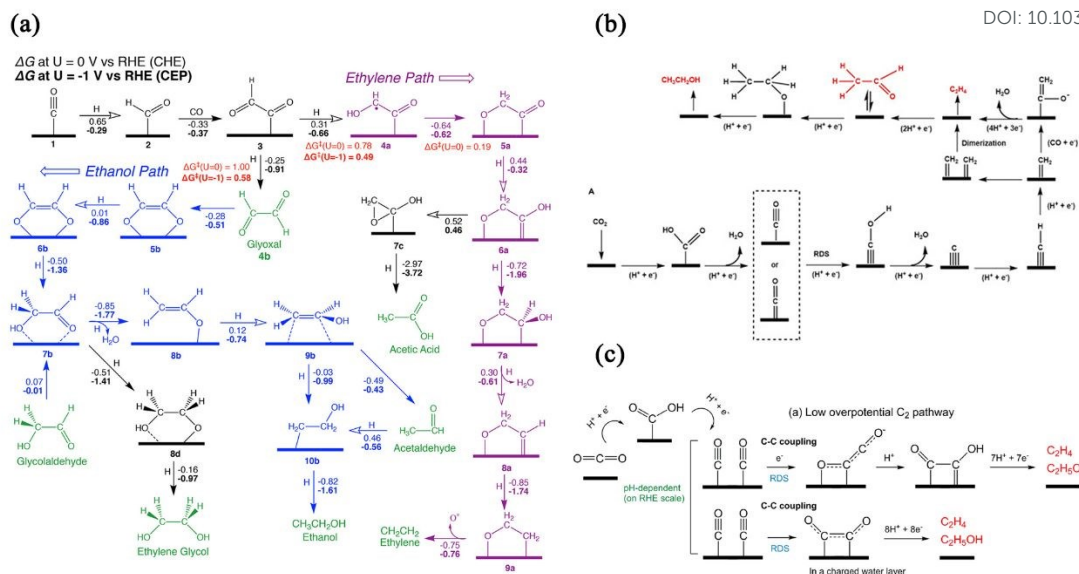
Fig. 7. Possible reduction pathways for C_2 products formation. Reproduced with permission from ref. [61], copyright 2018 American Chemical Society; Reproduced with permission from ref. [55], copyright 2017 Elsevier; Reproduced with permission from ref. [63], copyright 2017 American Chemical Society.

3.2.3 Formation of C_3 products

The production of C_3 products is more difficult than that of C_1 and C_2 products, so the research on the reduction mechanism of C_3 products is relatively less. Yoshio Hori's research found that C-C coupling between C_2 intermediates and C_1 intermediates would lead to the formation of C_3 products.[62] For example, CH_3CH^* and $^*CO$ combine to form $CH_3CH_2CO^*$ intermediates, and then through electron-proton transfer to form CH_3CH_2CHO and $CH_3CH_2CH_2OH$ (Fig. 8).[55, 62]

374
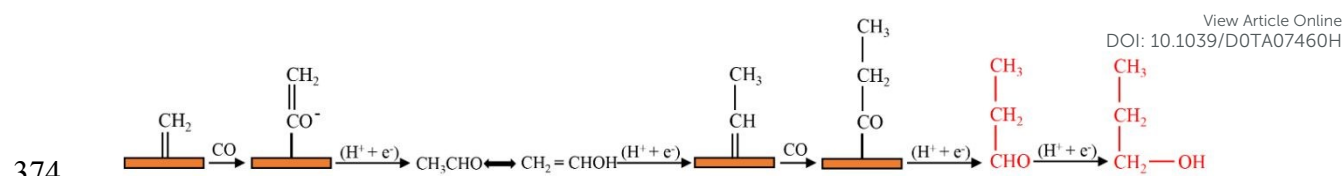
Fig. 8. Possible reduction pathways for CH₃CH₂CHO and CH₃CH₂CH₂OH

products formation. Reproduced with permission from ref. [62]. Copyright 1997

American Chemical Society.

3.3 Product selectivity

The selectivity of products has always been a hot issue in the field of CO_2 photoreduction. By effectively controlling the selectivity of the reduction product, the yield of the target product can be greatly increased, so it has the vital practical significance.[64] The selectivity of the product can be controlled from the following aspects: photoexcitation process, energy band structure of photocatalyst, supply of electrons and protons, mass transfer of CO_2, and reduction reaction.

3.3.1 Photoexcitation process

For conventional semiconductor photocatalysts, the process of generating electrons by photoexcitation is closely related to the inherent band structure of the material. Certain semiconductor materials will only be sensitive to incident light in a certain wavelength region. Therefore, it is difficult for semiconductor photocatalysts to achieve high selectivity of CO_2 photoreduction from the perspective of incident light. But the plasmonic nanoparticle photocatalyst changed this situation. Plasmonic

392   nanoparticle photocatalysts have light excitation characteristics that are significantly

393   different from semiconductor photocatalysts. Noble metal nanoparticles (such as Au,

394   Ag, Cu, etc.) will undergo localized surface plasmon resonances (LSPR) and exhibit

395   strong visible spectrum absorption. The electron oscillation induced by the plasmonic

396   relaxes to produce energetic hot electrons. Such energetic electrons can activate the

397   adsorbents on the surface of the catalyst, and the excess electrons can be used for

398   photoreduction.[65] The plasmonic nanoparticle photocatalyst makes it more feasible to

399   influence the product selectivity by controlling the light excitation process. For example,

400   in Wang's study,[66] by controlling the different wavelengths and intensities of incident

401   light, Au nanoparticles showed different selectivity for the generation of CH_4 and C_2H_6.

402   In addition, plasmon photocatalysts often form a composite system with traditional

403   semiconductor photocatalysts for the photoreduction of CO_2. Through the ingenious

404   design of the composite system, the high selectivity of the product can be achieved.

405   Zeng et al.[67] supported Au nanoparticles on photonic crystals composed of TiO_2

406   nanotubes (Au-PMTiNTs), and the CO_2 reduction products showed different selectivity

407   under different light conditions. Under the irradiation of AM1.5G simulated sunlight,

408   the CH_4 showed extremely high selectivity (89.3%). When the Au-PMTiNTs was

409   illuminated by LED light ($\lambda > 420$ nm) first and then by AM1.5G light source, CO and

410   CH_2O were the main reduction products, and CH_4 generation was not detected. The

411   reason for this phenomenon is that semiconductors and plasmons have different light

412   excitation properties. By reasonably controlling the wavelength of the incident light,

413   the electron transfer inside the composite material is changed, which in turn affects the

414   selectivity of the final product.

415   3.3.2 Energy band structure of photocatalyst

416   The band structure of the photocatalyst directly affects its redox ability. As shown

417   in Fig. 2, the different CB positions of the photocatalyst correspond to different

418   reduction potentials, and different reduction potentials thermodynamically determine

419   whether special products can be produced. Therefore, adjusting the energy band

420   structure of the photocatalyst through an appropriate method can thermodynamically

421   adjust the selectivity of the reduction product. Li et $al.$[68] loaded CdSe quantum dots

422   (QDs) on 2D polymerized C_3N_4 nanosheets for highly selective CO_2 photoreduction

423   reactions. Since the quantum confinement effect of 0D QDs can change the CB energy

424   level of the material, the CB energy level can be at an optimal position by controlling

425   the size of the QDs. When the particle size was 2.2 nm, the bottom of the CB (E_{CB}) was

426   just between the potential required to generate H_2 and CH_3OH. The energy of the CB

427   can be enough to produce CH_3OH, but not enough to produce H_2, thus effectively

428   inhibiting the HER reaction. In addition, the energy levels required to produce CO and

429   CH_4 were far away from E_{CB}, so CH_3OH, as the main product of CO_2 reduction, had a

430   selectivity of 73%. In addition to the thermodynamic selectivity, the overpotential of

431   the original material is changed by adjusting the energy level, thereby generating a

432   greater driving force in kinetics, which is also a means to promote the selectivity of

433　specific products. Xing et al.[69] used fluorination to upswept the Ti^{3+} impurity level of

434　mesoporous single crystal TiO_{2-x}. F atoms captured electrons from Ti^{3+}, and the upward

435　bending of Ti^{3+} impurity level increased the overpotential from 0.39 to 0.48 eV, which

436　drove the rapid reduction of CO to CH_4, thus improving the CH_4 selectivity kinetically.

437　The fluorination of raw materials increased the selectivity of CH_4 from 25.7% to 85.8%.

438　3.3.3 Supply of electrons and protons

439　　In the process of CO_2 photoreduction, the formation of reduction products requires

440　the constant supply of electrons and protons, and different reduction products

441　correspond to different numbers of electrons and proton consumption. The density of

442　electrons and protons on the surface of the catalyst will affect the selectivity of the

443　reduction products to a certain extent. The photocatalyst will generate photogenerated

444　electrons and holes under the irradiation of light of appropriate wavelength, and the

445　holes will oxidize the sacrificial agent to generate protons. Therefore, promoting the

446　separation of photogenerated electrons and holes can effectively increase the density of

447　surface electrons and protons. There are many strategies to promote the separation of

448　photogenerated electrons and holes, such as constructing heterojunctions,[70] loading

449　metal elements,[71] constructing electric fields,[72] and so on. For protons, in addition to

450　being restricted by the number of holes, they can also be supplemented in other ways.

451　For example, Zhao et al.[73] introduced Cu and H atoms into the lattice of Pt and used

452　the composite as a co-catalyst for C_3N_4. In the process of product formation, due to the

453   limited adsorption capacity of Pt atoms to H, the number of protons adsorbed by Pt was

454   not enough to continue the conversion of CO to CH_4. However, the H in the Pt lattice

455   diffused from the bulk to the surface of the material, and participated in the reduction

456   reaction in the form of chemical adsorption. Sufficient proton supply makes the

457   conversion of CO to CH_4 possible, thereby promoting the selectivity of CH_4. In addition

458   to the number of protons, protons need to efficiently combine with CO_2 molecules to

459   achieve high proton utilization. Only when protons bind to specific sites in the CO_2

460   molecule can the reduction reaction proceed along a specific reduction pathway. Wang

461   and co-workers loaded Pt on In_2O_3 nanorods for selective CO_2 photoreduction.[74] In

462   order to obtain CH_4 with high selectivity, the proton should bond to the C in the CO_2

463   molecule, not the O. In this reaction, protons first bonded with the coordinated

464   unsaturated O on the surface of pristine In_2O_3. The C in the CO_2 molecule must capture

465   the proton from the O on the surface of pristine In_2O_3. However, due to the lower

466   electronegativity of C, this process is difficult to occur. When Pt was loaded, the proton

467   first formed a Pt-H bond with Pt, and the electronegativity of C was higher than that of

468   Pt, so C in the CO_2 molecule can easily obtain H, which was more conducive to the

469   generation of CH_4.

470   3.3.4 Mass transfer of CO_2

471   When an aqueous solution is used as a hole sacrificial agent, the catalyst, H_2O and

472   CO_2 constitute a three-phase system. In this system, the mass transfer of CO_2 is a very

473 important step in the CO_2 reduction process. In general, if the concentration of CO_2

474 molecules on the catalyst surface is too low relative to H^+, the catalyst surface is more

475 likely to undergo HER reaction rather than CO_2 reduction reaction. Therefore,

476 promoting the mass transfer process of CO_2 molecules in aqueous solution is an

477 effective means to inhibit the HER reaction. Li et al.[75] loaded Pt on polymeric C_3N_4

478 nanosheets with a hydrophobic surface to explore the effect of CO_2 mass transfer

479 process on the HER reaction. Pt has a strong electron capture ability and HER reaction

480 promotion ability. For hydrophilic C_3N_4, only a few electrons on the photocatalyst

481 surface were used in the CO_2 reduction reaction. The selectivity of the C derivative in

482 the product was only 2.5%. Compared with the hydrophilic surface, the hydrophobic

483 surface of the C_3N_4 is more conducive to the mass transfer process of CO_2 molecules,

484 thereby increasing the concentration of CO_2 molecules adsorbed on the surface of the

485 material. In this case, the co-catalytic effect of Pt was more favorable to CO_2 reduction

486 reaction than HER, and the proportion of C derivative increased to 87.9%. Therefore,

487 the design of the photocatalyst to enhance the CO_2 mass transfer process is a very clever

488 means to inhibit the HER reaction. However, it is still difficult to improve the selectivity

489 of specific C derivatives only by controlling mass transfer of CO_2.

490 3.3.5 Reduction reaction

491 After light excitation and photogenerated carrier transfer, CO_2 molecules will be

492 adsorbed by the photocatalyst and then reduced along a specific reaction pathway. In

493 this process, various energies and chemical bonds are involved, which makes the whole

494 process quite complicated. However, through reasonable regulation of some factors in

495 this complex process, the selectivity of the product can be controlled to a certain extent.

496 The coordination between the CO_2 molecule and the catalyst is the starting point of the

497 entire reaction pathway. Different coordination modes will affect the formation of

498 various products in the subsequent reduction process. Yang et al.[76] introduced O

499 vacancies in Bi_2MoO_6 so that CO_2 molecules formed a new adsorption mode on its

500 surface. In the presence of O vacancies, the C atoms in CO_2 molecules bonded to the O

501 site on the material surface, and the two O atoms in CO_2 molecules bonded to the two

502 surface Bi atoms. For the pristine Bi_2MoO_6, CO_2 molecules were more likely to bond

503 with O atom and single Bi atom on the surface. Therefore, the new coordination mode

504 introduced by the O vacancy made the adsorption of CO_2 on the material more stable.

505 Under the influence of this special coordination mode, the conversion of CO* to *CHO

506 was more thermodynamically feasible, which in turn facilitated the formation of CH_4.

507 In a complete reduction pathway, many different intermediates are involved. The

508 adsorption capacity of the photocatalyst to the intermediate affects whether the

509 subsequent hydrogenation reaction can proceed. If the interaction between the

510 intermediate and the photocatalyst is weak, the intermediate will be desorbed from the

511 photocatalyst surface as a by-product. It is a method to enhance the selectivity of a

512 particular product by reasonably designing the material to change its adsorption

513 capacity to an intermediate. Liu and colleagues successfully synthesized highly

514 graphitized carbon dots containing nitrogen groups (GCDs).[77] In the CO_2

515 photoreduction experiment, GCDs showed 74.8% electronic selectivity of CH_4. The

516 nitrogen-containing groups on the surface of GCDs can produce strong chemical

517 adsorption to the *CO intermediate, thereby preventing the desorption of the

518 intermediate and inhibiting the formation of CO products. The *CO intermediate can

519 be further reduced to CH_4. For amorphous carbon dots (ACDs), *CO intermediate was

520 more likely to desorption on the surface due to their lack of strong chemical adsorption

521 capacity for *CO intermediates. The reduction of CO_2 is a multi-step reaction process,

522 and the formation of each intermediate corresponds to the different energy barrier.

523 Therefore, the selectivity of the product can be controlled by lowering the energy

524 barrier. Tan $et\ al.$[78] increased the metal and hydroxyl defects in Ni Al-LDH by reducing

525 the thickness of the material. In the process of CO_2 reduction by using Ni Al-LDH

526 without defects as a photocatalyst, the conversion of $*CH_3$ to CH_4 was a potential-

527 determining step for the formation of CH_4, and the introduction of hydroxyl defects

528 reduced the energy barrier of this step from 0.486 eV to 0.329 eV. In addition, the Gibbs

529 free energy barrier decreased from 0.329 eV to 0.127 eV and 0.163 eV after the Ni

530 vacancy and Al vacancy were introduced. The lower Gibbs free energy barrier is more

531 conducive to the formation of CH_4. Under suitable defect conditions, the optimal

532 selectivity of CH_4 reached 70.3%. The formation of various intermediates involves the

533 formation and breaking of various chemical bonds. In some cases, photocatalysts can

534 break certain chemical bonds, thus affecting the selectivity of products. Ouyang $et\ al.$[79]

535   synthesized dinuclear cobalt complex $[Co_2(OH)L^1](ClO_4)_3$ for CO_2 photoreduction.

536   After a series of reduction reaction steps, the $[L^1Co^{II}Co^{II}(COOH)]^{3+}$ intermediate was

537   generated. Under the action of the photocatalyst, the C-OH bond in this intermediate

538   was broken. One Co in the dinuclear cobalt complex was bonded to CO, and the other

539   Co was bonded to OH^-. After that, CO was released from the intermediate, and the

540   selectivity can reach 98%. During the formation of CO, the cleavage of C-OH is a rate

541   limiting step. Therefore, the photocatalyst promotes the cleavage of C-OH, which

542   means that it promotes the conversion of CO_2 to CO.

543   In short, through different coordination modes and reaction pathways, CO_2 will be

544   reduced to different intermediates and final products. Through the in-depth study of

545   CO_2 reduction pathways, the high selectivity of target products should be controllable

546   in the future. In the process of studying the reduction pathways and product selectivity,

547   experimental research and theoretical calculation are two indispensable methods, while

548   DFT is an irreplaceable theoretical calculation method at present.

549   ## 4. DFT calculation of CO_2 photoreduction

550   DFT was proposed by Hohenberg and Kohn in 1964 to study the ground state

551   properties of multi-particle systems.[80] The DFT originated from the Thomas-Fermi

552   model proposed by Thomas and Fermi in 1927, which explicitly expressed the electron

553   kinetic energy in the form of electron density for the first time, but this model is

554   relatively crude. In DFT, because there are too many wave function variables in the

555   multi-electron system, the wave function is not taken as the basic variable in the

556   research process, and the electron density ρ (r) is directly studied, which greatly reduces

557   the computational difficulty of the molecular electron structure. In the study of

558   photocatalytic reduction of CO_2, DFT has become one of the most commonly used and

559   necessary calculation methods. The DFT calculation can help us better understand the

560   electronic excitation process, energy band structure, adsorption energy (Ea), defects of

561   the photocatalytic material, and so on. In particular, through the calculation, the

562   possible complete path of CO_2 reduction can be analyzed clearly.

563   DFT calculations can help us analyze the relationship between material

564   microstructure and performance. For example, the doping site of a material can be

565   studied by calculating the formation energy. In the study of CO_2 photoreduction by S-

566   doped graphitic C_3N_4 (g-C_3N_4) nanosheet, Wang and co-workers verified the doping

567   site of S element by DFT calculation.[81] There were three different doping sites, namely

568   N_{Cen}, N_{Aro}, and N_{Tet}. Among them, three heptazine rings in g-C_3N_4 were connected to

569   the N_{Tet} site, which can be ignored. N_{Cen} and N_{Aro} were connected to the C atom with a

570   3-fold coordination and a 2-fold coordination, respectively. In order to identify the

571   possible doping sites, the formation energy (E_{form}) of the two sites was calculated. The

572   formation energy of N_{Cen} and N_{Aro} sites was -1.59 eV and -2.98 eV, respectively. It can

573   be seen that the doping of N_{Aro} site was more stable, so the doping of N_{Aro} site was

574   considered as the doping mode of the catalyst. In addition to doped sites, vacancies are

575   common research objects, and DFT calculations can also be used to study the effect of

576   material vacancies on material properties. Yang *et al.*[82] studied the effect of O vacancies

577   on the performance of Bi_2MoO_6 photocatalytic reduction of CO_2. After comparing the

578   band structure and density of state (DOS) of Bi_2MoO_6 and Bi_2MoO_6-OVs, they found

579   that an intermediate band appeared in the energy gap of Bi_2MoO_6-OVs, and this

580   intermediate band promoted the transfer of photogenerated carriers. In addition, the

581   influence of O vacancies on the adsorption performance of the materials was

582   determined by calculating the adsorption energy and the electron density on the surfaces

583   of the two materials. The calculation results showed that the adsorption of CO_2

584   molecules by Bi_2MoO_6-OVs was more stable, and O vacancies played a significant role

585   in the adsorption process. In the above studies, the adsorption energy is an important

586   evaluation index to evaluate the relationship between the adsorption property and

587   vacancy of materials, which can also be used to study the relationship between the

588   thickness of materials and the adsorption capacity. For example, Chen *et al.*[83] calculated

589   that the adsorption energy of the bulk Co_3O_4 and the monolayer Co_3O_4 for CO_2

590   molecules were -0.13 eV and -0.27 eV, respectively. The more negative Ea, the stronger

591   the adsorption capacity, so the single-layer Co_3O_4 has stronger CO_2 adsorption ability.

592   Besides, they also calculated that the adsorption energies of bulk Co_3O_4 and monolayer

593   Co_3O_4 to H atoms were -0.16 eV and -0.10 eV, respectively, thereby further indicating

594   the adsorption selectivity of monolayer Co_3O_4 for CO_2 molecule.

595   DFT calculation can also be used to analyze the electronic structure of the material.

596   Saeedeh S. Tafreshi and co-workers successfully synthesized Ag_3PO_4 (111)/g-C_3N_4

597   complex and used it in the study of CO_2 photoreduction.[84] They analyzed the electronic

598   structure of Ag_3PO_4 (111)/g-C_3N_4 through total DOS (TDOS) and projected DOS

599   (PDOS) calculations. The compound's valence band maximum (VBM) and conduction

600   band minimum (CBM) were occupied by different atomic orbits. As can be seen from

601   the Fig. 9a, the CBM of the composite material was mainly dominated by the atomic

602   orbital of g-C_3N_4, while the VBM was mainly dominated by the atomic orbital of

603   Ag_3PO_4 (111). And then from fig. 9b and 9c, we can see that VBM was mainly occupied

604   by O (p) and Ag (d) orbitals in Ag_3PO_4 (111). CBM was mainly occupied by C (p) and

605   N (p) orbitals in g-C_3N_4, while O (p) and Ag (d) also occupied a part. The band gap of

606   hybrid materials decreased from 2.75 eV of Ag_3PO_4 (111) and 3.13 eV of g-C_3N_4 to

607   about 2.52 eV, which enhanced the photocatalytic activity of materials in the visible

608   region. In addition, for the Ag_3PO_4/Ag/g-C_3N_4 complex, the total DOS and energy

609   bands were further studied and the existence of the midgap was found, thereby

610   confirming the existence of Ag at the interface of Ag_3PO_4 and g-C_3N_4. Through PDOS

611   analysis, the formation of midgap state was mainly the result of the combined action of

612   the Ag, O, C, and N atoms (Fig. 9d-9i). Moreover, DFT calculation can also be used to

613   elucidate the electron excitation process during photoreduction of CO_2. Lu et al.[85]

614   successfully synthesized porphyrin-tetrathiafulvalene covalent organic frameworks

615   (TTCOF-M, M=2H, Zn, Ni, Cu). Electric-deficient metalloporphyrin (TAPP) was

616   covalently coupled with electron-rich tetrathiafulvalene (TTF) within COFs. They

617   elaborated the transfer process of photogenerated carriers through DFT calculation. In

618   the electronic structure of the photocatalyst, HOMO was dominated by the TTF portion,

619   and LUMO was dominated by the TAPP portion. Then, the photoinduced electron

620   transfer (PET) process occurred under light conditions, forming TAPP-M$^-$ and TTF$^+$,

621   respectively. For TTF$^+$, the spin density was mainly concentrated on the C=C bond and

622   S atom, so the oxidation of H_2O molecules occurred at both sites, and the reduction of

623   CO_2 occurred at the metal ion center of TAPP-M$^-$.

624
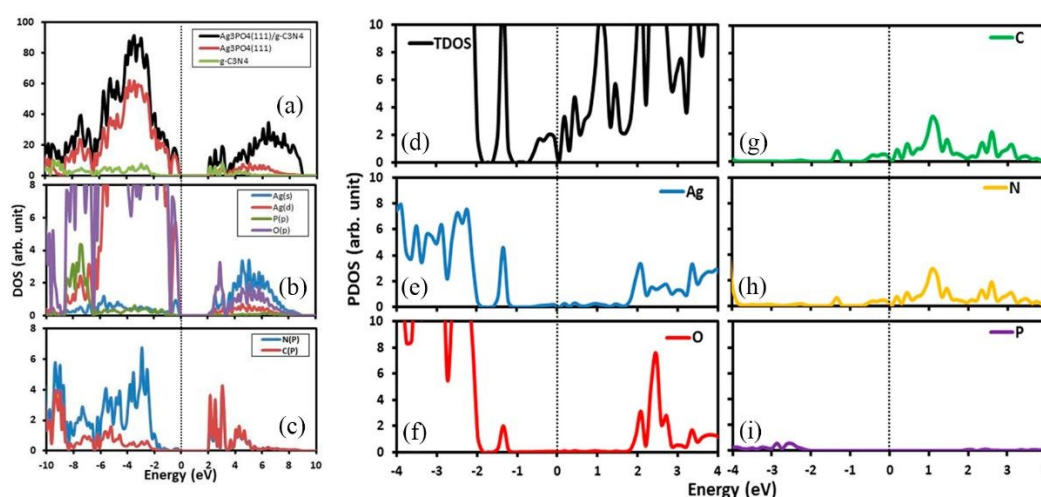
625   **Fig. 9. (a) TDOS and PDOS of the hybrid Ag$_3$PO$_4$ (111)/g-C$_3$N$_4$. (b) PDOS of**

626   **Ag$_3$PO$_4$(111) in the hybrid Ag$_3$PO$_4$ (111)/g-C$_3$N$_4$. (c) PDOS of g-C$_3$N$_4$ in the hybrid**

627   **Ag$_3$PO$_4$ (111)/g-C$_3$N$_4$. (d) TDOS of the hybrid Ag$_3$PO$_4$ (111)/Ag/g-C$_3$N$_4$. (e)-(i)**

628   **PDOS of the hybrid Ag$_3$PO$_4$ (111)/Ag/g-C$_3$N$_4$. Energy = 0 eV corresponds to the**

629   **Fermi level. Reproduced with permission from ref. [84]. Copyright 2019 American**

630   **Chemical Society.**

631   In addition to the above applications, DFT calculation is also widely used in the

632   analysis of CO_2 reduction pathways, which is difficult to be intuitively represented

633   through the experimental process alone. When analyzing the reduction pathways, it is

634   necessary to determine the coordination mode of the CO_2 molecules on the

635   photocatalyst surface, and this process can be realized by DFT calculation. Sun Hee

636   Yoon and co-workers investigated the selectivity of homogeneous and heterogeneous

637     $CuFeO_2/CuO$ complexes in converting CO_2 to formate by theoretical calculation, and

638   the materials was named HMS and HTS, respectively.[51] In order to better study the

639   adsorption mode of CO_2 molecules on the surface of the material (Fig. 10b), the

640   adsorption energy of CO_2 was first calculated (Fig. 10a). For HTS and HMS, the

641   tridentate bonding had the most negative adsorption energy, so CO_2 molecules can be

642   strongly adsorbed at Cu_1-Fe_1-Cu_2 sites of HMS and the Cu_2-Cu_3-Cu_4 sites of HTS (Fig.

643   10d and 10i). The oxygen coordinated monodentate bonding (O_{CO_2}-monodentate) of

644   the material were the weakest. For bidentate bonding, the adsorption energy of carbon

645   coordination (C_{CO_2}-bidentate) was more negative than that of oxygen coordination

646   (O_{CO_2}-bidentate). Therefore, it can be seen that the stability order of the four

647   coordination modes was: tridentate > C_{CO_2}-bidentate > O_{CO_2}-bidentate > O_{CO_2}-

648   monodentate. Subsequently, the redistribution of the charge on the surface of the

649   material was evaluated by Bader charge analysis. During this analysis, positive and

650   negative represent the donation and reception of electrons by the atoms in the adsorbed

651   CO_2 molecules, respectively. For both O_{CO_2}-monodentate and O_{CO_2}-bidentate (Fig. 10c,

652   10f, 10h, and 10k), the valence electrons of the O atom in the CO_2 molecule were

653   negative, and the net charge of O_{CO_2}-monodentate and O_{CO_2}-bidentate were negative,

654   confirming that the CO_2 molecule behaved as Lewis acid to receive electrons from the

655   site on the catalyst surface. Therefore, negatively charged O atoms and positively

656   charged H atoms will combine to form $HCOO^-$. Through the same analysis method, for

657   HMS, since the net charge of tridentate (Fig. 10d), C_{CO_2}-bidentate (Fig. 10e), and C_{CO_2}-

658   monodentate (Fig. 10g) were all positive, the transfer of electrons to the CO_2 molecule

659   was suppressed. But it is feasible for the HTS to donate electrons to CO_2 because of

660   negative net charge in C_{CO_2}-bidentate (Fig. 10j) and C_{CO_2}-monodentate (Fig. 10l) modes.

661   In the analysis of the CO_2 reduction pathways, reaction energy and activation energy

662   are two very important factors, which can be expressed through PBE + U, PBE + D3

663   and so on. In addition, several intermediates in the path are often the key to determine

664   the subsequent products. The adsorption energy of the intermediate products is used to

665   determine whether the substance will desorb, that is, whether it plays a role as an

666   intermediate or a by-product. In short, exploring the CO_2 reduction pathways is a

667   relatively complicated problem, and it must be analyzed through a series of DFT

668   calculations combined with experiments. The specific CO_2 reduction pathways has

669   been detailed in section 3.

670
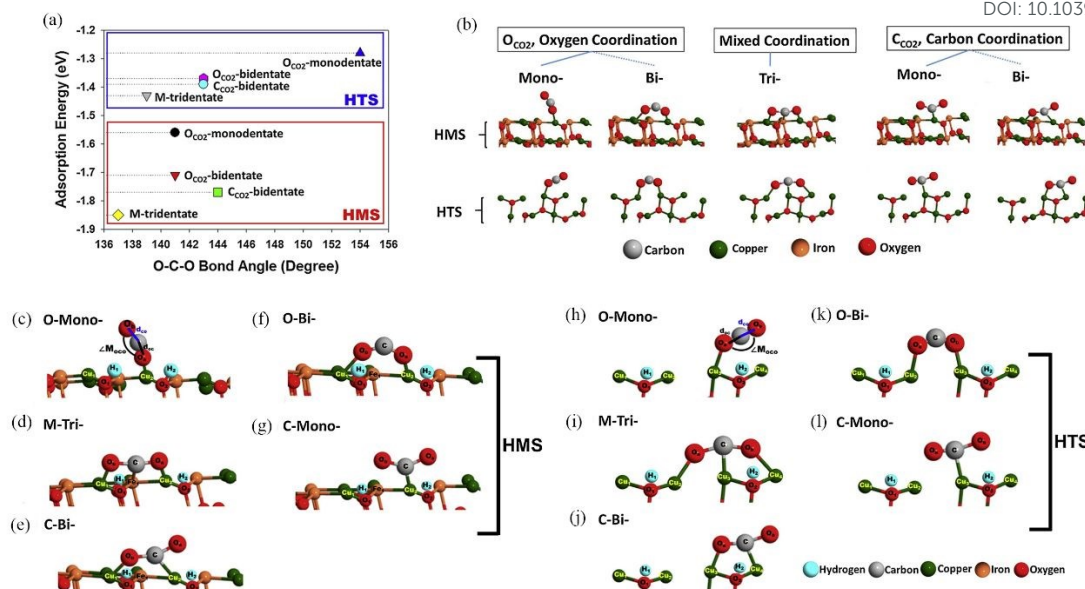
671   **Fig. 10. (a) The adsorption energy of HMS and HTS under oxygen, carbon, and**

672   **mixed coordination. (b) Schematic diagram reflects various coordination**

673   **adsorption modes of CO_2 molecules in HTS and HMS systems. (c)-(l) Schematic**

674   **diagram reflects the CO_2 adsorption configurations. Reproduced with permission**

675   **from ref. [51]. Copyright 2019 Elsevier.**

676   # 5. 2D nanomaterials for CO_2 photoreduction

677   2D materials have great application potential in the field of CO_2 photoreduction.

678   Many semiconductor 2D materials can directly act as photocatalysts or co-catalysts,

679   and some non-semiconductor 2D materials can achieve good photocatalytic

680   performance through appropriate modification, or play other critical roles (such as

681   transferring electrons, acting as a carrier, etc.) in the reduction reactions.[86]

682   **5.1 Metal-containing 2D nanomaterials**

39

683   **5.1.1 MXenes-based photocatalysts**

684   In 2011, Ti_3C_2 was obtained by exfoliating from Ti_3AlC_2, which opened the

685   curtain of MXenes material utilization in photocatalysis.[87] MXenes refer to transition

686   metal carbides, nitrides, and carbonitrides, which are a new class of 2D layered

687   materials. There is no direct precursor of MXenes material in nature, so the material is

688   usually produced in the MAX phase. The MAX phase has the general formula $M_{n+1}AX_n$,

689   where n can be 1, 2, or 3. M, A, and X in the formula represent the early transition metal

690   element, the IIIA or IVA elements, and the C or N element, respectively.[88, 89] For the

691   structure of MAX, the stability of layer A is worse than that of layer M-X. Based on

692   this feature, layered MXenes material can be obtained by selectively exfoliating layer

693   A. Intercalation agents such as dimethylsulfoxide (DMSO) and LiF can be added to

694   obtain an ultra-thin material during the exfoliating process.[29] It is worth noting that

695   during the exfoliating process, some terminated groups (such as OH, F, and O) are

696   spontaneously generated without relying on other reaction paths.[90] Therefore, the

697   general formula of MXenes is $M_{n+1}X_nT_x$, where T represents surface terminating groups.

698   So far, more than 10 kinds of MXenes have been successfully synthesized, such as

699    $Ti_3C_2T_x$, Mo_2CT_x, V_2CT_x, Nb_2CT_x, etc.

700   MXenes have some special properties: (i) The surface termination of the MXenes

701   material affects the performance of photocatalysis.[91] Zhang and co-workers reported

702   that when the O-termination group of the surface was incomplete, oxygen vacancies

703   were introduced on the surface.[92] These oxygen vacancies strongly adsorb reactants

704   (such as CO_2) for photocatalytic reactions. In addition, the surface hydrophilic

705   functional groups can enhance the connection between MXenes and other

706   photocatalysts, which facilitates the formation of heterostructures.[93] (ii) MXenes are

707   unstable under high temperature conditions and easily oxidized. Huang *et al.*[94] used

708   Ti_3C_2 as a carbon skeleton and titanium source, and oxidized it to form N-doped

709    $TiO_2@C$ under high temperature conditions. The apparent rate constant of

710   photocatalytic degradation of phenol reached 1.646×10^{-2} min^{-1}. (iii) The excellent

711   electrical conductivity of MXene material enables it to act as an "electronic sink" ,

712   which is beneficial to the transfer of electrons, so MXene material can be used as an

713   excellent co-catalyst.[95] (iv) Due to the amount of interlayer space of MXene material,

714   it is beneficial to the adsorption of gas molecules. Wang and co-workers found that the

715   CO_2 adsorption capacity of the intercalated Ti_3C_2 was 5.79 mmol g^{-1}, and the original

716   Ti_3C_2 had a CO_2 adsorption capacity of only 1.33 mmol g^{-1}.[96]

717   The ideal pristine MXenes are metallic and have no semiconductor properties, so

718   the bare MXenes cannot be used as a photocatalyst alone.[97] Although some MXenes

719   acquire semiconducting natures under the action of surface termination groups, few

720   MXenes have been used for photocatalysis alone due to the mismatched band structure.

721   Because of their lower Fermi level, metallic MXenes are usually used as the excellent

722   co-catalyst.[98] In the study of photocatalytic reduction of CO_2, MXenes mainly form

723   composites with other semiconductors to improve the photocatalytic performance of

724   materials.

725   Due to its large specific surface area and excellent electrical conductivity, the 2D

726   MXene material can serve as a carrier for many photocatalysts. For example, Cao and

727   co-workers successfully prepared 2D/2D ultrathin Ti_3C_2/Bi_2WO_6 nanosheets and

728   applied them to CO_2 reduction experiment.[99] Ti_3C_2 material was obtained by selective

729   ultrasonic exfoliating of Al element from layered Ti_3AlC_2, and then Bi_2WO_6 nanosheets

730   were grown on Ti_3C_2 surface (Fig. 11). Under simulated visible light irradiation, the

731   yields of methane and methanol were 4 and 6 times that of pristine Bi_2WO_6 nanosheets,

732   respectively. MXenes can form a heterojunction with other photocatalysts to improve

733   photocatalytic effects. Wang et al.[100] prepared the quasi-core-shell In_2S_3/anatase

734   TiO_2@metallic $Ti_3C_2T_x$ hybrids by in situ hydrothermal method. A double

735   heterojunction structure of type-Ⅱ heterojunction and Schottky junction was

736   simultaneously formed in the material, and the formed electron channel greatly

737   promoted the transfer efficiency of photogenerated electrons. Excellent photocatalytic

738   performance was determined by the visible light absorption capacity of In_2S_3, the wide

739   bandgap of TiO_2, and the conductivity of MXenes. Su et al.[101] synthesized

740    $Nb_2O_5/C/Nb_2C$ (MXenes) material by one-step oxidation of CO_2. The Schottky

741   junction was formed on the surface of Nb_2O_5/Nb_2C. The electrons were transferred

742   from Nb_2O_5 to Nb_2C, and Nb_2C served as electron sink. At the same time, due to the

743   intimate combination between Nb_2C and Nb_2O_5, the transfer of electrons was greatly

744   promoted. Furthermore, the termination of the MXenes material can be fully utilized to

745   enhance the CO_2 reduction efficiency. Ye et al.[102] used the surface-alkalinized Ti_3C_2 as

746   a co-catalyst to improve the ability of commercial titania (P25). The hydroxyl group on

747   the surface of the Ti_3C_2 can provide abundant active sites, which was beneficial to the

748   adsorption and activation of CO_2 molecules. The yields of CO and CH_4 were 11.74 and

749   25 $\mu mol\ g^{-1}\ h^{-1}$, which were 3-fold and 277-fold that of pristine P25, respectively.

750   Related studies have shown that MXenes materials can inhibit photocorrosion of CdS.

751   Xie et al.[103] showed that after 2D Ti_3C_2 and CdS constitute a heterojunction, Ti_3C_2 can

752   be employed as an electron mediator. At the same time, due to the strong interaction

753   between Cd^{2+} and Ti_3C_2, the Cd^{2+} generated during the process of photocorrosion was

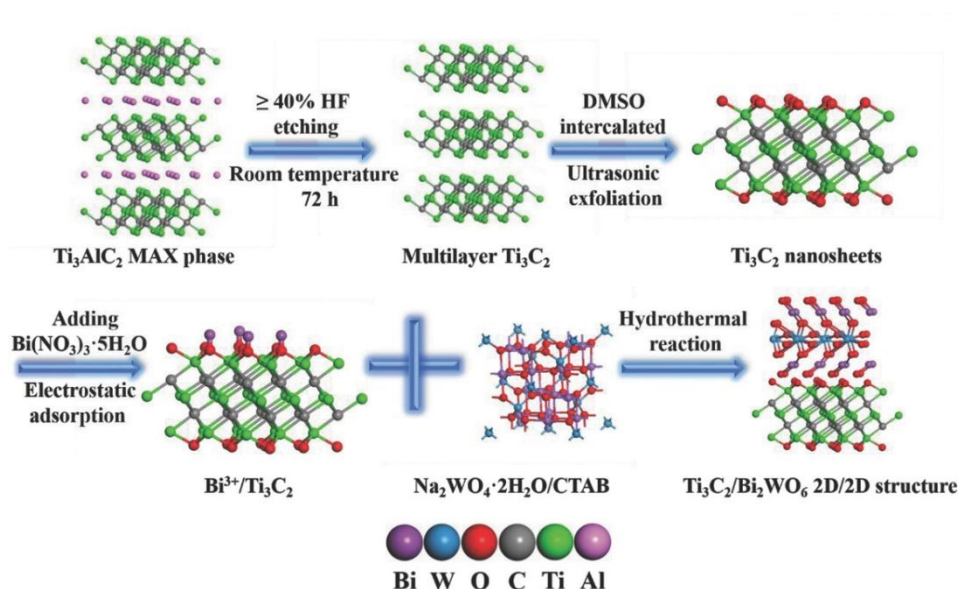754   confined on the Ti_3C_2 mezzanine, effectively preventing the leakage of Cd^{2+}.

755

756   **Fig. 11. Schematic illustration of the synthetic process of 2D/2D heterojunction of**

757   **ultrathin Ti$_3$C$_2$/Bi$_2$WO$_6$ nanosheets. Reproduced with permission from ref. [99].**

758   **Copyright 2018 Wiley-VCH.**

759   **5.1.2 LDHs-based photocatalysts**

760   In 1842, Hochstetter first discovered the natural hydrotalcite mine from the schist

761   deposit   in   Sweden,   and   Feitknecht   successfully   synthesized

762   [Mg$_6$Al$_2$(OH)$_{16}$]CO$_3$ · 4H$_2$O in 1942.[104, 105] LDHs are a type of "hydrotalcite-like

763   compounds", also known as anionic clay, which have great application value in

764   catalysis, medicine, adsorption, and ion exchange.[106-109] The general formula of LDHs

765   is [M$_{1-x}^{2+}$M$_x^{3+}$(OH)$_2$]$^{x+}$[A$_{x/n}$ H$_2$O]$^{x-}$, where A represents an anion between layers, such

766   as CO$_3^{2-}$, SO$_4^{2-}$, Cl$^-$ and ClO$_4^-$, etc. M^{2+} and M^{3+} represent the divalent and trivalent

767   cations, respectively. The common divalent cations contained in LDHs are Mg^{2+}, Co^{2+},

768   Ni^{2+}, or Zn^{2+}, and trivalent cations are Al^{3+}, Cr^{3+}, or Fe^{3+}.[110, 111] However, in some

769   special cases, LDHs also contain some monovalent and tetravalent cations, such as Li$^+$,

770   Zr^{4+}, Ti^{4+}, and Sn^{4+}.[112] LDHs have a unique host-guest structure, the host structure of

771   LDHs consists of a positively charged brucite-like layer. Each octahedron forms a unit

772   layer by a common edge, wherein OH$^-$ is located at the apex of each octahedron, and

773   the center of the octahedron is metal cation.[113] According to the occupancy of the

774   central cation, the host structure can be divided into two types, one is the trioctahedron

775   in which all octahedral centers are occupied by metal ions, and the other is the

776   dioctahedron in which two-thirds of the centers are occupied by metal ions. There are

777   also some guest substances between the brucite layer of LDHs: charge-balance cations

778   and crystal water molecules.[114] The electrostatic attraction between the positively

779   charged brucite layer and the negatively charged interlayer ensures the stability of the

780   LDHs structure.

781   In 2011, Izumi's group used Zn-Cu-M (Ⅲ) (M=Al, Ga) LDHs materials for

782   photocatalytic reduction of CO_2 for the first time.[115] They synthesized Zn and/or Cu

783   hydroxides and combined them with Al or Ga. Zn-Al LDH was the most active in

784   reduction reaction, and the yield of CO was 620 nmol h^{-1} g_{cat}^{-1}. After Cu was introduced

785   into Zn-Al LDH and Zn-Ga LDH, the selectivity of methanol improved from 5.9 to 26

786   mol% and from 39 to 68 mol%, respectively. Since then, LDHs have received more and

787   more attention in CO_2 photocatalytic reduction due to their unique characteristics.

788   Firstly, due to the Lewis acidity of CO_2, alkaline photocatalysts tend to have greater

789   advantages in the adsorption of CO_2 molecules. The host structure of LDHs contains a

790   large amount of alkaline OH groups, which can effectively adsorb CO_2 molecules.

791   Wang and co-workers prepared Co-Al LDH nanosheets for photocatalytic CO_2

792   reduction at atmospheric concentration (400 ppm) under visible light irradiation.[116] The

793   yield of methane was 4.3 μmol g^{-1} h^{-1} without the addition of sacrificial agent and noble

794   metals. After five cycles of repetition test, the yield of CH_4 remained almost unchanged,

795   the material exhibited excellent stability. The CO_2 adsorption capacity of Co-Al LDH

796   was 2.95 cm^3 g^{-1}, which was about twice higher than P25. In this experiment, the better

Journal of Materials Chemistry A Accepted Manuscript

797 photocatalytic performance was mainly due to the strong adsorption capacity of alkaline

798 OH groups on the surface of Co-Al LDH. Secondly, the composition of LDHs is

799 controllable. LDHs generally contain two or three different metal cations, so the

800 photocatalytic properties of the material can be changed by adjusting the proportion of

801 metal cations. This principle is similar to the element doping process of semiconductor

802 photocatalysts. Kong *et al.*[117] studied the performance of Ti-Li-Al LDH with different

803 Ti : Li : Al molar ratios in CO_2 photocatalytic reduction. By comparing $Ti_1Li_3Al_1$-LDHs,

804 $Ti_1Li_3Al_2$-LDHs, $Ti_1Li_3Al_3$-LDHs, and $Ti_1Li_3Al_4$-LDHs, $Ti_1Li_3Al_2$-LDHs exhibited the

805 largest specific surface area and the strongest CO_2 adsorption capacity, and the yield of

806 methane was 1.33 mmol h^{-1} g^{-1}. At the same time, by theoretical calculation, it was

807 found that $Ti_1Li_3Al_2$-LDHs was the p-type semiconductor with the narrowest bandgap

808 among all the samples. In addition to the proportion of metal ions, Xiong *et al.*[118]

809 studied the effect of the types of metal cations in LDHs on the selectivity of CO_2

810 photoreduction products. They performed photoreduction experiments on Zn-based

811 LDH containing different trivalent and tetravalent metal ions, as well as in-situ diffuse

812 reflectance infrared measurements and DFT calculations. The results showed that when

813 the d-band center of cations was relatively close to the Fermi level, the CO_2 molecules

814 were more likely to be reduced to CH_4 or CO. The cations with the d-band center far

815 away from the Fermi level had poor adsorption capacity on CO_2 molecules, and H_2 was

816 more likely to be produced in this process. Thirdly, the interlayer space of LDHs is the

817 main site of photocatalytic process, and the interlayer space contains some anions and

818 H$_2$O molecules. The proper regulation of the interlayer space of LDHs will affect its

819 photocatalytic performance. Wein *et al.*[119] pretreated Zn-Cu-Ga-CO$_3$ LDH with 423 K

820 in a vacuum environment for 1 h, liberating 31% of the crystal water in the interlayer

821 space. After photocatalytic reduction of CO$_2$, the methanol yield was 2.8 μmol g$_{cat}$$^{-1}$ h^{-}

822 ^{1}. Under the same conditions, the methanol yield of the unpretreated Zn-Cu-Ga-CO$_3$

823 LDH material was 0.011-0.30 μmol g$_{cat}$$^{-1}$ h^{-1}. Therefore, the liberation effect of the

824 interlayer space is very obvious. On the other hand, since the interaction between the

825 LDHs laminate and the interlayer anions is weak, the interlayer anions have a certain

826 exchangeability, so the photocatalytic performance can be improved by introducing

827 different interlayer anions. Finally, since the metal cation is located at the center of the

828 octahedron in the host structure, the recombination of photogenic carriers is suppressed

829 due to the high dispersion of metal cation, thereby effectively improving the efficiency

830 of photocatalytic reduction of CO$_2$.

831   Ultrathin LDHs, with their outstanding structural properties, are often more

832 popular than bulk LDHs in CO$_2$ photocatalytic reduction. The thickness of 2D LDHs is

833 an important factor affecting its photocatalytic performance.[120] It is generally believed

834 that ultrathin materials tend to expose more surface defects, while in LDHs, they mainly

835 appear as oxygen vacancies and metal vacancies. For example, Zhao *et al.*[121] reduced

836 the thickness of the Zn-Al LDH sheet to create O vacancies, which in turn resulted in

837 the formation of coordinated unsaturated Zn, thereby enhancing the photoreduction

838   efficiency of CO_2. Tan and co-workers synthesized Ni-Al LDHs materials with the

839   thickness ranging from 27 nm to 5 nm and to 1 nm.[78] The material was characterized

840   by X-ray absorption fine structure, soft X-ray absorption spectroscopy and positron

841   annihilation spectrometry, and the results proved that lower material thickness has more

842   metal defects. Although LDHs materials have many advantages, the photocatalytic

843   properties of pristine LDHs are often unsatisfactory, so researchers often synthesize

844   complexes to achieve higher photocatalytic activity. For example, Jiang and co-workers

845   synthesized $0.1Cu_2O@Zn_{1.8}Cr$ LDH for CO_2 photocatalytic reduction,[122] and the CO

846   yield was 6.3 μmol after 24 h, while the CO yield was only 0.1 μmol when LDH was

847   not loaded with Cu_2O. In this process, Cu_2O acted as electron traps, which promoted

848   the transfer of charge. Gao et al.[123] successfully assembled Fe_3O_4/Mg-Al LDH by co-

849   precipitation method and used it in CO_2 photocatalytic reaction. The production rate of

850   CO (422.2 μmol g^{-1} h^{-1}) and CH_4 (223.9 μmol g^{-1} h^{-1}) were 1.8 and 1.7 times that of

851   pristine Mg-Al LDH, respectively. In this composite, Fe_3O_4 facilitated the separation

852   of electrons and holes, while 2D Mg-Al LDH could reduce the transmission resistance

853   of electrons and provide more active sites.

854   In addition to being an excellent photocatalytic material, LDHs can also serve as

855   a precursor for other photocatalysts. LDHs have a number of advantages as a precursor,

856   such as high dispersion of metal cations at the atomic level, high specific surface area,

857   and homogeneous microstructure, etc.[124] Chen et al.[125] successfully produced a series

858 of CoFe-based photocatalysts by hydrogen reduction of Co-Fe-Al LDH nanosheets in

859 the range of 300-700°C. With the increase of reduction temperature, the selectivity of

860 CoFe-x reduction products gradually shifted from CO to CH_4, and the selectivity of

861 CH_4 in CoFe-650 reduction products reached 60%, and the selectivity of C_{2+} reached

862 35% (Fig. 12a). Zhao's group used Ni-Al LDH as a precursor to prepare NiO nanosheets

863 with a large number of Ni and O vacancies.[126] They calcined Ni-Al LDH at high

864 temperature to make it undergo topological transformation, and then obtained the

865 catalytic material NiAl-X, where X represented the reaction temperature. NiAl-275 had

866 the greatest CH_4 selectivity, and the HER reaction could be completely suppressed

867 under irradiation above 600 nm (Fig. 12b).

868
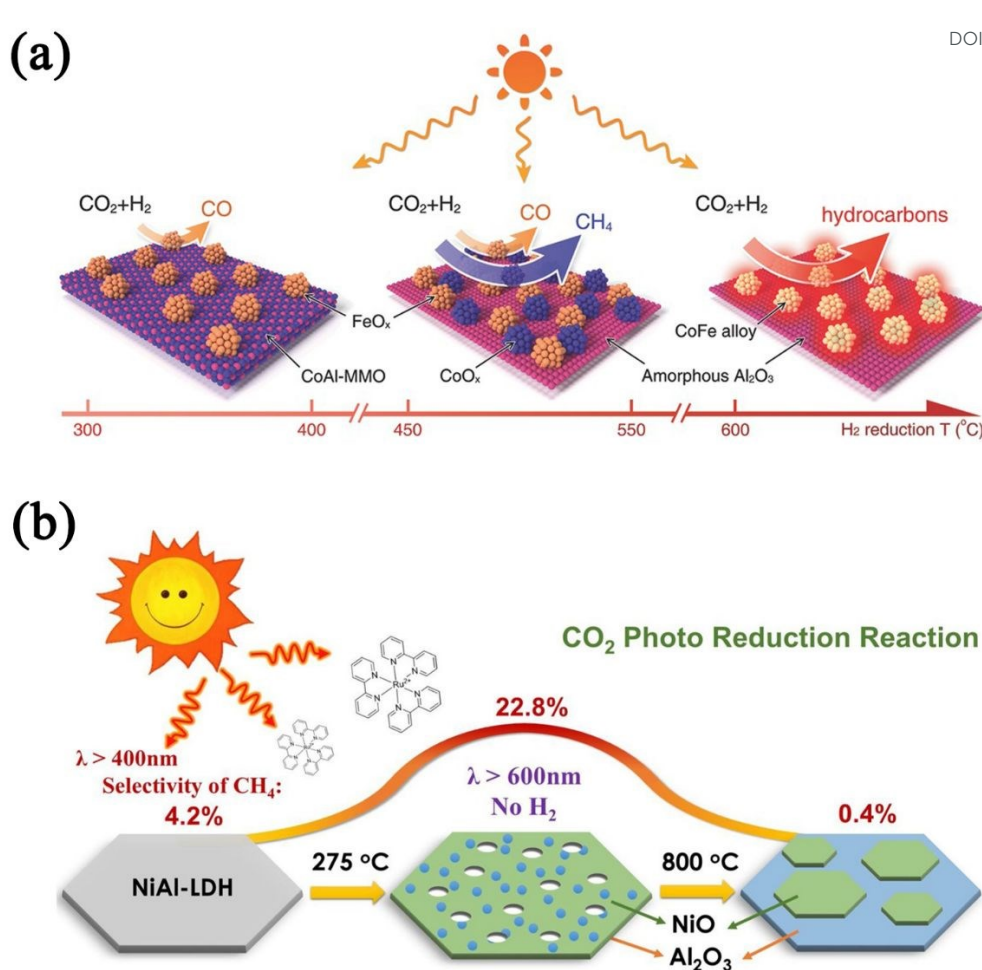
Fig. 12. (a) Schematic illustration of the different CoFe-x catalysts formed by hydrogen reduction of a CoFeAl-LDH nanosheet precursor at different temperatures. Reproduced with permission from ref. [125]. Copyright 2018 Wiley-VCH. (b) Schematic illustration of NiAl-X derived from the topological transformation of NiAl-LDH. Reproduced with permission from ref. [126]. Copyright 2020 Elsevier.

5.1.3 TMDs-based photocatalysts

Transition metal dichalcogenides (TMDs), a class of 2D semiconductor materials,

877   have recently received extensive attention in the field of CO_2 photoreduction. The

878   general formula of TMDs is MX_2, where M represents a transition metal element and

879   X represents a chalcogen element.[127] Single-layer TMDs exhibit a X-M-X sandwich

880   structure in which the transition metal is between two chalcogens. The atoms in the

881   layer are connected by covalent bonds, and the atoms between the layers are connected

882   by relatively weak Van der Waals forces.[128, 129] Common TMDs include MoS_2, $MoSe_2$,

883   WS_2, and WSe_2, etc., among which MoS_2 and WS_2 are widely used in photocatalytic

884   research for their excellent performance. It is worth noting that some TMDs have

885   different fundamental phases. For example, MoS_2 has three phases, namely 1T phase,

886   2H phase, and 3R phase. The 1T phase is a square symmetry single-layer repeating unit.

887   The 2H phase is hexagonal symmetry, wherein the Mo atom maintains an octahedral

888   coordination, and the 3R phase is a prismatic symmetric three-layer repeating unit.[130,

889   131] Related experiments showed that MoS_2 can be converted from 2H phase to 1T phase

890   by Li intercalation.[132-134]

891   TMDs are ideal materials for replacing noble metals as co-catalysts due to their

892   high stability and low cost. In addition, under the influence of quantum confinement

893   effect, the CB energy level of the material will change accordingly with the number of

894   layers, so TMDs exhibit excellent co-catalytic performance.[135] Xu et al.[136] successfully

895   wrapped MoS_2 nanosheets on TiO_2 fiber to form 1D/2D TiO_2/MoS_2 composites. By

896   changing the molar percentage of surface MoS_2 relative to TiO_2, different CO_2

897 photocatalytic reduction effects can be obtained. The experimental results showed that

898 when the molar percentage of MoS_2 and TiO_2 was 10, the production rates of CH_4 and

899 CH_3OH reached the maximum, which were 2.86 and 2.55 μmol h^{-1} g^{-1}, respectively.

900 Through the investigation of material recycling capacity, it was found that the

901 photocatalytic activity did not decrease significantly after four cycles. In addition, MoS_2

902 can be used as a co-catalyst to increase the selectivity of CH_3OH in the products.

903 Because the Mo cation site at the edge of MoS_2 is beneficial to stabilize the CH_xO_y

904 intermediate by electrostatic attraction, it is favorable for the conversion of CO_2 to

905 CH_3OH. [137] Compared with noble metals, MoS_2 tends to have a higher current density

906 and a lower overpotential, which can receive photogenerated electrons more effectively

907 in composite materials. Jung et al.[138] loaded few-layered MoS_2 on three-dimensional

908 graphene aerogel and porous TiO_2 material (TGM) through simple one-pot

909 hydrothermal method (Fig. 13a). Mesoporous TiO_2 nanoparticles and MoS_2

910 nanoparticles were distributed on the graphene surface (Fig. 13b and 13c).

911 Photogenerated electrons were transferred from the CB of TiO_2 through the graphene

912 to the edge of MoS_2 (Fig. 13e). The yield of CO in the final product was 92.33 μmol g^{-1}

913 h^{-1}, which was 14.5 times that of pristine TiO_2 (Fig. 13d). After 15 cycles of

914 experiments, there is no loss of material weight, and the original conversion rate can be

915 maintained. MoS_2 can also act as a charge-transfer mode switcher. Zhang et al.[139]

916 prepared $WO_3@MoS_2/CdS$ composites by three-step wet chemistry, in which MoS_2

917 was located at the interface between WO_3 and CdS. As a charge-transfer mode switcher,

918 MoS$_2$ successfully converted the type-Ⅱ electron transfer mode into the Z-system.

919 Photogenerated electrons from the CB of WO$_3$ and photogenerated holes from CdS can

920 be transferred to MoS$_2$ for recombination. At the same time, MoS$_2$ provided many

921 active sites for the whole reaction process, which improved the efficiency of

922 photocatalysis. Therefore, in the WO$_3$@MoS$_2$/CdS system, MoS$_2$ acted as a charge-

923 transfer mode switcher, an electron-hole mediator, and a co-catalyst.
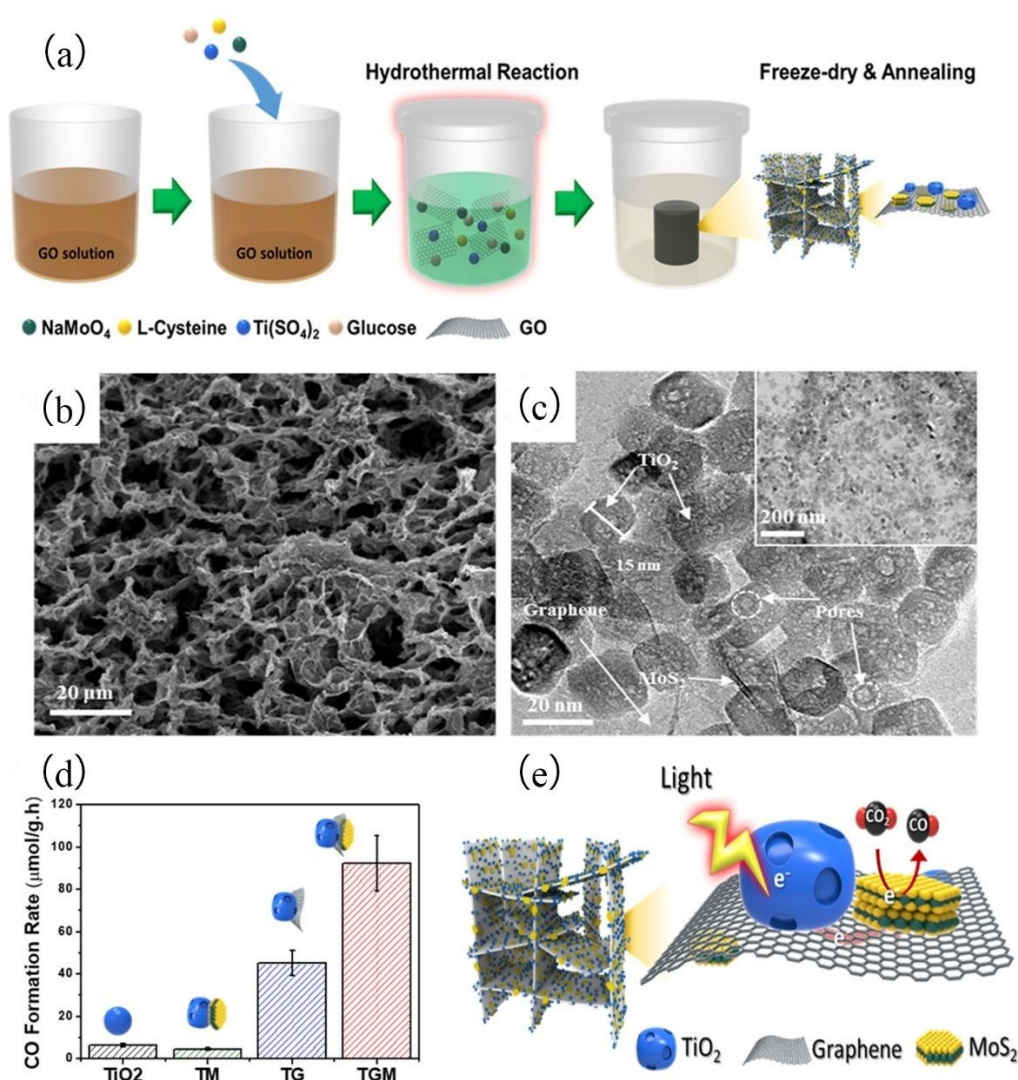

924

925 **Fig. 13. (a) Schematic diagram of synthesis process of TGM through simple one-**

926 **pot hydrothermal method. (b) and (c) SEM and TEM image of TGM. (d) The CO**

927 **formation rate of TGM, TG, TM, and TiO$_2$. (e) Schematic diagram of material**

928 **(TGM) structure and photogenic electron transfer process. Reproduced with**

929 **permission from ref. [138]. Copyright 2018 American Chemical Society.**

930   TMDs have some unique characteristics compared with other 2D photocatalytic

931 materials. For example, MoS$_2$ generally has three phases of 1T (metallic), 2H

932 (semiconducting), and 3R. The 1T metal configuration of MoS$_2$ has more active sites

933 on the basal plane and edges, and the conductivity is better, but there is thermal dynamic

934 metastable state. Huang *et al.*[140] combined the properties of 1T MoS$_2$ and 2H MoS$_2$ to

935 synthesize 1T/2H MoS$_2$, and then combined the system with 2D g-C$_3$N$_4$ to form a

936 ternary composite structure. In this system, 1T MoS$_2$ mainly acted as an electron trap

937 to promote electron transfer and provided many active sites, while a heterojunction was

938 constructed between 2H MoS$_2$ and g-C$_3$N$_4$ for the separation of carriers. In general, the

939 MoS$_2$ material is black, so the photothermal effect will occur in the photocatalytic

940 reaction. In the photocatalytic reaction process, there are two main sources of thermal

941 energy, one is direct thermal radiation, and the other is the photothermal effect of the

942 material. Guo *et al.*[141] successfully prepared WS$_2$/MoS$_2$@WO$_{3-x}$ double Z-system

943 heterojunction photocatalyst with core-shell structure. In this experiment, the

944 photothermal effect of the material was quantitatively studied by IR thermal driver.

945 Before irradiation, the temperature of the material was only about 24°C. After

946   irradiation, the temperature of the material rose to about 190°C, which indicated that

947   the photothermal effect was obvious in the photocatalytic process. Therefore, the

948   photothermal effect of MoS_2 can provide valuable reference ideas for the construction

949   of photocatalytic materials.

950   At present, the main TMDs material used in the study of CO_2 photoreduction is

951   MoS_2, and other TMDs have relatively few applications in this field. There is a report

952   on the photoreduction of CO_2 by WSe_2. Oh's group synthesized the WSe_2-Graphene-

953   TiO_2 ternary composite by ultrasonic technology,[142] in which WSe_2 and TiO_2 were

954   distributed on the surface of graphene. In heterojunction systems, WSe_2 acted as an

955   electron trap to promote the charge separation. The band gap of WSe_2-Graphene-TiO_2

956   was about 1.62 eV. Under the irradiation of UV-visible light, the optimal yield of

957   CH_3OH was 6.900 μmol g^{-1} h^{-1} with Na_2SO_3 as sacrificial agent. WS_2, as an important

958   class of TMDs, has been extensively studied in the direction of photocatalytic hydrogen

959   evolution, degradation of pollutants, sterilization and so on,[143-146] but its research in the

960   field of photoreduction of CO_2 is scarce.

961   **5.1.4 Others**

962   Metal oxides are an important class of photocatalytic materials. Metal oxides have

963   strong antioxidant properties, and the commonly used metal oxides in photocatalysis

964   mainly include TiO_2, ZnO, Co_3O_4, WO_3, etc.[83, 147-149] TiO_2 is one of the most studied

965   materials in the field of photocatalysis. TiO_2 has the merits of non-toxicity, low price,

966   high stability and good photocatalytic activity. Qamar *et al.*[150] synthesized 2D TiO_2

967   nanosheets by TiO_2-octylamine hybrid method, and the ultrathin properties equipped

968   the material with excellent performance. In the CO_2 photoreduction experiment, the

969   yield of formate was 1.9 $\mu mol\ g^{-1}\ h^{-1}$, which was 450 times that of bulk TiO_2. However,

970   due to its wide bandgap (3.2 eV), the response to visible light is poor, and

971   photogenerated electrons and holes are easily recombined, which greatly limits its

972   application.[151] In recent years, research on 2D TiO_2 has focused on the modification of

973   materials, including element doping, morphology control, construction of

974   heterojunctions, etc. Recently, Jiang and co-workers modified TiO_2 nanosheet with

975   Lewis base $[WO_4]^{2-}$ in which $[WO_4]^{2-}$ substituted OH^- on the surface of TiO_2.[152] The

976   basicity of $[WO_4]^{2-}$ can promote the adsorption of CO_2 molecules, and $[WO_4]^{2-}$ can

977   capture photogenerated electrons. The experimental results showed that the yield of CO

978   was 19 times that of pure TiO_2, which was higher than that of noble metal (Au, Ag)

979   modified TiO_2. 2D ZnO has good thermal stability with a direct bandgap of 3.37 eV.

980   When the number of layers of ZnO is reduced to about 8 layers, the structural properties

981   of graphene-like structures appear. Zhao *et al.*[153] reported the effect of the number of

982   layers of 2D ZnO on the performance of photocatalytic reduction of CO_2. When the

983   thickness was less than or equal to 5 layers, CO and HCOOH were the main products,

984   and the photocatalytic activity was the highest in the 3 and 4 layers. In the 6 layers,

985   CH_3OH and CH_4 were the main products. In addition to the ZnO, Chen *et al.*[83] prepared

986   2D porous Co_3O_4 and modified it with Ru-based photosensitizer. The ultrathin and

987   porous properties gave the material a lower carrier recombination rate, a larger number

988   of active sites, and a stronger ability to adsorb CO_2. The yield of CO was 4.52 μmol h$^-$

989   ^{1}, and the selectivity was 70.1%, which were better than the bulk Co_3O_4.

990   Metal-Organic Frameworks (MOFs) are a kind of porous crystalline material with

991   network structure composed of organic linkers and metal nodes, also known as porous

992   coordination polymer.[154, 155] MOFs have stimulated an immense impetus as

993   photocatalyst because of their ultra-high surface area, adjustable pore structure as well

994   as uniformly distributed coordination unsaturated metal sites.[156-158] Ye *et al.*[159] used Zn

995   porphyrin-based MOFs as photosensitizer and ZIF-67 as co-catalyst to compare the

996   effects of 2D MOFs and bulk MOFs on photocatalytic reduction of CO_2. The

997   experimental results showed that when the Zn-MOF bulk was used as a photosensitizer,

998   the turnover numbers of CO were 63.6 within 6 h. When the Zn-MOF nanosheet was

999   used as a photosensitizer, the turnover numbers of CO could reach 117.8, and the

1000   selectivity of CO increased from 89.5% to 91.0%. There are a lot of researches on the

1001   modification of MOFs materials. Recently, Wang *et al.*[160] modified the material by

1002   virtue of the large amount of coordination unsaturated metal ions in the MOFs. Firstly,

1003   tetrakis (4-carboxyphenyl)-porphyrin (TCPP) interacted with cobalt carboxyphenyl,

1004   and then benzoic acid exerted an axial constraint on cobalt ions to form 2D porphyrin

1005   MOF (PMOF) (Fig. 14a). The Co active center in ultrathin porphyrin MOF would

1006   coordinate with the N atom in g-C_3N_4, and then the g-C_3N_4 quantum dots would be

1007   supported on the PMOF material to obtain g-CNQDs/PMOF hybrids (Fig. 14b). On the

1008   one hand, it was conducive to the enrichment of CO_2 at the Co site. On the other hand,

1009   it could also promote the direct transfer of electrons from g-C_3N_4 QDs to Co sites (Fig.

1010   14c). The yields of CO and CH_4 were 2.34 and 6.02 times that of pure PMOF,

1011   respectively.
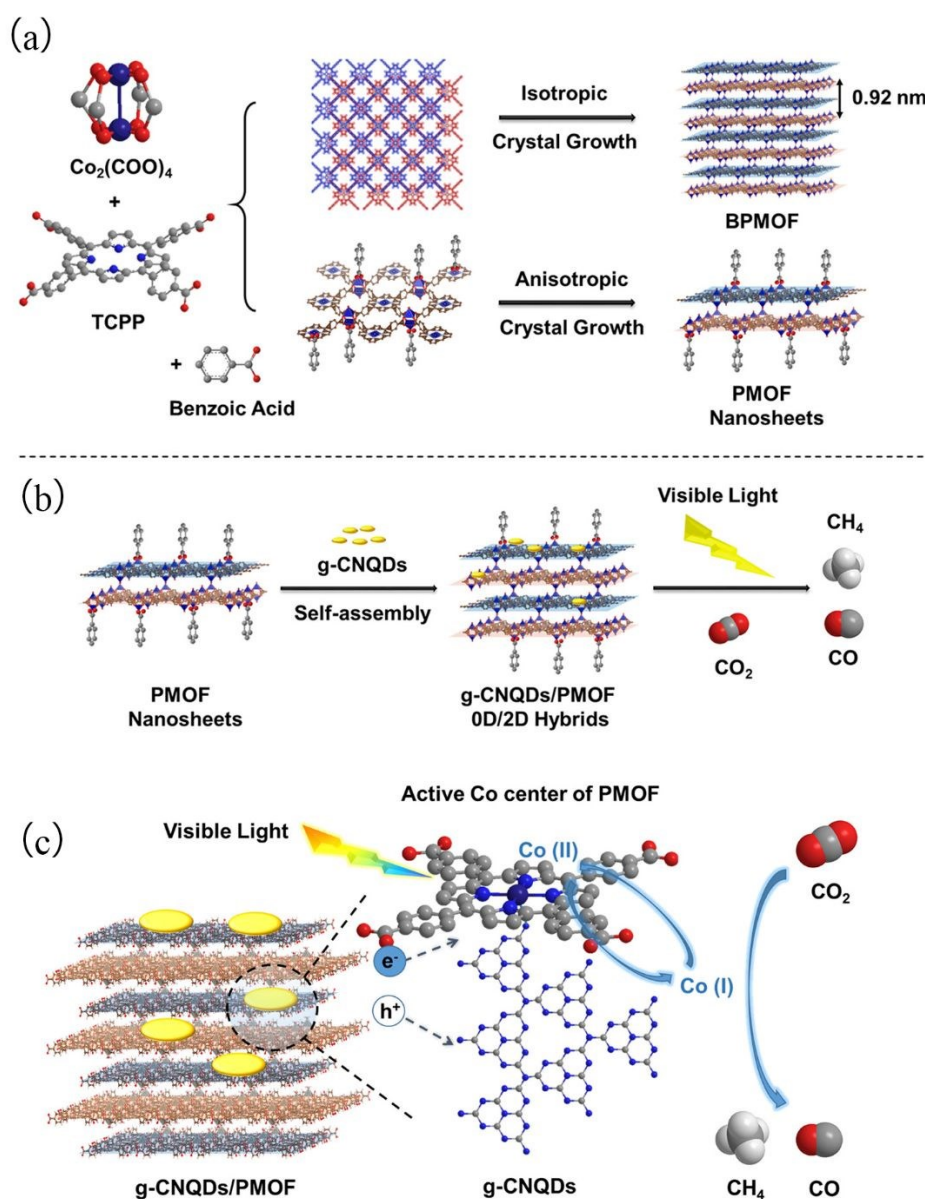
1012

1013 **Fig. 14. (a) Schematic diagram of synthesis process of PMOF. (b) Schematic**

1014 **diagram of synthesis process of g-CNQDs/PMOF hybrids. (c) Proposed**

1015 **mechanism of CO_2 reduction over g-CNQDs/PMOF hybrids under visible-light**

1016 **irradiation. Reproduced with permission from ref. [160]. Copyright 2019 American**

1017 **Chemical Society.**

1018 There are some metal oxyhalides that are used for photocatalytic reduction of CO_2,

1019 among which BiOX (X=Br, Cl, I) is the class of typical layered material with high

1020 photocatalytic activity.[161] The {X-Bi-O-Bi-X} layered structure stacked by nonbonding

1021 interactions causes a large space between the layers, and an endogenous electric field

1022 can be generated. Some studies have focused on improving photocatalytic performance

1023 by appropriate modification of metal oxyhalides. By controlling the time of

1024 hydrothermal reaction, Ye et al.[162] synthesized BiOI nanosheets exposed to {001} and

1025 {100} facets, respectively. The experimental results showed that BiOI-001 had good

1026 photoinduced carrier separation efficiency, high CB position, and strong CO_2 molecular

1027 adsorption capacity. Besides that, Zhu et al.[163] used Bi and phosphorylation to

1028 simultaneously modify the BiOBr in the form of the regular hierarchical spheres, and

1029 phosphorus existed in the form of $BiPO_4$. In this composite system, photogenerated

1030 electrons migrated from BiOBr to $BiPO_4$. When Bi was in contact with BiOBr and

1031 $BiPO_4$, a Schottky junction would be formed. The Schottky junction could promote the

1032 migration of photoexcited electrons from BiOBr to Bi, the carrier recombination was

1033   suppressed. In addition, the doping of Bi atoms could significantly increase the

1034   selectivity of CH_4. Besides that, Bai and co-workers found that 2D $Bi_4O_5Br_2$ nanosheets

1035   could also exhibit good photocatalytic reduction of CO_2 performance.[164] Its large

1036   surface area and porous structure promoted the adsorption of CO_2, and the reduction

1037   products showed certain selectivity.

1038   In addition to the above 2D metal-containing materials, there are also a few

1039   research reports on the application of 2D Bi_2WO_6 in the field of CO_2 photoreduction.

1040   For example, Wang et al.[165] loaded PtO_x nanoparticles on Bi_2WO_6 nanosheet with a

1041   thickness of 4.8 nm. The optimal yield of CH_4 was 108.8 ppm g^{-1} h^{-1}, which was 5.7

1042   times higher than pristine Bi_2WO_6.

1043   **5.2 Metal-free 2D nanomaterials**

1044   **5.2.1 g-C_3N_4-based photocatalysts**

1045   In 2009, Wang and co-workers applied g-C_3N_4 material to photocatalytic

1046   hydrogen evolution for the first time.[166] Since then, the door for the application of g-

1047 C_3N_4 in the field of photocatalysis has opened.[167, 168] Carbon nitride consists of

1048   covalently bonded carbon and nitrogen, and the C and N atoms are sp^2 hybrids to form

1049   a highly delocalized conjugated π-system.[169, 170] In theory, according to the structural

1050   difference, there are five types of carbon nitride in total, namely α-C_3N_4, β-C_3N_4, g-

1051 C_3N_4, cubic C_3N_4, and pseudo-cubic C_3N_4. Among them, g-C_3N_4 is composed of tri-s-

1052   triazine, and the atoms are connected by covalent bond, which has a high thermal and

1053   chemical stability.[171-173] The bandgap of g-C_3N_4 is about 2.7 eV, where the CB and VB

1054   position are -1.3 eV and 1.4 eV, respectively. So it can effectively reduce CO_2

1055   molecules.[174]

1056   In 2012, Dong *et al.*[175] used the g-C_3N_4 as photocatalyst to reduce CO_2 under water

1057   vapor and visible light conditions for the first time. Due to its ease of preparation, good

1058   stability, low cost, suitable bandgap, and ease of modification, g-C_3N_4 has great

1059   potential for photocatalytic reduction of CO_2.[174, 176] g-C_3N_4 has the unique tri-s-triazine

1060   units' structure, making it an excellent carrier material. For example, Tang and co-

1061   workers successfully implanted single titanium-oxide species into 2D g-C_3N_4 (2D TiO-

1062   CN).[177] Due to the tri-s-triazine units' structure, Ti^{4+}-O^{2-} was effectively anchored to g-

1063 C_3N_4 and was reduced to a highly reductive Ti^{3+}-O^- by electrons. Under the strong

1064   reduction of Ti^{3+}-O^- species, the yield of CO reached 283.9 μmol g^{-1} h^{-1}. In addition,

1065   the N atom in the skeleton of the structure could cooperate with metal ions. Huang *et*

1066   *al.*[178] used a simple deposition method to introduce Co^{2+} into the g-C_3N_4 material. The

1067   Co-N coordination formed between Co^{2+} and g-C_3N_4, thereby increasing the selectivity

1068   of CO in the reduction products. Due to incomplete polymerization of the amide

1069   groups-rich precursor, some NH_2 and NH groups are formed on the surface during the

1070   synthesis of g-C_3N_4. These groups impart a basic character to the g-C_3N_4 material,

1071   which promote the adsorption of CO_2 molecules with Lewis acidity. Mo *et al.*[179]

1072   successfully synthesized porous nitrogen-rich g-C_3N_4 nanotubes by simple

1073 supramolecular self-assembly method. The CO yield was 17 times higher than bulk g-

1074 C_3N_4. The introduction of amino group effectively improved the Lewis basicity and

1075 hydrophilicity of the material, thus promoting the adsorption of CO_2 molecules. But in

1076 the opposite direction, the NH_2 and NH groups are related to a large number of defects

1077 in layers, and some hydrogen bonds are formed in these defects, which makes the

1078 material distinct from those containing only covalent bonds. These defects affect carrier

1079 transport between layers. Li and co-workers introduced a carbon chain in the polymeric

1080 carbon nitride and carried out a CO_2 photoreduction experiment.[180] In this experiment,

1081 the carbon chain connected the defects in g-C_3N_4 through the action of C-N covalent

1082 bonds. The carbon chain acted as an electron channel, accelerating the separation and

1083 transfer of charge carriers. The yield of CO was 29.2 times higher than the original g-

1084 C_3N_4. In addition, Lin *et al.*[181] introduced 3,5-dibromobenzoyl chloride as π-conjugated

1085 organic subunits in the polymeric carbon nitride, and promoted the separation and

1086 transfer of photogenerated carriers by π-conjugated organic molecules. In g-C_3N_4,

1087 electrons were excited from N atoms to C atoms, but the two-coordinated N atoms were

1088 usually the photocatalytic active sites, so the excited electrons need to transfer from C

1089 atoms to N atoms again. However, in the above process, it is often difficult to excite

1090 electrons from N atoms to C atoms. Therefore, Fu and co-workers used the coordination

1091 between the B atoms and the two-coordinated N atom to dope the B atom into the g-

1092 C_3N_4 material.[182] According to theoretical calculation, it was easier to excite electrons

1093 from N to B than from N to C, and the CH_4 yield obtained by 1% B/g-C_3N_4 sample was

1094   32 times that of the pristine g-C_3N_4.

1095   Although g-C_3N_4 is a good photocatalytic material, the original g-C_3N_4 still has

1096   the inherent drawbacks, such as poor adsorption capacity for CO_2 molecules, low

1097   visible light absorption range, and easy recombination of carriers.[183] Therefore, g-C_3N_4

1098   generally combines with other materials to form a composite. In recent years, some

1099   studies have begun to focus on interfacial connections between g-C_3N_4 and other

1100   materials. In the process of combining different materials, it is easy to ignore the

1101   occurrence of lattice mismatch, which is not conducive to carrier separation and transfer.

1102   Wu and co-workers introduced phosphate-oxygen links in the g-C_3N_4/TiO_2-nanotubes

1103   (TNTs) complex.[184] The P-O bond strengthened the interface connection between g-

1104 C_3N_4 and TNTs, thus inhibiting the occurrence of lattice mismatch. The P-O bond

1105   accelerated the transfer of photogenerated electrons from TiO_2 to g-C_3N_4. The results

1106   showed that the yields of acetic acid, methanol and formic acid were 46.9 ± 0.76 mg

1107 $L^{-1}\,h^{-1}$, 38.2 ± 0.69 mg $L^{-1}\,h^{-1}$, and 28.8 ± 0.64 mg $L^{-1}\,h^{-1}$, respectively. In addition, the

1108   protonation of g-C_3N_4 is also used to construct the catalyst of composite structure.

1109   Protonation can significantly change the charge structure of the surface and give the

1110   material some special properties. Bafaqeer and co-workers pretreated g-C_3N_4 with

1111 HNO_3 to obtain protonated g-C_3N_4 (PCN) with positive polarity.[185] The g-C_3N_4 and

1112 ZnV_2O_6 were combined to form a 2D/2D heterojunction, and PCN was used as an

1113   electron transfer mediator and electron trap. Many high-speed charge transfer channels

1114   were constructed to transfer electrons from the CB of g-C_3N_4 to the CB of ZnV_2O_6

1115   through PCN (Fig. 15a-15c). The experimental results showed that the yield of CH_3OH

1116   was 3742 μmol g^{-1} cat^{-1}. Copolymerization is also a good method for the construction

1117   of g-C_3N_4-based composites. The specific monomers are integrated into the

1118   copolymerized carbon nitride to change the bandgap, composition, and electronic

1119   structure of the material. Hayat et al.[186] integrated trimesic acid (TMA) into polymeric

1120   carbon nitride (PCN) by copolymerization. The integration of TMA effectively

1121   promoted the transfer of electrons from the ground state to the excited state in PCN.

1122   The photocatalytic performance of the CNU-$TMA_{13.0}$ sample was 16 times that of the

1123   blank CNU in all test samples. In conclusion, g-C_3N_4 is an excellent photocatalyst and
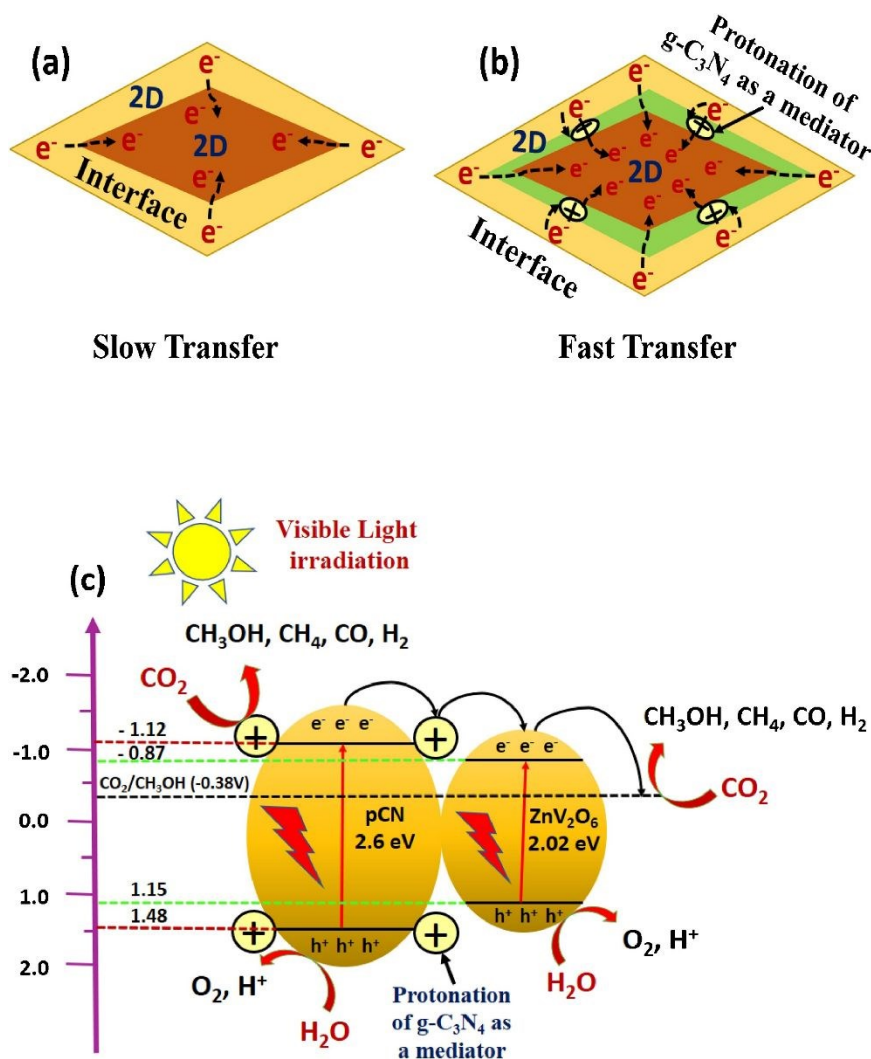
1124   deserves further study.

1125

Fig. 15. Schematic illustration of contact interfaces for (a) 2D/2D heterojunction, (b) 2D/2D heterojunction with protonation (HNO$_3$) as a mediator. (c) Schematic diagram of the separation and transfer of photogenerated charges in ZnV$_2$O$_6$/PCN composite under visible light irradiation. Reproduced with permission from ref. [185]. Copyright 2019 Elsevier.

5.2.2 Graphene-based photocatalysts

In 2004, Novoselov and Geim successfully separated graphene materials from

1133   graphite by micromechanical exfoliation.[24] As the first 2D material to be prepared,

1134   graphene materials act as guides in the wide application of 2D materials.[187] Graphene

1135   is a honeycomb-shaped carbon atom sheet formed by 2D plane sp^2 hybridization.

1136   Graphene has many excellent structural and optoelectronic properties, making it a

1137   promising photocatalytic material.[188] Firstly, the large specific surface area of graphene

1138   guarantees more active sites, which facilitates the adsorption and activation of CO_2

1139   molecules. Theoretically, the specific surface area of graphene can reach 2630 m^2 g^{-1}.[26]

1140   Then, at room temperature, graphene has a high electron transfer rate of 200,000 cm^2

1141 V^{-1} s^{-1}, the excellent conductivity facilitates the migration and transfer of photogenic

1142   electrons, thus accelerating the bonding of electrons and CO_2 molecules. Next, the

1143   thermal conductivity of graphene is about 5000 W m^{-1} K^{-1}, and its good thermal

1144   conductivity is beneficial to its photothermal effect.[189] However, it is worth noting that,

1145   unlike other semiconductor photocatalysts, graphene is difficult to generate

1146   photogenerated electrons under photoexcitation due to the lack of bandgap, which

1147   limits the application in photocatalysis. In order to overcome this drawback, some

1148   derivatives of graphene are developed, such as graphene oxide (GO) and reduced

1149   graphene oxide (rGO). These derivative materials have an adjustable bandgap and

1150   contain some special surface functional groups, which can be an ideal photocatalytic

1151   material.[190] Moreover, the combination of graphene and other semiconductors is also

1152   an effective way to overcome the bandgap drawback.

1153   The graphene material is oxidized to obtain GO, which is quite different from

1154   graphene. Some defects appear in the crystal structure of GO, forming functional

1155   groups such as epoxy groups, hydroxyl groups, and carboxyl groups, etc.[191] When

1156   graphene is oxidized, it will convert its zero-gap characteristics into semiconductor

1157   characteristics, and related experiments show that the position of the energy band can

1158   be significantly changed by changing the oxidation degree of GO, thereby affecting the

1159   bandgap of the semiconductor.[192] In addition, rGO can be obtained by partial reduction

1160   of GO, thus improving the conductivity of the material. At the same time, rGO retains

1161   some functional groups of GO.[193] Recently, there have been some studies on the

1162   modification of graphene derivatives. The oxygen-containing functional groups on the

1163   GO surface make the material alkaline. Since CO_2 itself has the characteristic of Lewis

1164   acidity, the adsorption of CO_2 molecules on the GO surface is greatly promoted. In

1165   general, oxygen functional groups are easily modified by nitrogenous substances. Liu

1166   and co-workers used ultrasound-assisted method to prepare amine functionalized

1167   GO.[194] The amine is nucleophilic and undergoes a strong nucleophilic substitution

1168   reaction with the electrophilic CO_2, which greatly increases the adsorption capacity of

1169   GO for CO_2 molecules. The optimum adsorption capacity of TEPA-GO was 1.2 mmol

1170 g^{-1} at 338 K and 0.1 atm. After 10 cycles, the adsorption capacity of the material

1171   decreased by only 1%. In addition, there are also some studies on N-doped GO.

1172   Through N doping, GO can have the following advantages: (i) An active region is

1173   formed at a position adjacent to a nitrogen atom and a carbon atom; (ii) N atoms can

1174   act as anchor centers to adsorb and activate CO_2 molecules; (iii) When GO is

1175   coordinated with metal ions, the N atom can act as a connection site.[195] Since GO is a

1176   layered structure, the interlayer spacing is an important factor affecting the properties

1177   of materials. Cai *et al.*[196] incorporated the alkyl diamine molecule into the layer of GO

1178   and expanded the intralayer spacing from 0.762 nm to over 1.030 nm (Fig. 16a and 16b).

1179   The results showed that the intralayer spacing of GO directly affected the adsorption

1180   performance of CO_2 molecules. When the interlayer spacing was 0.860 nm, the

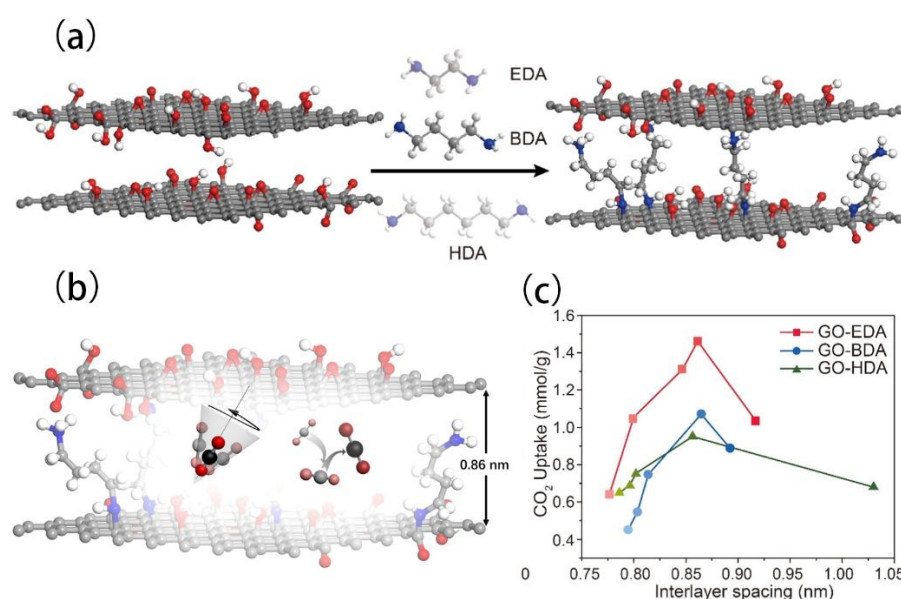1181   adsorption capacity of the CO_2 molecule was maximized (Fig. 16c).

1182

1183   **Fig. 16. (a) Reaction process and structural diagram of 1,4-butanediamine-cross-**

1184   **linked GO. (b) Schematic diagram shows the adsorption of CO_2 molecules between**

1185   **the layers of diamine-cross-linked GO. (c) The effect of interlayer spacing on CO_2**

1186   **uptake. Reproduced with permission from ref. [196]. Copyright 2019 American**

1187   **Chemical Society.**

1188   The composite structure formed by graphene-based materials and other

1189   semiconductors is an excellent way to make full use of its properties. Since the Fermi

1190   level of graphene (derivatives) is lower than the CB position of most semiconductor

1191   materials, graphene and its derivatives tend to act as an electron acceptor in the

1192   composite structure. In addition, its excellent conductivity greatly accelerates the

1193   transfer of electrons. Liu *et al.*[197] synthesized the rhombic dodecahedral Cu_2O/rGO, and

1194   used it in CO_2 photocatalytic reduction experiments. In this composite system, rGO

1195   received photogenerated electrons from the CB of the Cu_2O, then photogenerated

1196   electrons were rapidly transferred to the surface of the GO. The yield of methanol was

1197   355.3 μmol g_{cat}^{-1}. Through the study of durability and recyclability, it was found that

1198   the photocatalytic performance of the material did not decline significantly after three

1199   consecutive tests. Graphene and its derivatives can also act as an electron medium in

1200   the construction of heterostructures, facilitating the transfer of electrons between

1201   different materials. Meng *et al.*[198] synthesized ZnO/rGO/UiO-66-NH_2 composite

1202   material, in which ZnO and UiO-66-NH_2 formed Z system, and rGO acted as an

1203   electronic medium. Electrons were transferred from the CB of ZnO to the VB of UiO-

1204   66-NH_2 through rGO, which inhibited the recombination of charge carriers. Graphene

1205   and its derivatives have a large specific surface area, making it an ideal carrier material.

1206   It is worth noting that the oxygen-containing functional groups on the surface of GO

1207   can serve as sites for other semiconductors, thereby uniformly dispersing them on the

1208   surface of the GO to prevent aggregation. Wang and co-workers successfully

1209   constructed α-Fe$_2$O$_3$-ZnO/rGO heterojunction.[199] Zn spheres were oxidized to ZnO on

1210   the surface of GO and uniformly supported on the surface of GO. This anchoring effect

1211   of rGO inhibited the aggregation of Zn spheres, thereby promoting the photocatalytic

1212   reaction. Graphene and its derivatives can wrap certain photocatalyst materials, which

1213   in turn produce some special effects. For example, Zhao and co-workers synthesized

1214   (Pt/TiO$_2$)@rGO-n composite material.[200] TiO$_2$ was encapsulated by GO, wherein the

1215   surface hydroxyl group and extended π bond of GO could improve the adsorption and

1216   activation of CO$_2$ and H$_2$O molecules. The photogenerated electrons were transferred

1217   from TiO$_2$ to Pt and then to the rGO surface, which greatly promoted the separation of

1218   carriers (Fig. 17). The encapsulation of graphene can be used to inhibit the

1219   photocorrosion of materials, thereby increasing the light stability of the material. Tang

1220   *et al.*[201] prepared rGO/CdS–TiO$_2$ nanotube materials in which rGO was coated on the

1221   surface of CdS. There are two reasons why the photocorrosion of CdS was suppressed:

1222   Firstly, due to the barrier effect of rGO, the contact of active radical ·OH with CdS was

1223   prevented; Secondly, an electron-rich microenvironment was generated on the rGO

1224   surface, which in turn converted S$^-$ into S^{2-}. Because of its black and zero bandgap

1225   characteristics, graphene can absorb almost the whole spectrum of light from ultraviolet

1226   to infrared. Graphene cannot generate photogenerated electrons under the excitation of

1227   photons, but it can convert the energy of photons into heat energy, thus making the

1228   material has a good photothermal effect. Recently, Xu and co-workers specially studied

1229   the influence of photothermal effect of graphene on the photoreduction performance of

1230 TiO_2.[202] When 30 mg of graphene was introduced, the temperature of the material

1231   surface increased sharply from 58.9 to 116.4°C under light illumination of 4.38 kW

1232 m^{-2}. The experimental results showed that the photothermal effect of graphene

1233   promoted the movement speed of CO_2 molecules and carriers on the surface of the

1234   material, thereby increasing the yield of CH_4. The yield of CH_4 was 26.7 μmol g^{-1} h^{-1},

1235   which was 5.1 times that of pristine TiO_2. Therefore, modification of graphene

1236   derivatives and composite of graphene with other semiconductors are still two

1237   important aspects of the current research on the application of graphene in

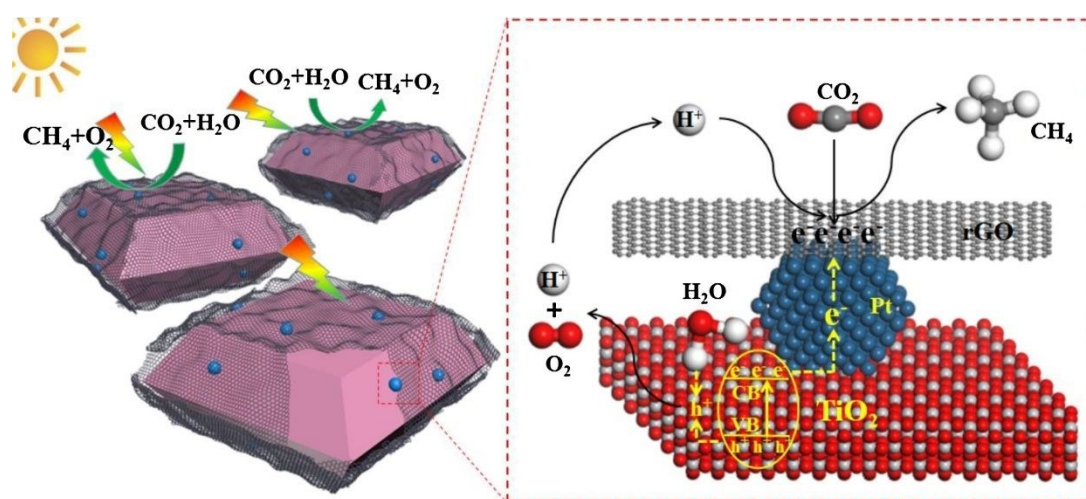1238   photocatalysis. Further research is worthwhile in order to fully exploit the potential of

1239   graphene.

1240

1241

1242   **Fig. 17.   Schematic of the mechanism for CO_2 photoreduction with H_2O to CH_4**

1243   **over (Pt/TiO_2) @ rGO-n catalysts. Reproduced with permission from ref. [200].**

1244   **Copyright 2018 Elsevier.**

1245 **5.2.3 Others**

1246   Hexagonal boron nitride (h-BN) is a type of layered 2D photocatalytic material,

1247 also known as "white graphene", which has good stability and strong electrical

1248 conductivity.[203] But the bandgap of h-BN is 5.5 eV, which needs to be modified

1249 properly to be better applied in the field of photocatalysis.[204] Zhao *et al.*[205] synthesized

1250 S-doped 2D h-BN nanosheets, which significantly adjusted the bandgap of the material,

1251 thereby improving the photocatalytic activity. Chen and co-workers studied the

1252 adsorption properties of porous h-BN to CO_2 molecules.[206] They successfully doped C

1253 atoms into h-BN materials to produce borocarbonitride (BCN) materials. In the

1254 structure of this material, both graphene and h-BN were contained in the structural

1255 domain, so it possessed the properties of both materials. The adsorption capacity of

1256 BCN for CO_2 was 3.74-3.91 $mmol_{CO_2}$ g^{-1} under the conditions of 298 K and ambient

1257 pressure, while the adsorption capacity of the original h-BN was only 1.16-1.66

1258 $mmol_{CO_2}$ g^{-1}. Therefore, their research has certain guiding value for the application of

1259 h-BN in the field of photocatalytic reduction of CO_2.

1260   Black phosphorus (BP) nanosheet is also a metal-free emerging 2D photocatalytic

1261 material. BP has excellent electrical conductivity, adjustable band gap structure, and a

1262 large surface area.[207] The band gap of BP can be effectively adjusted by changing the

1263 thickness of the material, and the bandgap range from 0.3 to 2.0 eV.[208, 209] Lee and co-

1264 workers used BP as a photocatalyst for the first time and applied it to the degradation

1265   of pollutants.[210] In the past period of time, research on 2D BP in the field of

1266   photocatalysis has mainly focused on photocatalytic hydrogen evolution and pollutants

1267   degradation.[211, 212] Very recently, some research results on the application of 2D BP in

1268   photocatalytic CO_2 reduction have been reported gradually. In these studies, 2D BP was

1269   mainly used to form composites with other materials (such as g-C_3N_4, covalent triazine

1270   framework, and $CsPbBr_3$), rather than acting as photocatalysis alone for CO_2 reduction

1271   reaction.[213-215] The reason for this phenomenon is that 2D BP has some inherent

1272   shortcomings. Firstly, the photogenerated electrons and holes of 2D BP are prone to

1273   recombination, which greatly reduces the efficiency of photoreduction. Secondly, the

1274   lone pair electrons of the P atom in BP can easily react with oxygen, and then the

1275   intermediate product will react with water. Therefore, 2D BP is extremely unstable in

1276   air and water. Aiming at the stability of 2D BP, Zhu et al.[216] used the hydroxyl group

1277   to occupy the lone pair electrons of the P atom, thereby effectively inhibiting the

1278   reaction between the lone pair electrons and oxygen. In the CO_2 photoreduction

1279   experiment, the stable BP nanosheets were used as the main photocatalyst, which

1280   showed excellent photoreduction performance and strong air and water stability. In

1281   conclusion, 2D BP still has great research and application potential in the field of

1282   photocatalytic CO_2 reduction.

1283   To sum up, it can be seen that there exist many kinds of 2D materials, which show

1284   different photocatalytic capabilities and effects in the experiments of photocatalytic

1285   reduction of CO_2. Table 3 summarizes the performance of various 2D-related

1286   photocatalysts in specific experiments. In addition, different kinds of 2D materials have

1287   different structures and photoelectrical properties. The advantages and disadvantages

1288   of the main 2D materials are shown in table 4.

1289 **Table 3. Summary of various 2D-related nanomaterials toward CO_2 reduction.**

	Photocatalyst	Mass(mg)	Light source	Reaction medium	Quantum yield	Performance	Ref.
MXenes-based	Ti_3C_2/Bi_2WO_6	100	300 W Xe lamp	CO_2 and H_2O	-	CH_4: 1.78 µmol g^{-1} h^{-1} CH_3OH: 0.44 µmol g^{-1} h^{-1}	[99]
	TiO_2/Ti_3C_2	50	300 W Xe lamp	CO_2 and H_2O	-	CH_4: 0.22 µmol h^{-1}	[217]
	$Ti_3C_2/P25$	-	300 W Xe lamp	CO_2 and H_2O	CO: 0.32% CH_4: 1.61%	CO: 11.74 µmol g^{-1} h^{-1} CH_4: 16.61 µmol g^{-1} h^{-1}	[102]
LDHs-based	TiLiAl-LDH	1000	UV lamp	CO_2 and H_2O	-	CH_4: 1.33 mmol g^{-1} h^{-1}	[117]
	$MgAl-LDH/Ag/Ga_2O_3$	-	400 W Hg lamp	CO_2 and H_2O	-	CO: 211.7 µmol h^{-1}	[218]
	NiAl-LDH	10	λ > 600 nm	CO_2 and H_2O (sacrificial reagent: TEOA)	CO + CH_4: 0.95% (AQY)	CH_4: 70.3%	[78]
	$CoZnAl-LDH/RGO/g-C_3N_4$	50	300 W Xe lamp	CO_2 and H_2O	CO: 0.45% (AQY)	CO: 10.11 µmol g^{-1} h^{-1}	[219]
	$0.1Cu_2O@Zn_{1.8}Cr-LDH$	200	200 W Hg-Xe lamp	CO_2 and H_2O	-	CO: 6.3 µmol after 24 h	[122]

	P25@CoAl-LDH	50	300 W Xe lamp	CO_2 and H_2O	CO: 0.1% (AQY)	CO: 94%	[220]
	Fe$_3$O$_4$/MgAl-LDH	50	8 W UV lamp	CO_2 and H_2O	-	CO: 442.2 μmol g^{-1} h^{-1} CH$_4$: 223.9 μmol g^{-1} h^{-1}	[123]
	g-C$_3$N$_4$/NiAl-LDH	50	300 W Xe lamp	CO_2 and H_2O	-	CO: 8.2 μmol g^{-1} h^{-1}	[221]
TMDs-based	MoS$_2$/TiO$_2$	100	300 W Xe lamp	CO_2 and H_2O	-	CH$_3$OH：10.6 μmol g^{-1} h^{-1}	[137]
	SiC@MoS$_2$	-	visible light ($\lambda \geq 420$ nm)	CO_2 and H_2O	CH$_4$: 1.75%	CH$_4$: 323 μL g^{-1} h^{-1}	[222]
	TiO$_2$/MoS$_2$	-	350 W Xe lamp	CO_2 and H_2O	0.16% (AQY)	CH$_4$：2.86 μmol g^{-1} h^{-1} CH$_3$OH：2.55 μmol g^{-1} h^{-1}	[136]
	TiO$_2$/graphene/MoS$_2$	-	300 W Xe lamp	CO_2 and H_2O	-	CO: 93.22 μmol g^{-1} h^{-1}	[138]
	WSe$_2$/Graphene/TiO$_2$	100	500 W Xe lamp	CO_2 and H_2O (sacrificial reagent: Na$_2$SO$_3$)	-	CH$_3$OH: 6.3262 μmol g^{-1} h^{-1}	[142]
	MoS$_2$/Bi$_2$WO$_6$	50	300 W Xe lamp	CO_2 and H_2O	-	CH$_3$OH: 36.7 μmol g$_{cat}$$^{-1}$	[223]

						CH_3CH_2OH: 36.6 µmol g_{cat}^{-1}	
g-C_3N_4-based	TiO/g-C_3N_4	3	300 W Xe lamp	CO_2 and H_2O (sacrificial reagent: TEOA)	-	CO: 283.9 µmol g^{-1} h^{-1}	[177]
	TiO_{2-x}/g-C_3N_4	5	300 W Xe lamp	CO_2 and H_2O (sacrificial reagent: TEOA)	-	CO: 77.8 µmol g^{-1} h^{-1}	[224]
	V_N-g-C_3N_x	5	300 W Xe lamp	CO_2 and H_2O (sacrificial reagent: TEOA)	-	CO: 56.9 µmol g^{-1} h^{-1}	[225]
	CN-xGly	20	300 W Xe lamp	CO_2 and H_2O (sacrificial reagent: TEOA)	-	CO: 29.2-fold than pure CN	[180]
	C, O co-doped polymeric g-C_3N_4	100	300 W Xe lamp	CO_2 and H_2O (sacrificial reagent: TEOA)	-	CH_3OH: 4.18 mmol g^{-1} in 6 h	[183]

	NCD/LDH/CN	50	300 W Xe lamp	CO_2 and H_2O	CH_4: 0.62% (AQY)	CH_4: 25.69 μmol g^{-1} h^{-1}	[226]
	α-Fe$_2$O$_3$/g-C$_3$N$_4$	10	300 W Xe lamp	CO_2 and H_2O	-	CH_3OH: 5.63 μmol g^{-1} h^{-1}	[227]
	Cu-SCN	25	500 W Xe lamp	CO_2 and H_2O	-	total consumed electron number: 9.47 μmol g^{-1} h^{-1}	[228]
	ZnV$_2$O$_6$/g-C$_3$N$_4$	100	35W HID Xe lamp	CO_2 and H_2O	CH_3OH: 0.21% CO: 2.8%	slurry system: CH_3OH 3742 μmol g$_{cat}^{-1}$ gas phase system: CO 3237 μmol g$_{cat}^{-1}$	[185]
	C-TiO$_{2-X}$ @g-C$_3$N$_4$	1	300 W Xe lamp	CO_2 and H_2O	-	CO: 12.30 mmol g^{-1} within 60h	[229]
graphene-based	TiO$_2$/rGO/CeO$_2$	150	15W UV-C mercury lamp	CO_2 and H_2O	-	CH_3OH: 641 μmol g$_{cat}^{-1}$ h^{-1} CH_3CH_2OH: 271 μmol g$_{cat}^{-1}$ h^{-1}	[230]
	α-Fe$_2$O$_3$-ZnO/rGO	100	300 W Xe lamp	CO_2 and H_2O	-	CH_3OH: 1.8 μmol g^{-1} h^{-1}	[199]
	Cu$_2$O/rGO	25	300 W Xe lamp	CO_2 and H_2O	-	CH_3OH: 355.3 μmol g$_{cat}^{-1}$ after 20 h	[197]

TiO$_2$-graphene	50	300 W Xe lamp	CO$_2$ and H$_2$O	-	CH$_4$: 26.4 μmol g^{-1} h^{-1}	[202]
Ag$_2$CrO$_4$/Ag/BiFeO$_3$@RGO	5	300 W Xe lamp	CO$_2$ and H$_2$O	-	CH$_4$: 180 μmol g^{-1} after 8h	[231]
RGO/TiO$_2$	5	8 W UV-A lamp	CO$_2$ and H$_2$O (sacrificial reagent: TEOA)	-	CH$_3$OH: 2.33 mmol g^{-1} h^{-1}	[232]
O-ZnO/rGO/UiO-66-NH$_2$	100	300 W Xe lamp	CO$_2$ and H$_2$O	-	CH$_3$OH: 34.83 μmol g^{-1} h^{-1} HCOOH: 6.41 μmol g^{-1} h^{-1}	[198]
NH$_2$-rGO/Al-PMOF	50	visible-light	CO$_2$ and H$_2$O (sacrificial reagent: TEOA)	-	HCOO$^-$: 685.6 μmol g$_{cat}$$^{-1}$ h^{-1}	[233]
SnO$_2$/eo-GO	20	450 W Xe lamp	CO$_2$ and H$_2$O	-	CH$_4$: 85 nmol g$_{cat}$$^{-1}$ h^{-1}	[234]
(Pt/TiO$_2$)@rGO	100	300W Xe lamp	CO$_2$ and H$_2$O	CH$_4$: 1.93% (AQY)	CH$_4$: 41.3 μmol g^{-1} h^{-1}	[200]
NiO/Ni-G	50	300W Xe lamp	CO$_2$ and H$_2$O	CH$_4$: 1.98% (AQY)	CH$_4$: 642 μmol g$_{Ni}$$^{-1}$ h^{-1}	[235]
Cu$_2$O/G	-	300W Xe lamp	CO$_2$ and H$_2$O	CH$_4$: 7.84% (AQY)	CH$_4$: 14.93 mmol g$_{Cu_2O}$$^{-1}$ h^{-1}	[236]

1290

1291 **Table 4. Structure and performance comparison of common 2D nanomaterials.**

2D nanomaterials	Band gap (eV)	General formula	Structure	Advantage	Disadvantage
MXenes	0.24~1.8 (functionalized)	$M_{n+1}X_nT_x$	Hexagonal close-packed structure	(i) Excellent stability and mechanical strength; (ii) Tunable band structure; (iii) The unique surface termination group.	(i) Preparation method is not mature enough, fluorine-containing etchant is harmful to the environment; (ii) In theory, pristine MXenes are metallic and have no semiconductor properties.
LDHs	2.0~3.4	$[M_{1-x}^{2+}M_x^{3+}(OH)_2]^{x+}[A_{x/n} H_2O]^{x-}$	Brucite-like layers	(i) The alkaline OH^- groups facilitate the adsorption of CO_2 molecules; (ii) Controllability of metal ion components; (iii) Tunable interlayer space.	The properties of LDHs depend on its structure and synthesis methods, and better materials synthesis methods need to be proposed.
TMDs	1.0~1.6	MX_2	Sandwiched structure	(i) Excellent chemical stability and conductivity; (ii) TMDs have different phases, materials with different phases have different	The surface and inner plane of the sheet have low catalytic efficiency, and the high active sites are mainly concentrated at the edge positions.

					optoelectronic properties;
					(iii) There are many groups containing unsaturated and dangling bonds on the edge of the material.
g-C$_3$N$_4$	2.7	-	Tri-s-triazine structure	(i) Low cost and easy preparation; (ii) High chemical and thermal stability; (iii) Low toxicity.	(i) Low visible light absorption range; (ii) Low surface area; (iii) Low photoinduced carrier separation efficiency.
Graphene	Zero-gap	-	Honeycomb-shaped carbon atom sheet	(i) Extremely huge theoretical special surface area and a large number of active sites; (ii) Excellent electrical and thermal conductivity; (iii) Easily modified, can be oxidized to graphene oxide with good photocatalytic performance.	The characteristic of zero band gap makes it impossible to produce photogenic electrons.

6. Combination of single-atom and 2D nanomaterials for CO_2 photoreduction

1293

1294

1295   In general, decreasing the number of layers of a 2D material will change the

1296 electronic structure of the material, such as a decrease in the DOS. Similarly, when the

1297 size of a bulk photocatalyst is reduced to the single atom level, the electronic state of

1298 the photocatalyst will also change significantly. In 2005, John Meurig Thomas first

1299 proposed the concept of single-site heterogeneous catalysts (SSHC), and pointed out

1300 the broad prospects of SSHC in the field of catalysis.[237] In 2011, Zhang and co-workers

1301 successfully anchored Pt atoms to the surface of iron oxide nanocrystals and used them

1302 for CO oxidation.[238] The Pt atom showed extremely high dispersibility on the support,

1303 and the catalyst showed excellent stability and selectivity. Since then, the concept of

1304 single-atom catalysts (SACs) has gradually emerged in the field of photocatalysis and

1305 attracted widespread attention.[239] After relevant experimental research and theoretical

1306 calculations, single-atom catalysts can effectively combine the advantages of

1307 homogeneous and heterogeneous catalysts, thereby playing the role of homogeneous

1308 catalyst analogs.[240] The active atoms in the traditional supported nanoparticle catalysts

1309 cannot be completely exposed on the surface of the support material, and the atoms

1310 below the surface cannot function, while the single atom catalysts can ensure maximum

1311 contact between the active site and the reactants. And theoretically, there are no atoms

1312 that touch each other in SACs, thus effectively preventing the accumulation of atoms.

1313   These properties make single-atom catalysts effectively distinct from common

1314   nanoparticles and elemental doping.

1315   For SACs, to achieve high dispersion and excellent catalytic performance, the

1316   development of single-atom carriers will be a key issue. For a suitable carrier, a large

1317   specific surface area is indispensable to carry as many active sites as possible. In

1318   addition, there must be specific anchor points on the carrier surface, so that single atoms

1319   can be firmly loaded. Furthermore, a high electrical conductivity is needed for carrier

1320   material, which is conducive to the transfer of electrons.[50] Taking the above factors into

1321   consideration, the 2D material is an ideal single-atom support due to its unique

1322   geometry and photoelectric structure. The effective combination of 2D materials and

1323   single atoms will endow the materials with some unique properties.[241] Firstly, single

1324   atoms can be fixed in the lattice of 2D materials or connected by covalent bonds,

1325   thereby ensuring the stability of the overall structure. Secondly, the single atoms

1326   anchored on 2D materials tend to be more coordination unsaturated, while a high

1327   proportion of low coordination atoms greatly increases the number of active sites,

1328   thereby improving catalytic performance. Thirdly, due to the ultra-thin properties of 2D

1329   materials, the open structure on either side is more conducive to the contact of reactants

1330   with single atoms, thereby maximizing the utilization of single atoms and greatly

1331   reducing the use of materials. Fourthly, single atoms generally show a long-range

1332   ordered arrangement on the surface of 2D materials, so that theoretical calculations can

1333   play a better role in the study of catalytic performance. Therefore, it will be an excellent

1334   platform that combines theoretical calculations and experimental research.[242]

1335   The effective adsorption of single atoms on 2D materials is a prerequisite for the

1336   high efficiency of CO_2 photoreduction. Therefore, analyzing the adsorption behavior

1337   between single atoms and 2D materials is helpful to the design of high-performance

1338   photocatalytic materials. Different single atoms often have different adsorption sites on

1339   2D materials. Tong and co-workers investigated the different adsorption sites of single

1340   atom Pt, Pd and Au on the bilayer g-C_3N_4.[243] According to the calculation results of the

1341   formation energy, single-atom Pd and Pt were embedded in the interlayer of g-C_3N_4,

1342   while single-atom Au was adsorbed on the surface of g-C_3N_4. The Pt atom has vacant

1343   5d orbitals, which could have a strong coordination effect with g-C_3N_4. The partial

1344   overlap of the 4d orbital and the 5d orbital of the Pd atom also makes it have a strong

1345   bonding ability. The closely packed 5d and 6s orbitals of Au atoms make them adsorbed

1346   only on the surface of g-C_3N_4. Therefore, the adsorption sites of single atom on a two-

1347   dimensional material are usually determined by its outer orbital characteristics. In

1348   addition to different adsorption sites, there are many different coordination modes

1349   between single atom and 2D materials. Firstly, single metal atoms can bond with atoms

1350   in a 2D plane through ligands. For example, Gao et al.[244] successfully anchored single

1351   atom Co to the surface of partially oxidized graphene. In this process, in addition to

1352   electrostatic force and complexation, the oxygen-containing functional groups of

1353   partially oxidized graphene also acted as ligands that anchor Co atoms. Secondly,

1354   vacancy engineering is an effective method to load single atom. Zhou et al.[245]

1355   synthesized g-C_3N_4 with N vacancies and 2H MoS_2 with S vacancies, and analyzed the

1356   adsorption properties of the materials to single atoms. Compared with the pristine g-

1357 C_3N_4 and 2H MoS_2 surface, they found that the metal atom Ir had a more negative

1358   adsorption energy in the N vacancy, and the single atom Rh had a more negative

1359   adsorption energy in the S vacancy. The reason for this phenomenon is that the vacancy

1360   on the material surface changes the regional electronic structure, which enhances the

1361   stability of the single atom load. Thirdly, single atoms can replace atoms in the plane

1362   to achieve efficient load. Di and co-workers replaced the Bi atoms in the Bi_3O_4Br

1363   nanosheet crystal lattice with a single atom of Co,[246] thus achieving uniform and

1364   isolated distribution of Co atoms on 2D materials. In short, the adsorption behavior of

1365   a single atom on 2D material surface is closely related to the electronic structure of

1366   both.

1367   The adsorption of single atoms on the 2D material will change some of the original

1368   properties of the material. It is very common to change the electronic structure of 2D

1369   materials, such as the band position, intermediate energy state and so on. Shi et al.[247]

1370   loaded atomic Co on 2D Te nanosheets and analyzed the influence of Co atoms on the

1371   electronic structure of Te nanosheets. The introduction of Co atoms caused the valence

1372   band minimum of Te nanosheets to shift upwards towards the Fermi level, thus

1373   narrowing the band gap of the material. Due to the low orbital level of the atom Co, the

1374   orbital hybridization between the Te atom and the Co atom occurred, resulting in an

1375   intermediate energy state lower than the CB. The change in the electronic structure of

1376   2D Te enhanced its ability to excite carriers, separate and transfer electrons, thereby

1377   improving the efficiency of photocatalysis. Moreover, the interfacial interaction

1378   between single atom and the 2D carrier material can result in the structural change of

1379   the material. Zhang and co-workers dispersed atom Mo in g-C_3N_4 and studied its effect

1380   on the performance of photocatalytic reduction of CO_2.[248] When Mo atoms were

1381   introduced into g-C_3N_4, the coordination of atoms in the melon unit and the

1382   coordination between adjacent melon units remained unchanged, but the melon unit

1383   itself was twisted outward. Therefore, the crystal lattice of the g-C_3N_4 was distorted,

1384   and the atomic arrangement appeared disordered, resulting in the transition of g-C_3N_4

1385   from crystalline to amorphous phase. The phase transition increased the surface area of

1386 g-C_3N_4 from 13.2 to 61.2-71.3 m^2 g^{-1}. The experimental results showed that the yield

1387   of CO was 18 μmol g^{-1} h^{-1}, which was 10.6 times higher than the crystal phase g-C_3N_4.

1388   Therefore, under certain conditions, the change of 2D material properties caused by

1389   single atom load is a favorable factor to improve the performance of CO_2

1390   photoreduction.

1391   The adsorption, activation and conversion process of CO_2 molecules on the surface

1392   of the photocatalyst are vital factors that affect the yield and selectivity of the final

1393   product. In composite systems composed of single-atom and 2D materials, metal atoms

1394   tend to act as active sites for CO_2 reduction. Therefore, in order to achieve rich and

1395   controllable reduction products, we must study the adsorption and conversion

1396   properties of single atom to CO_2 molecules. In general, the orbital characteristics of a

1397   single atom have a great influence on the adsorption of CO_2 molecules. Homlamai *et*

1398   *al.*[249] used first-principles to analyze the influence of different single atoms (Fe, Co, Ni,

1399   and Cu) loaded on g-C_3N_4 on the adsorption of CO_2 molecules. Among all the materials,

1400   Fe-g-C_3N_4 showed the most negative CO_2 adsorption energy (-0.40 eV). According to

1401   the calculation of partial DOS, it was found that the d orbital of metal atom overlapped

1402   with the p orbital of O in CO_2. The d-p orbital overlap between Fe-g-C_3N_4 and CO_2

1403   molecules was the most obvious, which means that a strong bond exists between Fe and

1404   O. The electrons transferred from O to the d orbital of Fe atoms caused a strong

1405   interaction between CO_2 molecules and the photocatalyst surface, and CO_2 molecules

1406   were absorbed stably on the surface of Fe-g-C_3N_4. The other single atoms (Co, Ni, and

1407   Cu) and O shown only small d-p overlapping peaks. In addition, through Perdew-

1408   Burke-Ernzerfhof (PBE) functional analysis, it was found that the van der Waals force

1409   between the single-atom photocatalyst and the CO_2 molecules had a great effect on the

1410   adsorption energy. In the process of CO_2 molecular reduction, the type of single atom

1411   will directly affect the conversion of CO_2 molecules, and then change the selectivity of

1412   the final product. In each step of CO_2 reduction, the barrier is an effective index to

1413   reflect the difficulty of the reduction reaction. Generally speaking, the weaker the

1414   adsorption strength between the intermediate and the photocatalyst, the higher the

1415   barrier required for the reaction.[250] For single-atom photocatalysts, different electronic

1416   structures of atoms lead to different interactions with hydrocarbons, thereby affecting

1417   the reaction barriers required for the formation of various intermediates, and showing

1418   certain selectivity in the final reduction products. Gao and colleagues loaded single-

1419   atom Pd and Pt on g-C_3N_4 for CO_2 photoreduction reaction.[251] The Pt atoms have two

1420   uncoupled electrons, so compared to Pd atoms, there is a stronger interaction between

1421   the Pt atom and the hydrocarbon. The largest barrier during the formation of CH_3OH

1422   on Pd/g-C_3N_4 was 1.46 eV, which was higher than the barrier on Pt/g-C_3N_4 (1.16 eV).

1423   For Pd/g-C_3N_4, the largest barrier required to form HCOOH was only 0.66 eV, which

1424   was much lower than the largest barrier for the formation of CH_3OH, so Pd/g-C_3N_4 was

1425   more inclined to reduce CO_2 to HCOOH. After further theoretical calculations, the

1426   formation of CH_4 on Pt/g-C_3N_4 was more thermodynamically stable. Therefore, when

1427   Pt/g-C_3N_4 was used as a photocatalyst, CH_4 was considered to be the final reduction

1428   product. In a word, studying the electronic structure of single atom and its interaction

1429   with intermediates is an effective way to reveal the selectivity of reduction products.

1430   Single-atom photocatalysts have great application potential, but it is worth noting

1431   that there are still some challenges here. For example, 2D materials have a large surface

1432   area, but it is difficult for single atom to achieve a uniform load over a large area. The

1433   surface energy of metal materials increases sharply with decreasing size, so metal

1434   aggregation has always been a major problem for single-atom photocatalysts. In

1435   addition, the bond between the single-atom metal site and the 2D material may become

1436   unstable as the reaction progresses, thereby affecting the single-atom loading.

1437   Therefore, the combination of single-atom photocatalysts and two-dimensional

1438   materials still has wide research space in the field of CO_2 photoreduction.

1439   7. Strategies for improving photocatalytic CO_2 reduction
1440   activity of 2D nanomaterials

1441   In order to effectively improve the activity of CO_2 photoreduction, the following

1442   aspects should be taken into account: (i) Rationally adjusting the band structure of the

1443   material; (ii) Accelerating the migration rate of photogenerated carriers and reducing

1444   the recombination rate of charge carriers; (iii) Promoting the CO_2 molecular adsorption

1445   and activation. In order to achieve these purposes, element doping, morphology control,

1446   vacancy engineering and heterostructure engineering are introduced. Table 5

1447   summarizes the typical material modification method and its performance improvement.

1448   **Table 5. Summary of the typical material modification method and its performance improvement.**

Methods	Classification	Function	Photocatalyst	Performance	Ref.
Elements doping	Metal elements	As the active sites and the electron trap.	MOF-525-Co	CO: 3.13 times higher than pristine MOF-525 CH_4: 5.93 times higher than pristine MOF-525	[252]
	Non-metallic elements	Adjust the energy band structure.	B/g-C_3N_4	CH_4: 32 times higher than pristine g-C_3N_4	[182]
Morphology control	Shape	Expose certain special groups; improve the specific surface.	ZIF-67	CO_2 adsorption capacity: rhombic dodecahedral morphology: 1.11mmol g^{-1} pitaya-like morphology: 0.81mmol g^{-1} leaf-like morphology: 1.16mmol g^{-1}	[253]
	Thickness	Affects the surface defects and coordination relationships.	Ni-Al LDH	The selectivity of CH_4: 27 nm: 0.1%; 5 nm: 2.4%; 1 nm: 16.5%	[78]
	Facets exposure	Improve the surface energy.	Cu_2O/WO_3-001	CO：11.7 μmol in 24 h	[254]
Vacancy	Non-metallic vacancy	Adjust the energy band structure;	V_N-g-C_3N_4	CO: 4 times higher than bulk g-C_3N_4	[255]

	engineering		promote the adsorption and activation of CO_2 molecules; weaken the exciton-effect.			
		Metallic vacancies	Adjust the electronic structure.	V_{Bi}-BiOBr	CO: 3.8 times higher than pristine BiOBr	256
Heterostructure engineering		0D/2D heterostructure	Promote the separation of photogenic electrons, reduce the carrier recombination rate.	TiO_{2-x}/g-C_3N_4	CO: 5 times higher than pristine g-C_3N_4	224
		1D/2D heterostructure	Promote the separation of photogenic electrons, reduce the carrier recombination rate.	CNTs/PCN	CO: 6.6 times higher than pristine g-C_3N_4 CH_4: 1.52 times higher than pristine g-C_3N_4	257
		2D/2D heterostructure	Promote the separation of photogenic electrons, reduce the carrier recombination rate.	g-C_3N_4/NiAl-LDH	CO: 5 times and 9 times higher than pristine g-C_3N_4 and NiAl-LDH	221

7.1 Element doping

Element doping is a very common strategy to improve the photocatalytic performance of 2D materials, which can significantly change the photoelectric properties of materials. It is worth noting that the influence of different doped elements on the properties of materials is different. In general, doped elements can be classified into two types: metal elements and non-metallic elements. The most widely studied metal doping elements are Fe, Na, K, Pt, Co, etc.,[258-263] while common non-metallic doping elements include C, O, B, S, N, etc.[264-269] In addition, the number and location of doping elements are also important factors affecting material properties.[31]

The metal element implanted in the 2D material can generally act as a photocatalytic active site and electronic trap, thereby becoming the central atom of the reaction. Zhang et al.[252] implanted Co atoms into MOF-525. Compared with the pristine MOF-525, the yields of CO (200.6 $\mu mol\ g^{-1}\ h^{-1}$) and CH_4 (36.67 $\mu mol\ g^{-1}\ h^{-1}$) were 3.13 times and 5.93 times that of the previous ones. The unsaturated Co site greatly enhanced the adsorption and activation of CO_2 molecules. In addition, Co site led to the migration of photogenic electrons from porphyrin to Co. Apart from this, the doping of the metal element can also change the selectivity of reduction products. Li and co-workers compared the effects of Au and Cu doped polymeric carbon nitride on the selectivity of CO_2 reduction products.[270] The experimental results showed that the reduction products of Au/CN mainly included CO and CH_3OH, while Cu/CN achieves a high

1470   selectivity of CH_4. After analysis, the covalent action between Cu atoms and CN was

1471   stronger than that between Au atoms and CN, which was more conducive to the deep

1472   reduction of CO_2. However, the electron transfer between the intermediates and Au/CN

1473   was weak, which led to the easy desorption of CH_3OH/CO from the material surface,

1474   and the reduction products were mainly CH_3OH and CO. What's more, metal doping

1475   also improves the light absorption capacity of materials. Tan et al.[271] implanted Ag/Pd

1476   alloy into N-doped TiO_2 nanosheets. UV−vis−NIR absorption spectra showed that

1477 Ag_xPd_y/TiO_2 photocatalysts greatly enhanced the visible light response. Compared with

1478   the absence of CH_4 production of pure TiO_2, the maximum CH_4 yield of Ag_xPd_y/TiO_2

1479   was 79.0 $\mu mol\ g^{-1}\ h^{-1}$.

1480   Non-metallic elements have the advantages of low price and wide sources, so the

1481   doping with non-metallic elements tends to be more attractive. Doping of certain

1482   nonmetallic elements will affect the electronic system of the material and change the

1483   bandgap of the semiconductor material. Huang et al.[272] doped C element into the lattice

1484   of g-BN nanosheets to form a ternary B-C-N structure. The DFT theoretical calculation

1485   showed that the indirect bandgap of pristine h-BN was 4.56 eV, and the bandgap of the

1486 $B_{11}C_{12}N_9$ was significantly reduced to 2.00 eV, which greatly enhanced the absorption

1487   of visible light. It is worth noting that the doping of foreign non-metallic elements will

1488   form a new photogenerated carrier recombination center, which will cause additional

1489   energy loss.[273] Therefore, self-doping of materials is an effective way to avoid this

1490   defect. Huang and co-workers successfully introduced C into the structure of g-C_3N_4

1491   and replaced part of N by self-doping.[274] The doping of C improved the availability of

1492   π-electron, and the bandgap of g-C_3N_4 was reduced from 2.75 eV to 2.58 eV. The

1493   material showed a good photocatalytic performance under green (λ = 500 nm) and

1494   yellow (λ = 550 nm) light. Since doping of different elements produces different effects,

1495   multi-element co-doping tends to impart a variety of effective properties to the material,

1496   and one element can also be used to compensate for defects caused by another

1497   element.[275] Samanta *et al.*[183] co-doped the C and O elements into the polymeric g-C_3N_4.

1498   Among them, C doping promoted the separation of charge carriers and increased the

1499   electrical conductivity of the material, while the O element expanded the absorption

1500   range of light and facilitated the adsorption of CO_2 molecules on the surface. The

1501   experimental results showed that the yield of CH_3OH within 6 h was 4.18 mmol g^{-1}.

1502   **7.2 Morphology control**

1503   In addition to elemental doping, morphology control is an effective method to

1504   change the properties of materials. The commonly used morphology control methods

1505   for 2D materials mainly include changing the thickness of 2D materials, changing the

1506   shape of materials, and controlling the exposed facets. Through morphological control,

1507   the electronic structure, active site, and light absorption capacity can be significantly

1508   changed.

1509   Constructing different shapes is one of the most common methods for morphology

1510 control. By constructing special shapes, it is more conducive to the exposure of certain

1511 special groups. For example, the groups containing unsaturated bonds and dangling

1512 bonds in TMDs are generally located at the edge of the nanosheet, rather than the

1513 surface or the basal planes of the bulk material. Based on this characteristic,

1514 photocatalytic performance can be improved by creating more edge positions. Meier *et*

1515 *al.*[276] successfully synthesized a MoS_2 nanoflower with a large number of edge planar

1516 slices by chemical vapor deposition. In the CO_2 photocatalytic reduction experiment,

1517 the diameter of nanoflowers increased with the increased of temperature rise rate (Fig.

1518 18d-18f). It is worth noting that when the heating rate reached $20°C$ min^{-1} (SZF-20), the

1519 excessive heating rate would lead to distortion of the crystal structure of the material,

1520 thus affecting the absorption of light. At 5 and $10°C$ min^{-1} (SZF-5 and SZF-10), the

1521 photocatalyst samples had abundant edge site abundance and defect crystal structure,

1522 and the activity of the photocatalyst reached the optimal point. By adjusting the shape

1523 of the material, the specific surface of the material can be improved; the active site can

1524 be increased; the adsorption capacity of the reactant can be enhanced. Low *et al.*[217]

1525 loaded TiO_2 nanoparticles onto 2D Ti_3C_2 to form a unique rise crust-like structure by a

1526 simple calcination method, and the loading of TiO_2 nanoparticles could be adjusted by

1527 controlling the calcination temperature. Fig. 18a-18c show dried TiO_2/Ti_3C_2 (TT0),

1528 TiO_2/Ti_3C_2 at $550°C$ (TT550) and $650°C$ (TT650) with a ramping rate of $10°C$ min^{-1},

1529 respectively. This unique morphological structure greatly increased the specific surface

1530 area of the material, thereby generating more active sites and facilitating the adsorption

1531   of CO_2 molecules. The experimental results showed that the optimal CH_4 yield of

1532 TiO_2/Ti_3C_2 samples was 2.8 and 3.7 times of pure TiO_2 and P25, respectively. Besides,

1533   Wang and co-workers specifically compared the effects of different shapes of MOF

1534   materials as co-catalysts on the CO_2 photoreduction performance.[253] The rhombic

1535   dodecahedral morphology ZIF-67_1 (Fig. 18g), the pitaya-like morphology ZIF-67_2

1536   (Fig. 18h), and the leaf-like morphology ZIF-67_3 (Fig. 18i) were synthesized by using

1537   different volume ratios of CH_3OH and H_2O as solvents. At 100 KPa, ZIF-67_3 had the

1538   best adsorption capacity for CO_2, which was 1.16 mmol g^{-1}.
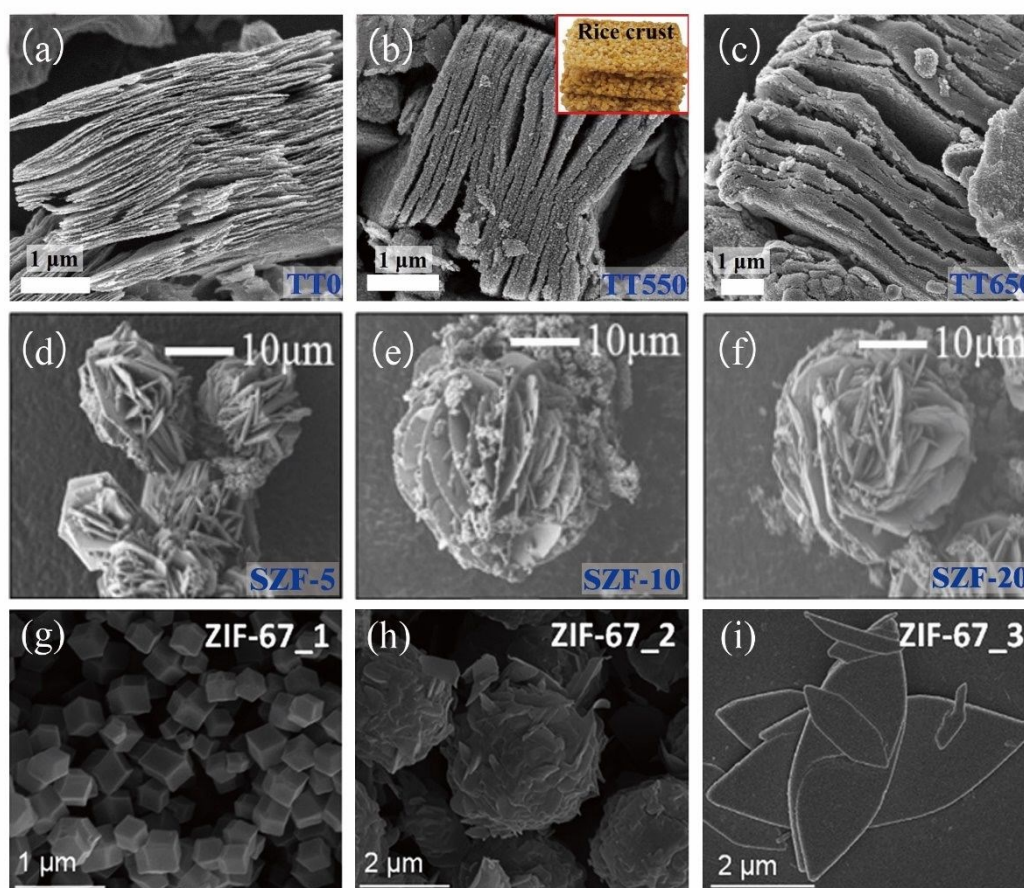
1539

1540   **Fig. 18. Field emission scanning electron microscope (FESEM) images of (a) TT0,**

1541 **(b) TT550 and (c) TT650. Reproduced with permission from ref. [217], copyright**

1542 **2018 Elsevier. Scanning electron microscope (SEM) images of (d) SZF-5, (e) SZF-7,**

1543 **(f) SZF-20. Reproduced with permission from ref. [276], copyright 2018 American**

1544 **Chemical Society. Scanning electron microscope (SEM) images of (g) ZIF-67_1, (h)**

1545 **ZIF-67_2, and (i) ZIF-67_3. Reproduced with permission from ref. [253], copyright**

1546 **2018 Royal Society of Chemistry.**

1547   For 2D materials, the thickness is an important factor affecting its properties. The

1548 thickness of the material affects the surface defects and coordination relationships.

1549 Therefore, thickness control is an important aspect of morphology control. Tan *et al.*[78]

1550 synthesized a series of Ni-Al LDH with the thickness ranging from 27 nm to 5 nm to 1

1551 nm. Through CO_2 photocatalytic reduction experiments, it was found that the

1552 selectivity of H_2 in the product decreased from 43.8% to 26.5% to 13.3%, and the

1553 selectivity of methane was increased from 0.1% to 2.4% to 16.5%. Therefore, as the

1554 thickness of Ni-Al LDH decreased, the competitive reaction of HER was effectively

1555 inhibited, and the selectivity of methane was improved. The main reason for this

1556 phenomenon was the increase of the coordination unsaturated metal and hydroxyl

1557 defects on the surface of LDH as the thickness decreases.

1558   In parallel, facets exposure is also one of the ways to control morphology. Facets

1559 are closely related to the surface energy of the material, and the exposure of high-energy

1560 facets can greatly improve the surface energy.[277, 278] In general, the low-energy facets

1561 of a material tend to dominate in order to keep its stability. For example, Anatase TiO_2

1562 crystals tend to be dominated by the {101} low-energy facets (0.44 J m^{-2}) to maintain

1563 thermodynamic stability without exposing {001} high-energy facets (0.90 J m^{-2}).[279] Shi

1564 et al.[254] modified WO_3 nanosheets with Cu_2O and studied the effect of WO_3 with or

1565 without dominant {001} facets on photocatalytic reduction of CO_2. The analysis

1566 showed that the {001} facets of WO_3 promoted the transfer of photogenerated holes to

1567 H_2O molecules, which was beneficial to the oxidation process of H_2O molecules. The

1568 maximum CO yield of Cu_2O/WO_3-001 material was 11.7 μmol in 24 h, which was

1569 higher than Cu_2O/WO_3 without dominant {001} facets.

1570 **7.3 Vacancy engineering**

1571 For 2D materials, because the thickness is reduced to the nanometer level, it will

1572 lead to the discontinuity of the crystal, and a large number of atoms are exposed on the

1573 surface, resulting in atomic vacancies and surface dangling bonds.[280] The introduction

1574 of defects can significantly change the physicochemical properties and photoelectric

1575 properties of materials, thus promoting their application in the field of photocatalysis.

1576 Different kinds of vacancies will have different effects on the material. The types of

1577 vacancies can be divided into metal vacancies and non-metal vacancies.[31]

1578 At present, there are many researches on non-metallic vacancy, and it is relatively

1579 easy to introduce non-metallic vacancy. Firstly, the energy band structure of the

1580 material can be adjusted through the introduction of vacancies. The N vacancy can

1581　adjust the band structure by introducing the midgap states. Tu *et al.*[255] calcined bulk g-

1582　C_3N_4 from 475℃ to 550℃ under the atmosphere of H_2 to produce g-C_3N_4 nanosheets

1583　with different N vacancy densities. With the increased of temperature, C/N gradually

1584　increased, indicating the formation of N vacancies (Fig. 19a). Fig. 19b showed that the

1585　proportion of C-N=C and N-$(C)_3$ decreased with the increase of temperature, reflecting

1586　that the missing N atom may be located at the two-coordinated lattice sites. Through

1587　experimental analysis and DFT theoretical calculations, it was found that the

1588　introduction of N vacancies led to a midgap state under the CB of g-C_3N_4 (Fig. 19c and

1589　19d). The photogenerated electrons of the VB would transit to the midgap states, which

1590　played a role similar to narrowing the bandgap (Fig. 19c, path 1). The midgap states

1591　could also receive electrons from the CB, thereby accelerating the separation of

1592　photogenerated electrons and holes (Fig. 19c, path 2). However, as the N vacancies

1593　increased, the position of the midgap states would become deeper. When too many N

1594　vacancies were introduced, the midgap states would become the recombination site (Fig.

1595　19c, path 3). When the density of N vacancy was optimal, the yield of CO was 4 times

1596　higher than the bulk g-C_3N_4. In addition to the adjustment of the energy band structure,

1597　the introduction of vacancies will also promote the adsorption and activation of CO_2

1598　molecules. Shen *et al.*[281] introduced C vacancies by heating g-C_3N_4 under NH_3

1599　atmosphere. The experimental and theoretical calculations showed that the CO_2

1600　adsorption energy of sample GCN510 with C vacancies was -0.463 eV, which was more

1601　negative than pure GCN (-0.183 eV). Furthermore, The C=O bond length of the CO_2

1602   molecule adsorbed on the surface of the GCN with C vacancies was 1.177 Å, which

1603   was greater than the initial C=O bond length (1.169 Å). It can be seen that the C

1604   vacancies promoted the adsorption and activation of CO_2 molecules. Moreover, the C

1605   vacancies weaken the exciton-effect, which promoted the generation of carriers. The

1606   experimental results showed that the yield of CO was 4.18 μmol g^{-1} h^{-1}, which was 2.3

1607   times higher than pristine GCN.

1608
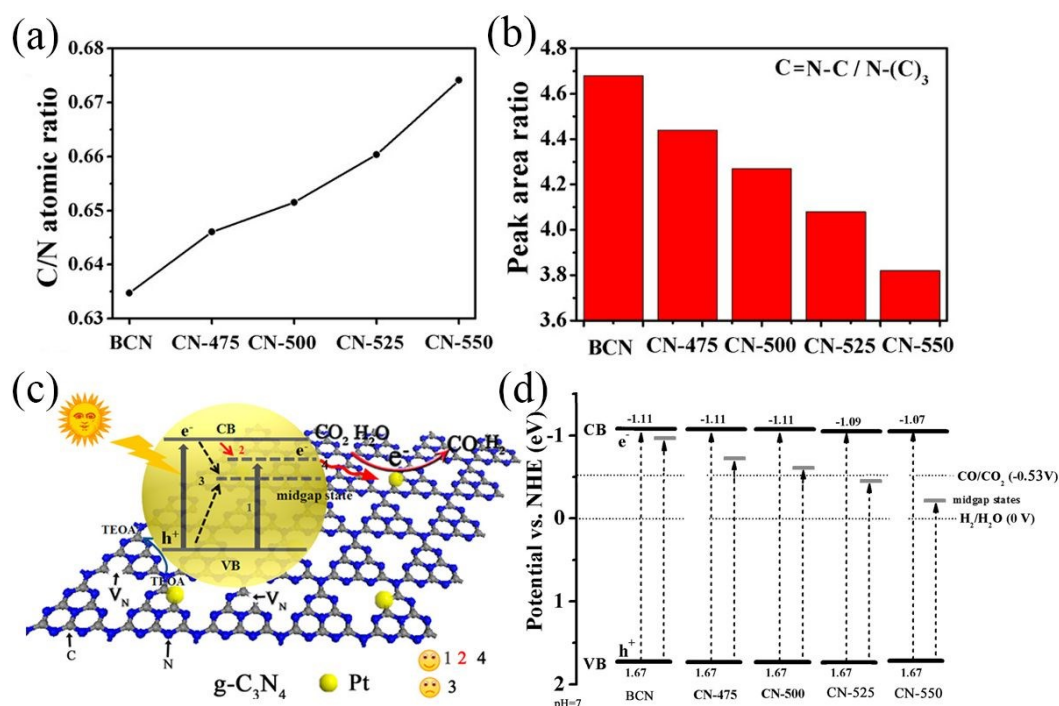
1609 **Fig. 19. (a) C/N atomic ratio of BCN and CN-x from element analysis. (b) The peak**

1610 **area ratio of C=N-C groups to N-(C)$_3$ of BCN and CN-x from XPS analysis. (c)**

1611 **Schematic illustrates the schematic diagram of g-C$_3$N$_4$ photocatalytic reduction of**

1612 **CO$_2$ with N vacancy. The Numbers 1, 2, 3, and 4 reflect four paths of electron**

1613 **excitation. (d) Schematic illustration of the electronic structure of BCN and CN-**

1614 **x. Reproduced with permission from ref. [255]. Copyright 2017 American Chemical**

1615 **Society.**
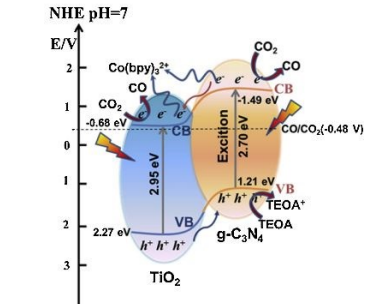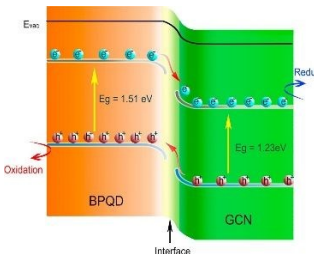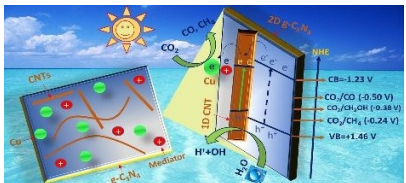
1616   In addition to non-metallic vacancies, metal cation vacancies can also change the

1617 electronic structure and physicochemical properties of materials due to the diversity of

1618 electronic configurations and orbital distribution.[282] However, it is more difficult to

1619 form metal cation vacancies because the formation energy is relatively large, which

1620 leads to relatively little research on cation vacancies. Di and co-workers successfully

1621 synthesized BiOBr nanosheets containing Bi vacancies by controlled long carbon chain

1622 ionic liquid-assisted synthesis.[256] The introduction of Bi vacancies changed the

1623 electronic structure. The density of states (DOS) of BiOBr VB edge with Bi vacancies

1624 (V_{Bi}-BiOBr) was higher, which means that more carriers of V_{Bi}-BiOBr would

1625 participate in CO_2 reduction reaction. At the same time, more negative CB gave V_{Bi}-

1626 BiOBr a stronger reducibility. The CO temperature programmed desorption (TPD)

1627 pattern showed that V_{Bi}-BiOBr has a lower onset CO desorption temperature, and the

1628 total amount of CO in the product was 3.8 times that of BiOBr nanosheets. In addition

1629 to the introduction of single metal atomic vacancies, Di and co-workers introduced a

1630 Bi-O vacancy pair in ultrathin $BiMoO_6$ nanosheets by template-directed method.[283]

1631 Similar to the introduction of Bi vacancies in BiOBr, the Bi-O vacancy pair also

1632 improved the electronic structure of the material and increased the carrier concentration.

1633 In addition, the Bi-O vacancy pair on the surface of the material could serve as a capture

1634   center for photogenerated electrons, thereby promoting the separation of

1635   photogenerated charge carriers. The results showed that the yield of CO was 3.62 μmol

1636 $g^{-1} h^{-1}$. Therefore, whether it is a metal vacancy or a non-metal vacancy, after reasonable

1637   setting, it can be an effective means to improve the photoreduction performance of CO_2.

1638   **7.4 Heterostructure engineering**

1639   Due to the limitation of intrinsic properties, the photocatalytic effect of 2D

1640   materials with single components is often unsatisfactory. Therefore, the formation of

1641   heterostructure between 2D materials and other materials is an excellent strategy to

1642   make up for the shortcomings of single components. In general, conventional

1643   heterostructure can be divided into three categories: type-Ⅰ (straddling gap), type-Ⅱ

1644   (staggered gap), and type-Ⅲ (broken gap). In recent years, there have been some studies

1645   on new p-n heterojunctions and Z-scheme heterojunctions. For 2D materials, they can

1646   be divided into 0D/2D (point contact) heterojunctions, 1D/2D (line contact)

1647   heterojunctions, and 2D/2D (face contact) heterojunctions according to the different

1648   contact methods between different materials (Table 6).[284]

1649 **Table 6. List of the synthesis, type and schematic diagram of heterojunction photocatalyst.**

Classification	Composites	Synthetic methods	Heterojunction type	Schematic diagram	Ref.
0D/2D	TiO$_{2-x}$/g-C$_3$N$_4$	In-situ pyrolysis	Conventional type Ⅱ		224
	BPQD/GCN		Conventional type Ⅱ		285
1D/2D	CNTs/PCN	Impregnation	Conventional type Ⅱ		257

	TiO_2/MoS_2	Hydrothermal	Conventional type Ⅱ		136
2D/2D	$g\text{-}C_3N_4/Ni\ Al\text{-}LDH$	Hydrothermal	Conventional type Ⅱ		221
	$Bi_2WO_6/RGO/g\text{-}C_3N_4$	Hydrothermal	Z-scheme		286
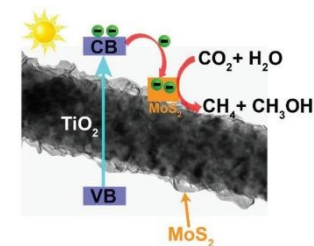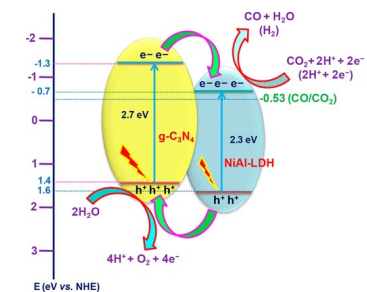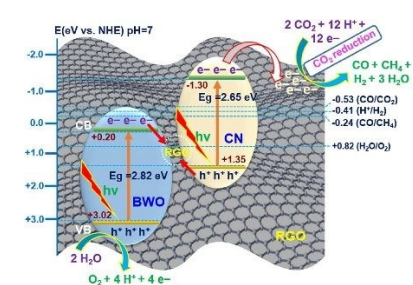
1651   Coupling 0D nanoparticles on the surface of 2D materials is an effective method

1652   to construct heterojunction. Shi *et al.*[224] coupled 0D TiO_2 quantum dots rich in O defects

1653   on g-C_3N_4 nanosheets to form a 0D/2D heterojunction (TiO_{2-x}/g-C_3N_4) for CO_2

1654   photoreduction. In this structure, photogenerated electrons were transferred from the

1655   CB of g-C_3N_4 to the CB of TiO_2, while the migration direction of photogenerated holes

1656   was opposite. Electron transfer occurred on the subpicosecond time scale, which greatly

1657   promoted the separation of electrons. The CO yield of TiO_{2-x}/g-C_3N_4 was 77.8 $\mu mol\ g^{-1}$

1658 h^{-1}, which was 5 times that of the pure g-C_3N_4. Similarly, Kong and co-workers

1659   successfully synthesized 0D/2D (BPQD)/g-C_3N_4 type-Ⅱ heterojunction.[285] Due to the

1660   staggered energy bands, the electrons in the CB of BPQD were transferred to the CB

1661   of g-C_3N_4, and the holes in the VB of g-C_3N_4 were transferred to the VB of BPQD. This

1662   heterojunction reduced the carrier recombination rate and greatly improved the

1663   photocatalytic efficiency. However, it is worth noting that the distribution of 0D

1664   nanoparticles on the surface of the 2D material is limited, and it is difficult to achieve

1665   comprehensive coverage. Such limited contact often fails to give full play to the

1666   advantages of heterostructures, so the separation efficiency of photogenerated carriers

1667   is limited.

1668   Compared with 0D nanoparticles, 1D materials tend to have larger specific surface

1669   area, higher aspect ratio and better carrier mobility.[86] There are some studies on the

1670   application of 1D/2D heterojunction in photocatalysis. For example, Tahir *et al.*[257] used

1671   1D carbon nanotubes (CNTs) to modify 2D protonated g-C$_3$N$_4$ (PCN), and then

1672   embedded Cu nanoparticles in the structure. The CNTs not only have a large specific

1673   surface area and a porous structure, but also have excellent thermal and electrical

1674   properties. In this heterostructure, CNTs acted as electron acceptors and received

1675   photogenerated electrons from g-C$_3$N$_4$. The experimental results showed that the

1676   highest CO yield of CNTs/PCN was 410 μmol g$_{cat}^{-1}$ h^{-1}, which was 6.6 times that of

1677   pure g-C$_3$N$_4$, while the yield of CH$_4$ was 1.52 times that of g-C$_3$N$_4$. Moreover, Xu *et*

1678   *al.*[136] constructed 1D/2D TiO$_2$/MoS$_2$ heterojunction by in-situ growth of MoS$_2$

1679   nanosheets on TiO$_2$ nanofiber. The optimal yields of CH$_4$ and CH$_3$OH were 2.86 and

1680   2.55 μmol g^{-1} h^{-1}, respectively. When pure TiO$_2$ nanofibers were used as photocatalysts,

1681   the products contained only CH$_3$OH (0.72 μmol g^{-1} h^{-1}). In this structure, electrons

1682   tended to transfer from TiO$_2$ nanofibers to MoS$_2$ nanosheets. MoS$_2$ nanosheets

1683   increased the surface area of the material, provided more reactive sites, and facilitated

1684   the adsorption and activation of CO$_2$ molecules.

1685   Compared with the above two types of heterojunctions, 2D/2D heterojunctions

1686   have stronger physical and electronic coupling due to their relatively larger contact

1687   surfaces. There are special studies on the effect of different dimensions of materials on

1688   the electron transfer at the heterojunction interface. For example, Sun *et al.*[287] compared

1689   the effects of 0D/2D P25/graphene, 1D/2D TiO$_2$ nanotubes/graphene, and 2D/2D TiO$_2$

1690   nanosheets/graphene on photocatalytic performance. Through experimental analysis,

1691   the interfacial electron transfer rates on the surface of 0D/2D, 1D/2D, and 2D/2D

1692   heterojunction were 1.15×10^8 s^{-1}, 3.47×10^8 s^{-1}, and 1.06×10^9 s^{-1}, respectively. 2D/2D

1693   heterojunctions have obvious advantages in terms of electron transfer. Tonda and co-

1694   workers synthesized the g-C$_3$N$_4$/NiAl-LDH 2D/2D heterostructure by the strong

1695   electrostatic interaction.[221] Through VB-XPS, it was shown that the minimum CB value

1696   of NiAl-LDH was lower than g-C$_3$N$_4$, while the maximum VB value of g-C$_3$N$_4$ was

1697   higher than NiAl-LDH. The photogenerated electrons were transferred from the CB of

1698   g-C$_3$N$_4$ to the CB of NiAl-LDH, while the holes formed on the VB of NiAl-LDH could

1699   enter the VB of g-C$_3$N$_4$. When the content of NiAl-LDH was 10%, the yield of CO

1700   reached a maximum of 8.2 μmol g^{-1} h^{-1}. Moreover, in order to further promote the

1701   photocatalytic properties of materials, the formation of heterojunction by combination

1702   of three materials is also a method of material design. Jo et al.[286] successfully

1703   synthesized Bi$_2$WO$_6$/RGO/g-C$_3$N$_4$ (BRC) 2D/2D/2D heterojunction through the two-

1704   step hydrothermal method (Fig. 20a-20e). It is worth noting that, unlike traditional

1705   heterojunctions, Z-scheme heterojunctions were formed between Bi$_2$WO$_6$ and g-C$_3$N$_4$.

1706   The photogenetic electrons in the CB of Bi$_2$WO$_6$ were transferred to the VB of g-C$_3$N$_4$

1707   through RGO, so that the oxidation and reduction sites were spatially separated. The

1708   redox reactions occurred in the VB of Bi$_2$WO$_6$ and the CB of g-C$_3$N$_4$, respectively.

1709   RGO acted as both a carrier and a medium for electron transfer, facilitating the transfer

1710   of electrons between semiconductor materials (Fig. 20g). When the content of RGO

1711   and Bi$_2$WO$_6$ in the material was 1 wt.% and 15 wt.% , respectively, the yield of CO

1712 reached a maximum value of 15.96 μmol g^{-1} h^{-1}, which was 15 times that of pristine g-

1713 C$_3$N$_4$, and the maximum yield of CH$_4$ was 2.51 μmol g^{-1} h^{-1} (Fig. 20f).

1714
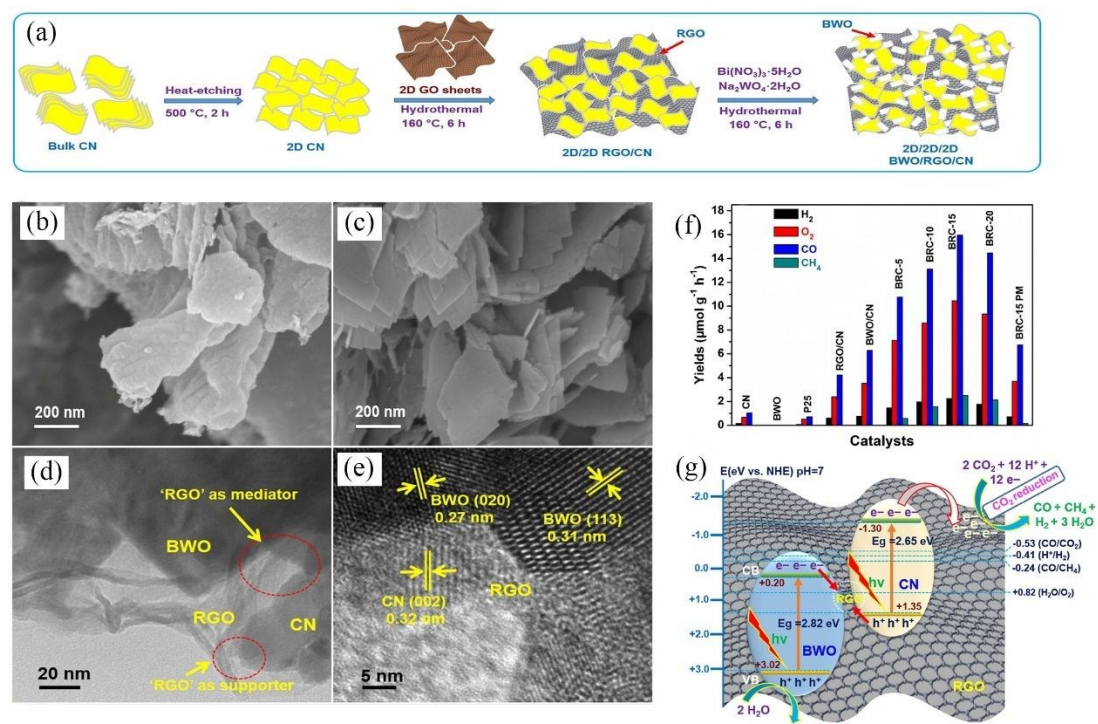
1715 **Fig. 20. (a) Schematic diagram of synthesis process of Bi$_2$WO$_6$/RGO/g-C$_3$N$_4$**

1716 **heterojunction. (b) and (c) SEM images of BRC-15 samples. (d) and (e) HR-TEM**

1717 **images of the BRC-15 samples. (f) The bar chart reflects the comparison of the**

1718 **yield of H$_2$, O$_2$, CO, and CH$_4$ after 5 h of visible light illumination. (g) Schematic**

1719 **diagram reflects the mechanism of photocatalytic reduction of CO$_2$ by**

1720 **Bi$_2$WO$_6$/RGO/g-C$_3$N$_4$. Reproduced with permission from ref. [286]. Copyright 2018**

1721 **Elsevier.**

1722 ## 8. Conclusions and perspectives

1723 Because sufficient clean solar exists to power energy for photocatalysis, further

1724   research on the photocatalytic reduction of CO_2 represents a firm grasp of the

1725   opportunity that executes solutions to CO_2 pollution and energy issues. Among

1726   photocatalysts, 2D materials are a unique category, and have been favored by

1727   researchers for their remarkable optoelectronic and structural properties. In this review,

1728   recent advances in two-dimensional materials for CO_2 photoreduction and related

1729   principles are described in detail. Despite considerable achievements have been made

1730   over the past few years, further research is needed to realize the large-scale application

1731   of 2D materials in the photocatalytic CO_2 conversion to achieve a sustainable future.

1732   The C atom in CO_2 is in the highest valence state, which means that CO_2 molecules

1733   will produce many different products during the reduction process. There are many

1734   factors that affect the product selectivity, including the adsorption and activation of CO_2,

1735   photoexcitation properties, the bandgap structure, the reaction sites on the surface, the

1736   adsorption and desorption of intermediates, etc. The involvement of many factors has

1737   led to extremely complicated control of product selectivity. In recent years, many

1738   measures have been taken to increase the selectivity of products, but the overall effect

1739   has been poor. Lack of a relatively complete product analysis system is a key obstacle

1740   to the study of product selectivity. Currently, CO, CH_4, and H_2 are mainly detected in

1741 CO_2 reaction products, while some liquid products and multi-carbon products are more

1742   difficult to detect, such as CH_3OH, $HCOOH$, CH_3CH_2OH, CH_3CH_2CHO, etc. They are

1743   significant for studying the reduction pathways and selectivity. Only by analyzing all

1744   the reduced products, including those with a low concentration, can we further explore

1745   the mechanism of CO_2 photocatalysis, which is conducive to improving the yield of

1746   target products.

1747   In the course of experimental research, the yield of reduced products can generally

1748   reach a few $\mu mol\ g^{-1}\ h^{-1}$, the yield is difficult to meet the requirements in practical

1749   applications. At the same time, there is a gap between the concentration of CO_2 used in

1750   many experimental studies and the actual atmosphere. The concentration of CO_2 in the

1751   atmosphere is lower than that in the experiment, so the prepared photocatalyst is

1752   generally difficult to achieve the desired effect under the condition of low concentration

1753   of CO_2. Therefore, improving the reduction yield of the product should be a

1754   continuously pursued goal.

1755   Ultrathin thickness is a typical and distinct feature of 2D materials, reducing the

1756   thickness can increase the specific surface area, reduce the migration distance of

1757   photogenerated carriers, and increase the elastic strain tolerance. However, the quantum

1758   confinement effect of the ultrathin structure will reduce the visible light absorption

1759   range and increase the carrier recombination rate. Therefore, the best photocatalytic

1760   performance can be obtained only when the thickness of 2D materials is suitable. The

1761   experiment of photocatalytic reduction of CO_2 by 2D materials with different thickness

1762   is the next step to explore this problem.

1763   The durability and recyclability of 2D materials is important if any wide, realistic

1764   application is envisaged. In the laboratory, we can prepare 2D photocatalysts with a

1765   certain morphological structure, but in practical commercial or industrial applications,

1766   it is very difficult to prepare 2D materials with high purity and controllable uniform

1767   morphology and size. At present, chemical vapor deposition (CVD) and high vacuum

1768   deposition are two commonly used methods to prepare 2D materials, but both have

1769   drawbacks of low yield and high cost. As a relatively new method, liquid phase

1770   stripping often results in relatively poor product quality. Therefore, the recycling of

1771   materials is an important means to reduce costs, and the research on material

1772   preparation method is still a long way.

1773   Some advanced in-situ and ex-situ characterization techniques should be applied

1774   to the development and application of 2D materials. Through characterization

1775   technology, the morphology, defects, and active sites of materials can be effectively

1776   analyzed, so as to study the relationship between structure and properties. For example,

1777   near atomic scale photocatalysts can be studied by high-angle annular dark field

1778   scanning TEM (HAADF-STEM) to investigate the distribution of atoms on 2D material

1779   surfaces. X-ray absorption near-edge structure (XANES) can be used to explore the

1780   defects and strains of materials. Extended X-ray absorption fine structure (EXAFS) is

1781   a common characterization technology for detecting structural information of

1782   photocatalytic materials, especially for photocatalysts containing single atoms or

1783   clusters. Electron spin resonance (ESR) is a strong method for detection of active free

1784   radicals on the surface of photocatalysts. Femtosecond transient absorption (TA)

1785   spectroscopy can be used to study the electron-hole recombination kinetics of

1786   semiconductors. X-ray photoelectron spectroscopy (XPS) using a synchrotron light

1787   source is a powerful tool to inspect the photoinduced carrier transfer. At present,

1788   advanced characterization is an effective method to study reaction intermediates, which

1789   provides a good method to study reaction mechanism and product selectivity.

1790   In summary, the generation of hydrocarbons from CO_2 by employing the 2D

1791   photocatalysts and solar as the energy input will be a promising technology. Progress

1792   in synthesis and modification methods for the 2D materials coupled with a more in-

1793   depth understanding of CO_2 photoreduction mechanisms has enabled the rational

1794   design of photocatalyst with excellent activity and selectivity. But the current research

1795   is only at the experimental level, there are still huge challenges to achieve large-scale

1796   applications. We are confident that the constant progress in 2D materials synthesis,

1797   modification, characterization, and mechanism analysis is laying the groundwork for

1798 CO_2 pollution control as well as energy conversion.

1799   **Conflicts of interest**

1800   There are no conflicts of interest to declare.

1801   **Acknowledgements**

Journal of Materials Chemistry A Accepted Manuscript

References

1. K. Li, X. An, K. H. Park, M. Khraisheh and J. Tang, *Catal. Today*, 2014, **224**, 3-12.

2. C. Hepburn, E. Adlen, J. Beddington, E. A. Carter, S. Fuss, N. Mac Dowell, J. C. Minx, P. Smith and C. K. Williams, *Nature*, 2019, **575**, 87-97.

3. C. Zhang, G. Zeng, D. Huang, C. Lai, M. Chen, M. Cheng, W. Tang, L. Tang, H. Dong and B. Huang, *Chem. Eng. J.*, 2019, **373**, 902-922.

4. B. P. Spigarelli and S. K. Kawatra, *J. CO₂ Util.*, 2013, **1**, 69-87.

5. J. Wu, Y. Huang, W. Ye and Y. Li, *Adv. Sci.*, 2017, **4**, 1700194.

6. F. M. Mota and D. H. Kim, *Chem. Soc. Rev.*, 2019, **48**, 205-259.

7. Q. Wang, Y. Lei, D. Wang and Y. Li, *Energy Environ. Sci.*, 2019, **12**, 1730-1750.

8. R. M. Evans, B. Siritanaratkul, C. F. Megarity, K. Pandey, T. F. Esterle, S. Badiani and F. A. Armstrong, *Chem. Soc. Rev.*, 2019, **48**, 2039-2052.

9. X. Li, J. Yu, M. Jaroniec and X. Chen, *Chem. Rev.*, 2019, **119**, 3962-4179.

10. J. Shi, Y. Jiang, Z. Jiang, X. Wang, X. Wang, S. Zhang, P. Han and C. Yang, *Chem. Soc. Rev.*, 2015, **44**, 5981-6000.

11. F. P. García de Arquer, C.-T. Dinh, A. Ozden, J. Wicks, C. McCallum, A. R. Kirmani, D.-H. Nam, C. Gabardo, A. Seifitokaldani, X. Wang, Y. C. Li, F. Li, J. Edwards, L. J. Richter, S. J. Thorpe, D. Sinton and E. H. Sargent, *Science*, 2020, **367**, 661-666.

12. M. Liras, M. Barawi and A. Víctor, *Chem. Soc. Rev.*, 2019, **48**, 5454-5487.

13. Y. Zhou, W. Wang, C. Zhang, D. Huang, C. Lai, M. Cheng, L. Qin, Y. Yang, C. Zhou, B. Li, H. Luo and D. He, *Adv. Colloid Interface Sci.*, 2020, **279**, 102144.

14. C. Zhang, C. Lai, G. Zeng, D. Huang, C. Yang, Y. Wang, Y. Zhou and M. Cheng, *Water Res.*, 2016, **95**, 103-112.

15. F. Qin, Y. Peng, G. Song, Q. Fang, R. Wang, C. Zhang, G. Zeng, D. Huang, C. Lai, Y. Zhou, X. Tan, M. Cheng and S. Liu, *J. Hazard. Mater.*, 2020, **398**, 122816.

1844   16.   T. Inoue, A. Fujishima, S. Konishi and K. Honda, *Nature*, 1979, **277**,
1845   637-638.

1846   17.   A. Meng, L. Zhang, B. Cheng and J. Yu, *Adv. Mater.*, 2019, **31**,
1847   1807660.

1848   18.   M. Wang, J. Iocozzia, L. Sun, C. Lin and Z. Lin, *Energy Environ. Sci.*,
1849   2017, **10**, 2041-2041.

1850   19.   X. Li, J.-L. Shi, H. Hao and X. Lang, *Appl. Catal. B-Environ.*, 2018,
1851   **232**, 260-267.

1852   20.   X. Li, P. Xu, M. Chen, G. Zeng, D. Wang, F. Chen, W. Tang, C. Chen,
1853   C. Zhang and X. Tan, *Chem. Eng. J.*, 2019, **366**, 339-357.

1854   21.   P. Zhou, Q. Zhang, Z. Xu, Q. Shang, L. Wang, Y. Chao, Y. Li, H.
1855   Chen, F. Lv and Q. Zhang, *Adv. Mater.*, 2020, **32**, 1904249.

1856   22.   A. Di Mauro, M. Cantarella, G. Nicotra, V. Privitera and G.
1857   Impellizzeri, *Appl. Catal. B-Environ.*, 2016, **196**, 68-76.

1858   23.   B. Shao, X. Liu, Z. Liu, G. Zeng, W. Zhang, Q. Liang, Y. Liu, Q. He,
1859   X. Yuan and D. Wang, *Chem. Eng. J.*, 2019, **374**, 479-493.

1860   24.   K. S. Novoselov, A. K. Geim, S. V. Morozov, D. Jiang, Y. Zhang, S.
1861   V. Dubonos, I. V. Grigorieva and A. A. Firsov, *Science*, 2004, **306**, 666-669.

1862   25.   Y. Wang, M. Qiu, M. Won, E. Jung, T. Fan, N. Xie, S.-G. Chi, H.
1863   Zhang and J. S. Kim, *Coord. Chem. Rev.*, 2019, **400**, 213041.

1864   26.   M. D. Stoller, S. Park, Y. Zhu, J. An and R. S. Ruoff, *Nano Lett.*, 2008,
1865   **8**, 3498-3502.

1866   27.   J. Fu, B. Zhu, C. Jiang, B. Cheng, W. You and J. Yu, *Small*, 2017, **13**,
1867   1603938.

1868   28.   G. Liu, C. Zhen, Y. Kang, L. Wang and H.-M. Cheng, *Chem. Soc.
1869   Rev.*, 2018, **47**, 6410-6444.

1870   29.   J. Pang, R. G. Mendes, A. Bachmatiuk, L. Zhao, H. Q. Ta, T.
1871   Gemming, H. Liu, Z. Liu and M. H. Rummeli, *Chem. Soc. Rev.*, 2019, **48**, 72-
1872   133.

1873   30.   X. Chang, T. Wang and J. Gong, *Energy Environ. Sci.*, 2016, **9**, 2177-
1874   2196.

1875   31.   J. Xiong, P. Song, J. Di and H. Li, *Appl. Catal. B-Environ.*, 2019, **256**,
1876   117788.

1877   32.   Z. Sun, N. Talreja, H. Tao, J. Texter, M. Muhler, J. Strunk and J. Chen,
1878   *Angew. Chem. Int. Ed.*, 2018, **57**, 7610-7627.

1879   33.   Y. Chen, G. Jia, Y. Hu, G. Fan, Y. H. Tsang, Z. Li and Z. Zou, *Sustain.*
1880   *Energ. Fuels*, 2017, **1**, 1875-1898.

1881   34.   M. Marszewski, S. Cao, J. Yu and M. Jaroniec, *Mater. Horizons*, 2015,
1882   **2**, 261-278.

1883   35.   P. S. Surdhar, S. P. Mezyk and D. A. Armstrong, *J. Phys. Chem.*, 1989,
1884   **93**, 3360-3363.

1885   36.   S. Yu, X.-B. Fan, X. Wang, J. Li, Q. Zhang, A. Xia, S. Wei, L.-Z. Wu,
1886   Y. Zhou and G. R. Patzke, *Nat. Commun.*, 2018, **9**, 1-10.

1887   37.   A.   Sandhu,   *Nat.   Nanotechnol.*,   2006,   DOI:
1888   https://doi.org/10.1038/nnano.2006.21.

1889   38.   M.-P. Jiang, K.-K. Huang, J.-H. Liu, D. Wang, Y. Wang, X. Wang,
1890   Z.-D. Li, X.-Y. Wang, Z.-B. Geng, X.-Y. Hou and S.-H. Feng, *Chem*, 2020,
1891   DOI: https://doi.org/10.1016/j.chempr.2020.06.033.

1892   39.   S.-C. Lin, C.-C. Chang, S.-Y. Chiu, H.-T. Pai, T.-Y. Liao, C.-S. Hsu,
1893   W.-H. Chiang, M.-K. Tsai and H. M. Chen, *Nat. Commun.*, 2020, **11**, 3525.

1894   40.   S. Xu and E. A. Carter, *Chem. Rev.*, 2018, **119**, 6631-6669.

1895   41.   S. Kattel, P. Liu and J. G. Chen, *J. Am. Chem. Soc.*, 2017, **139**, 9739-
1896   9754.

1897   42.   M. J. L. Ginés, A. J. Marchi and C. R. Apesteguía, *Appl. Catal. A-*
1898   *Gen.*, 1997, **154**, 155-171.

1899   43.   L. K. Rihko-Struckmann, A. Peschel, R. Hanke-Rauschenbach and K.
1900   Sundmacher, *Ind. Eng. Chem. Res.*, 2010, **49**, 11073-11078.

1901   44.   D. Pakhare and J. Spivey, *Chem. Soc. Rev.*, 2014, **43**, 7813-7837.

1902   45.   F. Wang, M. Wei, D. G. Evans and X. Duan, *J. Mater. Chem. A*, 2016,
1903   **4**, 5773-5783.

1904   46.   M. Khalil, J. Gunlazuardi, T. A. Ivandini and A. Umar, *Renew. Sust.*
1905   *Energ. Rev.*, 2019, **113**, 109246.

1906   47.   Y. Wang, D. He, H. Chen and D. Wang, *J. Photochem. Photobiol. C-*
1907   *Photochem. Rev.*, 2019, **40**, 117-149.

1908   48.   Z. Fu, Q. Yang, Z. Liu, F. Chen, F. Yao, T. Xie, Y. Zhong, D. Wang,
1909   J. Li and X. Li, *J. CO$_2$ Util.*, 2019, **34**, 63-73.

1910   49.   W. Fan, Q. Zhang and Y. Wang, *Phys. Chem. Chem. Phys.*, 2013, **15**,
1911   2632-2649.

1912   50.   L. Wang, W. Chen, D. Zhang, Y. Du, R. Amal, S. Qiao, J. Wu and Z.
1913   Yin, *Chem. Soc. Rev.*, 2019, **48**, 5310-5349.

1914   51.   S. H. Yoon, U. Kang, H. Park, A. Abdel-Wahab and D. S. Han, *Catal.*
1915   *Today*, 2019, **335**, 345-353.

1916   52.   S. Zhang, P. Kang and T. J. Meyer, *J. Am. Chem. Soc.*, 2014, **136**,
1917   1734-1737.

1918   53.   R. Kortlever, J. Shen, K. J. P. Schouten, F. Calle-Vallejo and M. T.
1919   Koper, *J. Phys. Chem. Lett.*, 2015, **6**, 4073-4082.

1920   54.   M. F. Baruch, J. E. Pander III, J. L. White and A. B. Bocarsly, *ACS*
1921   *Catal.*, 2015, **5**, 3148-3156.

1922   55.   Z. Sun, T. Ma, H. Tao, Q. Fan and B. Han, *Chem*, 2017, **3**, 560-587.

1923   56.   X. Nie, M. R. Esopi, M. J. Janik and A. Asthagiri, *Angew. Chem. Int.*
1924   *Ed.*, 2013, **52**, 2459-2462.

1925   57.   A. A. Peterson, F. Abild-Pedersen, F. Studt, J. Rossmeisl and J. K.
1926   Nørskov, *Energy Environ. Sci.*, 2010, **3**, 1311-1315.

1927   58.   S. N. Habisreutinger, L. Schmidt‐Mende and J. K. Stolarczyk,
1928   *Angew. Chem. Int. Ed.*, 2013, **52**, 7372-7408.

1929   59.   W. Ju, A. Bagger, X. Wang, Y. Tsai, F. Luo, T. F. Möller, H. Wang,
1930   J. Rossmeisl, A. S. Varela and P. Strasser, *ACS Energy Lett.*, 2019, **4**, 1663-
1931   1671.

1932   60.   X. Li, Y. Sun, J. Xu, Y. Shao, J. Wu, X. Xu, Y. Pan, H. Ju, J. Zhu and
1933   Y. Xie, *Nat. Energy*, 2019, **4**, 690-699.

1934   61.   A. J. Garza, A. T. Bell and M. Head-Gordon, *ACS Catal.*, 2018, **8**,
1935   1490-1499.

1936   62.   Y. Hori, R. Takahashi, Y. Yoshinami and A. Murata, *J. Phys. Chem.*
1937   *B*, 1997, **101**, 7075-7081.

1938   63.   K. D. Yang, C. W. Lee, K. Jin, S. W. Im and K. T. Nam, *J. Phys.*
1939   *Chem. Lett.*, 2017, **8**, 538-545.

1940   64.   J. Fu, K. Jiang, X. Qiu, J. Yu and M. Liu, *Mater. Today*, 2020, **32**,
1941   222-243.

1942   65.   S. Yu, A. J. Wilson, G. Kumari, X. Zhang and P. K. Jain, *ACS Energy*

Lett., 2017, **2**, 2058-2070.

66. S. Yu, A. J. Wilson, J. Heo and P. K. Jain, *Nano Lett.*, 2018, **18**, 2189-2194.

67. S. Zeng, E. Vahidzadeh, C. G. VanEssen, P. Kar, R. Kisslinger, A. Goswami, Y. Zhang, N. Mahdi, S. Riddell, A. E. Kobryn, S. Gusarov, P. Kumar and K. Shankar, *Appl. Catal. B-Environ.*, 2020, **267**, 118644.

68. A. Li, T. Wang, C. Li, Z. Huang, Z. Luo and J. Gong, *Angew. Chem. Int. Ed.*, 2019, **58**, 3804-3808.

69. M. Xing, Y. Zhou, C. Dong, L. Cai, L. Zeng, B. Shen, L. Pan, C. Dong, Y. Chai, J. Zhang and Y. Yin, *Nano Lett.*, 2018, **18**, 3384-3390.

70. X. Wang, Y. Wang, M. Gao, J. Shen, X. Pu, Z. Zhang, H. Lin and X. Wang, *Appl. Catal. B-Environ.*, 2020, **270**, 118876.

71. S. Feng, J. Zhao, Y. Bai, X. Liang, T. Wang and C. Wang, *J. CO$_2$ Util.*, 2020, **38**, 1-9.

72. K. Wang, Z. Fang, X. Huang, W. Feng, Y. Wang, B. Wang and P. Liu, *Chem. Commun.*, 2017, **53**, 9765-9768.

73. L. Zhao, F. Ye, D. Wang, X. Cai, C. Meng, H. Xie, J. Zhang and S. Bai, *ChemSusChem*, 2018, **11**, 3524-3533.

74. Y. Wang, J. Zhao, Y. Li and C. Wang, *Appl. Catal. B-Environ.*, 2018, **226**, 544-553.

75. A. Li, Q. Cao, G. Zhou, B. V. K. J. Schmidt, W. Zhu, X. Yuan, H. Huo, J. Gong and M. Antonietti, *Angew. Chem. Int. Ed.*, 2019, **58**, 14549-14555.

76. X. Yang, S. Wang, N. Yang, W. Zhou, P. Wang, K. Jiang, S. Li, H. Song, X. Ding, H. Chen and J. Ye, *Appl. Catal. B-Environ.*, 2019, **259**, 118088.

77. Z. Liu, Z. Wang, S. Qing, N. Xue, S. Jia, L. Zhang, L. Li, N. Li, L. Shi and J. Chen, *Appl. Catal. B-Environ.*, 2018, **232**, 86-92.

78. L. Tan, S.-M. Xu, Z. Wang, Y. Xu, X. Wang, X. Hao, S. Bai, C. Ning, Y. Wang, W. Zhang, Y. K. Jo, S.-J. Hwang, X. Cao, X. Zheng, H. Yan, Y. Zhao, H. Duan and Y.-F. Song, *Angew. Chem. Int. Ed.*, 2019, **58**, 11860-11867.

79. T. Ouyang, H.-H. Huang, J.-W. Wang, D.-C. Zhong and T.-B. Lu, *Angew. Chem. Int. Ed.*, 2017, **56**, 738-743.

80. P. Hohenberg and W. Kohn, *Phys. Rev.*, 1964, **136**, B864.

81. Y. Wang, Y. Tian, L. Yan and Z. Su, *J. Phys. Chem. C*, 2018, **122**,

Journal of Materials Chemistry A Accepted Manuscript

1976   7712-7719.

1977   82.   X. Yang, S. Wang, N. Yang, W. Zhou, P. Wang, K. Jiang, S. Li, H.
1978   Song, X. Ding and H. Chen, *Appl. Catal. B-Environ.*, 2019, **259**, 118088.

1979   83.   W. Chen, B. Han, C. Tian, X. Liu, S. Liang, H. Deng and Z. Lin, *Appl.*
1980   *Catal. B-Environ.*, 2019, **244**, 996-1003.

1981   84.   S. S. Tafreshi, A. Z. Moshfegh and N. H. de Leeuw, *J. Phys. Chem.*
1982   *C*, 2019, **123**, 22191-22201.

1983   85.   M. Lu, J. Liu, Q. Li, M. Zhang, M. Liu, J. L. Wang, D. Q. Yuan and
1984   Y. Q. Lan, *Angew. Chem. Int. Ed.*, 2019, **131**, 12392-12397.

1985   86.   A. Hasani, M. Tekalgne, Q. Van Le, H. W. Jang and S. Y. Kim, *J.*
1986   *Mater. Chem. A*, 2019, **7**, 430-454.

1987   87.   M. Naguib, M. Kurtoglu, V. Presser, J. Lu, J. Niu, M. Heon, L.
1988   Hultman, Y. Gogotsi and M. W. Barsoum, *Adv. Mater.*, 2011, **23**, 4248-4253.

1989   88.   X. Li, C. Wang, Y. Cao and G. Wang, *Chem.-Asian J.*, 2018, **13**,
1990   2742-2757.

1991   89.   Y. Yang, Z. Zeng, G. Zeng, D. Huang, R. Xiao, C. Zhang, C. Zhou,
1992   W. Xiong, W. Wang and M. Cheng, *Appl. Catal. B-Environ.*, 2019, **258**, 117956.

1993   90.   P. Srivastava, A. Mishra, H. Mizuseki, K.-R. Lee and A. K. Singh,
1994   *ACS Appl. Mater. Interfaces*, 2016, **8**, 24256-24264.

1995   91.   C. Peng, P. Wei, X. Li, Y. Liu, Y. Cao, H. Wang, H. Yu, F. Peng, L.
1996   Zhang and B. Zhang, *Nano energy*, 2018, **53**, 97-107.

1997   92.   X. Zhang, Z. Zhang, J. Li, X. Zhao, D. Wu and Z. Zhou, *J. Mater.*
1998   *Chem. A*, 2017, **5**, 12899-12903.

1999   93.   T. Cai, L. Wang, Y. Liu, S. Zhang, W. Dong, H. Chen, X. Yi, J. Yuan,
2000   X. Xia and C. Liu, *Appl. Catal. B-Environ.*, 2018, **239**, 545-554.

2001   94.   H. Huang, Y. Song, N. Li, D. Chen, Q. Xu, H. Li, J. He and J. Lu,
2002   *Appl. Catal. B-Environ.*, 2019, **251**, 154-161.

2003   95.   T. Su, Z. D. Hood, M. Naguib, L. Bai, S. Luo, C. M. Rouleau, I. N.
2004   Ivanov, H. Ji, Z. Qin and Z. Wu, *Nanoscale*, 2019, **11**, 8138-8149.

2005   96.   B. Wang, A. Zhou, F. Liu, J. Cao, L. Wang and Q. Hu, *J. Adv. Ceram.*,
2006   2018, **7**, 237-245.

2007   97.   J. Peng, X. Chen, W.-J. Ong, X. Zhao and N. Li, *Chem*, 2019, **5**, 18-
2008   50.

Journal of Materials Chemistry A Accepted Manuscript

2009   98.   B. Wang, M. Y. Wang, F. Y. Liu, Q. Zhang, S. Yao, X. L. Liu and F.
2010 Huang, *Angew. Chem. Int. Ed.*, 2020, **59**, 1914-1918.

2011   99.   S. Cao, B. Shen, T. Tong, J. Fu and J. Yu, *Adv. Funct. Mater.*, 2018,
2012 **28**, 1800136.

2013   100. H. Wang, Y. Wu, T. Xiao, X. Yuan, G. Zeng, W. Tu, S. Wu, H. Y.
2014 Lee, Y. Z. Tan and J. W. Chew, *Appl. Catal. B-Environ.*, 2018, **233**, 213-225.

2015   101. T. Su, R. Peng, Z. D. Hood, M. Naguib, I. N. Ivanov, J. K. Keum, Z.
2016 Qin, Z. Guo and Z. Wu, *ChemSusChem*, 2018, **11**, 688-699.

2017   102. M. Ye, X. Wang, E. Liu, J. Ye and D. Wang, *ChemSusChem*, 2018,
2018 **11**, 1606-1611.

2019   103. X. Xie, N. Zhang, Z.-R. Tang, M. Anpo and Y.-J. Xu, *Appl. Catal. B-*
2020 *Environ.*, 2018, **237**, 43-49.

2021   104. W. Feitknecht and M. Gerber, *Helv. Chim. Acta*, 1942, **25**, 131-137.

2022   105. W. v. Feitknecht, *Helv. Chim. Acta*, 1942, **25**, 555-569.

2023   106. X. Zhao, C. Niu, L. Zhang, H. Guo, X. Wen, C. Liang and G. Zeng,
2024 *Chemosphere*, 2018, **204**, 11-21.

2025   107. Y. Zhu, R. Zhu, M. Wang, B. Wu, X. He, Y. Qian and S. Wang, *Adv.*
2026 *Sci.*, 2016, **3**, 1600229.

2027   108. M. I. Agnel, S. Grangeon, F. Fauth, E. Elkaïm, F. Claret, M. Roulet,
2028 F. Warmont and C. Tournassat, *Environ. Sci. Technol.*, 2020, **54**, 851-861.

2029   109. X. Zhang, L. Yan, J. Li and H. Yu, *J. Colloid Interface Sci.*, 2020,
2030 **562**, 149-158.

2031   110. B. Song, Z. Zeng, G. Zeng, J. Gong, R. Xiao, S. Ye, M. Chen, C. Lai,
2032 P. Xu and X. Tang, *Adv. Colloid Interface Sci.*, 2019, **272**, 101999.

2033   111. L. Lv, Z. Yang, K. Chen, C. Wang and Y. Xiong, *Adv. Energy Mater.*,
2034 2019, **9**, 1803358.

2035   112. L. Mohapatra and K. Parida, *J. Mater. Chem. A*, 2016, **4**, 10744-
2036 10766.

2037   113. S. P. Paredes, M. A. Valenzuela, G. Fetter and S. O. Flores, *J. Phys.*
2038 *Chem. Solids*, 2011, **72**, 914-919.

2039   114. Z.-z. Yang, J.-j. Wei, G.-m. Zeng, H.-q. Zhang, X.-f. Tan, C. Ma, X.-c.
2040 Li, Z.-h. Li and C. Zhang, *Coord. Chem. Rev.*, 2019, **386**, 154-182.

2041   115. N. Ahmed, Y. Shibata, T. Taniguchi and Y. Izumi, *J. Catal.*, 2011,

2042   **279**, 123-135.

2043   116. K. Wang, L. Zhang, Y. Su, D. Shao, S. Zeng and W. Wang, *J. Mater.*
2044   *Chem. A*, 2018, **6**, 8366-8373.

2045   117. T.-T. Kong, J. Huang, X.-G. Jia, W.-Z. Wang and Y. Zhou, *Sci. Rep.*,
2046   2019, **9**, 5659.

2047   118. X. Xiong, Y. Zhao, R. Shi, W. Yin, Y. Zhao, G. I. N. Waterhouse and
2048   T. Zhang, *Sci. Bull.*, 2020, **65**, 987-994.

2049   119. L. A. Wein, H. Zhang, K. Urushidate, M. Miyano and Y. Izumi, *Appl.*
2050   *Surf. Sci.*, 2018, **447**, 687-696.

2051   120. L. Lei, D. Huang, C. Zhou, S. Chen, X. Yan, Z. Li and W. Wang,
2052   *Coord. Chem. Rev.*, 2020, **408**, 213177.

2053   121. Y. Zhao, G. Chen, T. Bian, C. Zhou, G. I. N. Waterhouse, L.-Z. Wu,
2054   C.-H. Tung, L. J. Smith, D. O'Hare and T. Zhang, *Adv. Mater.*, 2015, **27**, 7824-
2055   7831.

2056   122. H. Jiang, K.-i. Katsumata, J. Hong, A. Yamaguchi, K. Nakata, C.
2057   Terashima, N. Matsushita, M. Miyauchi and A. Fujishima, *Appl. Catal. B-*
2058   *Environ.*, 2018, **224**, 783-790.

2059   123. G. Gao, Z. Zhu, J. Zheng, Z. Liu, Q. Wang and Y. Yan, *J. Colloid*
2060   *Interface Sci.*, 2019, **555**, 1-10.

2061   124. M. M.-J. Li, C. Chen, T. c. e. Ayvalı, H. Suo, J. Zheng, I. F. Teixeira,
2062   L. Ye, H. Zou, D. O'Hare and S. C. E. Tsang, *ACS Catal.*, 2018, **8**, 4390-4401.

2063   125. G. Chen, R. Gao, Y. Zhao, Z. Li, G. I. Waterhouse, R. Shi, J. Zhao,
2064   M. Zhang, L. Shang, G. Sheng, X. Zhang, X. Wen, L. Z. Wu, C. H. Tung and
2065   T. Zhang, *Adv. Mater.*, 2018, **30**, 1704663.

2066   126. Z. Wang, S.-M. Xu, L. Tan, G. Liu, T. Shen, C. Yu, H. Wang, Y. Tao,
2067   X. Cao, Y. Zhao and Y.-F. Song, *Appl. Catal. B-Environ.*, 2020, **270**, 118884.

2068   127. Q. Yun, L. Li, Z. Hu, Q. Lu, B. Chen and H. Zhang, *Adv. Mater.*, 2019,
2069   **32**, 1903826.

2070   128. X. Chia and M. Pumera, *Chem. Soc. Rev.*, 2018, **47**, 5602-5613.

2071   129. X. Zhang, Z. Lai, Q. Ma and H. Zhang, *Chem. Soc. Rev.*, 2018, **47**,
2072   3301-3338.

2073   130. R. Geioushy, S. El-Sheikh, I. Hegazy, A. Shawky, S. El-Sherbiny and
2074   A.-H. T. Kandil, *Mater. Res. Bull.*, 2019, **118**, 110499.

Journal of Materials Chemistry A Accepted Manuscript

131. R. Wang, Y. Yu, S. Zhou, H. Li, H. Wong, Z. Luo, L. Gan and T. Zhai, *Adv. Funct. Mater.*, 2018, **28**, 1802473.

132. Z. Xia, Y. Tao, Z. Pan and X. Shen, *Results Phys.*, 2019, **12**, 2218-2224.

133. D. Huang, L. Lei, R. Deng, S. Chen, Z. Li, C. Zhang, W. Wang and K. Wang, *J. Catal.*, 2020, **381**, 175-185.

134. L. Lei, D. Huang, G. Zeng, M. Cheng, D. Jiang, C. Zhou, S. Chen and W. Wang, *Coord. Chem. Rev.*, 2019, **399**, 213020.

135. Y. Li, J. Shi, Y. Mi, X. Sui, H. Xu and X. Liu, *J. Mater. Chem. C*, 2019, **7**, 4304-4319.

136. F. Xu, B. Zhu, B. Cheng, J. Yu and J. Xu, *Adv. Opt. Mater.*, 2018, **6**, 1800911.

137. W. Tu, Y. Li, L. Kuai, Y. Zhou, Q. Xu, H. Li, X. Wang, M. Xiao and Z. Zou, *Nanoscale*, 2017, **9**, 9065-9070.

138. H. Jung, K. M. Cho, K. H. Kim, H.-W. Yoo, A. Al-Saggaf, I. Gereige and H.-T. Jung, *ACS Sustain. Chem. Eng.*, 2018, **6**, 5718-5724.

139. L. Zhang, H. Zhang, C. Jiang, J. Yuan, X. Huang, P. Liu and W. Feng, *Appl. Catal. B-Environ.*, 2019, **259**, 118073.

140. J. Huang, J. Mei, J. Han, H. Liang, W. Wang, B. Dong and L. Cao, *J. Colloid Interface Sci.*, 2019, **556**, 224-231.

141. M. Guo, Z. Xing, T. Zhao, Z. Li, S. Yang and W. Zhou, *Appl. Catal. B-Environ.*, 2019, **257**, 117913.

142. M. R. U. D. Biswas, A. Ali, K. Y. Cho and W.-C. Oh, *Ultrason. Sonochem.*, 2018, **42**, 738-746.

143. J. R. Dunklin, H. Zhang, Y. Yang, J. Liu and J. van de Lagemaat, *ACS Energy Lett.*, 2018, **3**, 2223-2229.

144. S. Li, Z. Zhao, D. Yu, J.-Z. Zhao, Y. Su, Y. Liu, Y. Lin, W. Liu, H. Xu and Z. Zhang, *Nano Energy*, 2019, **66**, 104083.

145. Y. Lin, D. Han, Y. Li, L. Tan, X. Liu, Z. Cui, X. Yang, Z. Li, Y. Liang and S. Zhu, *ACS Sustain. Chem. Eng.*, 2019, **7**, 14982-14990.

146. R. Kumar, D. Das and A. K. Singh, *J. Catal.*, 2018, **359**, 143-150.

147. M. Wang, J. Ioccozia, L. Sun, C. Lin and Z. Lin, *Energy Environ. Sci.*, 2014, **7**, 2182-2202.

2108   148. J. Liu, P. Wang, W. Qu, H. Li, L. Shi and D. Zhang, *Appl. Catal. B-*
2109   *Environ.*, 2019, **257**, 117880.

2110   149. J. Wang, Y. Zhang, X. Wang and W. Su, *Appl. Catal. B-Environ.*,
2111   2019, **268**, 118444.

2112   150. S. Qamar, F. Lei, L. Liang, S. Gao, K. Liu, Y. Sun, W. Ni and Y. Xie,
2113   *Nano Energy*, 2016, **26**, 692-698.

2114   151. L. Wei, C. Yu, Q. Zhang, H. Liu and Y. Wang, *J. Mater. Chem. A*,
2115   2018, **6**, 22411-22436.

2116   152. Z. Jiang, W. Miao, X. Zhu, G. Yang, Z. Yuan, J. Chen, X. Ji, F. Kong
2117   and B. Huang, *Appl. Catal. B-Environ.*, 2019, **256**, 117881.

2118   153. Y. Zhao, N. Liu, S. Zhou and J. Zhao, *J. Mater. Chem. A*, 2019, **7**,
2119   16294-16303.

2120   154. H. Wang, Z. Zeng, P. Xu, L. Li, G. Zeng, R. Xiao, Z. Tang, D. Huang,
2121   L. Tang and C. Lai, *Chem. Soc. Rev.*, 2019, **48**, 488-516.

2122   155. H. Luo, Z. Zeng, G. Zeng, C. Zhang, R. Xiao, D. Huang, C. Lai, M.
2123   Cheng, W. Wang, W. Xiong, Y. Yang, L. Qin, C. Zhou, H. Wang, Y. Zhou and
2124   S. Tian, *Chem. Eng. J.*, 2020, **383**, 123196.

2125   156. R. Li, W. Zhang and K. Zhou, *Adv. Mater.*, 2018, **30**, 1705512.

2126   157. I. I. Alkhatib, C. Garlisi, M. Pagliaro, K. Al-Ali and G. Palmisano,
2127   *Catal. Today*, 2020, **340**, 209-224.

2128   158. S. Tian, C. Zhang, D. Huang, R. Wang, G. Zeng, M. Yan, W. Xiong,
2129   C. Zhou, M. Cheng and W. Xue, *Chem. Eng. J.*, 2020, **389**, 123423.

2130   159. L. Ye, Y. Gao, S. Cao, H. Chen, Y. Yao, J. Hou and L. Sun, *Appl.*
2131   *Catal. B-Environ.*, 2018, **227**, 54-60.

2132   160. C. Zheng, X. Qiu, J. Han, Y. Wu and S. Liu, *ACS Appl. Mater.*
2133   *Interfaces*, 2019, **11**, 42243-42249.

2134   161. Y. Yang, C. Zhang, C. Lai, G. Zeng, D. Huang, M. Cheng, J. Wang,
2135   F. Chen, C. Zhou and W. Xiong, *Adv. Colloid Interface Sci.*, 2018, **254**, 76-93.

2136   162. L. Ye, X. Jin, X. Ji, C. Liu, Y. Su, H. Xie and C. Liu, *Chem. Eng. J.*,
2137   2016, **291**, 39-46.

2138   163. J.-y. Zhu, Y.-p. Li, X.-j. Wang, J. Zhao, Y.-s. Wu and F.-t. Li, *ACS*
2139   *Sustain. Chem. Eng.*, 2019, **7**, 14953-14961.

2140   164. Y. Bai, P. Yang, L. Wang, B. Yang, H. Xie, Y. Zhou and L. Ye, *Chem.*

2141   *Eng. J.*, 2019, **360**, 473-482.

2142   165. Q. Wang, K. Wang, L. Zhang, H. Wang and W. Wang, *Appl. Surf.*
2143 *Sci.*, 2019, **470**, 832-839.

2144   166. X. Wang, K. Maeda, A. Thomas, K. Takanabe, G. Xin, J. M. Carlsson,
2145 K. Domen and M. Antonietti, *Nat. Mater.*, 2009, **8**, 76.

2146   167. W. Wang, C. Zhou, Y. Yang, G. Zeng, C. Zhang, Y. Zhou, J. Yang,
2147 D. Huang, H. Wang, W. Xiong, X. Li, Y. Fu, Z. Wang, Q. He, M. Jia and H.
2148 Luo, *Chem. Eng. J.*, 2021, **404**, 126540.

2149   168. Y. Yang, G. Zeng, D. Huang, C. Zhang, D. He, C. Zhou, W. Wang,
2150 W. Xiong, X. Li, B. Li, W. Dong and Y. Zhou, *Appl. Catal. B-Environ.*, 2020,
2151 **272**, 118970.

2152   169. Y. Yang, X. Li, C. Zhou, W. Xiong, G. Zeng, D. Huang, C. Zhang,
2153 W. Wang, B. Song, X. Tang, X. Li and H. Guo, *Water Res.*, 2020, **184**, 116200.

2154   170. C. Zhang, Y. Zhou, W. Wang, Y. Yang, C. Zhou, L. Wang, L. Lei, D.
2155 He, H. Luo and D. Huang, *Appl. Surf. Sci.*, 2020, **527**, 146757.

2156   171. S. N. Talapaneni, G. Singh, I. Y. Kim, K. AlBahily, A. a. H. Al‑
2157 Muhtaseb, A. S. Karakoti, E. Tavakkoli and A. Vinu, *Adv. Mater.*, 2020, **32**,
2158 1904635.

2159   172. D. He, C. Zhang, G. Zeng, Y. Yang, D. Huang, L. Wang and H. Wang,
2160 *Appl. Catal. B-Environ.*, 2019, **258**, 117957.

2161   173. Y. Yang, C. Zhang, D. Huang, G. Zeng, J. Huang, C. Lai, C. Zhou,
2162 W. Wang, H. Guo and W. Xue, *Appl. Catal. B-Environ.*, 2019, **245**, 87-99.

2163   174. J. Fu, J. Yu, C. Jiang and B. Cheng, *Adv. Energy Mater.*, 2018, **8**,
2164 1701503.

2165   175. G. Dong and L. Zhang, *J. Mater. Chem.*, 2012, **22**, 1160-1166.

2166   176. W. Wang, P. Xu, M. Chen, G. Zeng, C. Zhang, C. Zhou, Y. Yang, D.
2167 Huang, C. Lai and M. Cheng, *ACS Sustain. Chem. Eng.*, 2018, **6**, 15503-15516.

2168   177. S. Tang, X. Yin, G. Wang, X. Lu and T. Lu, *Nano Res.*, 2019, **12**,
2169 457-462.

2170   178. P. Huang, J. Huang, S. A. Pantovich, A. D. Carl, T. G. Fenton, C. A.
2171 Caputo, R. L. Grimm, A. I. Frenkel and G. Li, *J. Am. Chem. Soc.*, 2018, **140**,
2172 16042-16047.

2173   179. Z. Mo, X. Zhu, Z. Jiang, Y. Song, D. Liu, H. Li, X. Yang, Y. She, Y.
2174 Lei and S. Yuan, *Appl. Catal. B-Environ.*, 2019, **256**, 117854.

2175   180. Y. Li, J. Ren, S. Ouyang, W. Hou, T. Petit, H. Song, H. Chen, D. Philo,
2176   T. Kako and J. Ye, *Appl. Catal. B-Environ.*, 2019, **259**, 118027.

2177   181. F. Lin, Y. Zihao and X. Wang, *Chem. Commun.*, 2019, **55**, 8235-8237.

2178   182. J. Fu, K. Liu, K. Jiang, H. Li, P. An, W. Li, N. Zhang, H. Li, X. Xu
2179   and H. Zhou, *Adv. Sci.*, 2019, **6**, 1900796.

2180   183. S. Samanta, R. Yadav, A. Kumar, A. K. Sinha and R. Srivastava, *Appl.*
2181   *Catal. B-Environ.*, 2019, **259**, 118054.

2182   184. J. Wu, Y. Feng, D. Li, X. Han and J. Liu, *Energy*, 2019, **178**, 168-
2183   175.

2184   185. A. Bafaqeer, M. Tahir and N. A. S. Amin, *Appl. Catal. B-Environ.*,
2185   2019, **242**, 312-326.

2186   186. A. Hayat, J. Khan, M. U. Rahman, S. B. Mane, W. U. Khan, M. Sohail,
2187   N. U. Rahman, N. Shaishta, Z. Chi and M. Wu, *J. Colloid Interface Sci.*, 2019,
2188   **548**, 197-205.

2189   187. C. Zhang, W. Wang, A. Duan, G. Zeng, D. Huang, C. Lai, X. Tan, M.
2190   Cheng, R. Wang, C. Zhou, W. Xiong and Y. Yang, *Chemosphere*, 2019, **222**,
2191   184-194.

2192   188. C. Han, N. Zhang and Y.-J. Xu, *Nano Today*, 2016, **11**, 351-372.

2193   189. X. Gong, G. Liu, Y. Li, D. Y. W. Yu and W. Y. Teoh, *Chem. Mater.*,
2194   2016, **28**, 8082-8118.

2195   190. J. Yu, H. Feng, L. Tang, Y. Pang, G. Zeng, Y. Lu, H. Dong, J. Wang,
2196   Y. Liu and C. Feng, *Prog. Mater. Sci.*, 2020, **111**, 100654.

2197   191. S. Sajjad, S. A. Khan Leghari and A. Iqbal, *ACS Appl. Mater.*
2198   *Interfaces*, 2017, **9**, 43393-43414.

2199   192. T.-F. Yeh, J. Cihlář, C.-Y. Chang, C. Cheng and H. Teng, *Mater.*
2200   *Today*, 2013, **16**, 78-84.

2201   193. Y. Zhu, S. Murali, W. Cai, X. Li, J. W. Suk, J. R. Potts and R. S. Ruoff,
2202   *Adv. Mater.*, 2010, **22**, 3906-3924.

2203   194. Y. Liu, B. Sajjadi, W.-Y. Chen and R. Chatterjee, *Fuel*, 2019, **247**,
2204   10-18.

2205   195. C. Bie, B. Zhu, F. Xu, L. Zhang and J. Yu, *Adv. Mater.*, 2019, **31**,
2206   1902868.

2207   196. J. Cai, J. Chen, P. Zeng, Z. Pang and X. Kong, *Chem. Mater.*, 2019,

2208   **31**, 3729-3735.

2209   197. S.-H. Liu, J.-S. Lu, Y.-C. Pu and H.-C. Fan, *J. CO₂ Util.*, 2019, **33**,
2210   171-178.

2211   198. J. Meng, Q. Chen, J. Lu and H. Liu, *ACS Appl. Mater. Interfaces*,
2212   2018, **11**, 550-562.

2213   199. X. Wang, Q. Li, C. Zhou, Z. Cao and R. Zhang, *J. Colloid Interface*
2214   *Sci.*, 2019, **554**, 335-343.

2215   200. Y. Zhao, Y. Wei, X. Wu, H. Zheng, Z. Zhao, J. Liu and J. Li, *Appl.*
2216   *Catal. B-Environ.*, 2018, **226**, 360-372.

2217   201. Y. Tang, X. Hu and C. Liu, *Phys. Chem. Chem. Phys.*, 2014, **16**,
2218   25321-25329.

2219   202. M. Xu, X. Hu, S. Wang, J. Yu, D. Zhu and J. Wang, *J. Catal.*, 2019,
2220   **377**, 652-661.

2221   203. D. V. Shtansky, K. L. Firestein and D. V. Golberg, *Nanoscale*, 2018,
2222   **10**, 17477-17493.

2223   204. C. Zhou, C. Lai, C. Zhang, G. Zeng, D. Huang, M. Cheng, L. Hu, W.
2224   Xiong, M. Chen and J. Wang, *Appl. Catal. B-Environ.*, 2018, **238**, 6-18.

2225   205. G. Zhao, A. Wang, W. He, Y. Xing and X. Xu, *Adv. Mater. Interfaces*,
2226   2019, **6**, 1900062.

2227   206. S. Chen, P. Li, S. Xu, X. Pan, Q. Fu and X. Bao, *J. Mater. Chem. A*,
2228   2018, **6**, 1832-1839.

2229   207. W. Wang, Q. Niu, G. Zeng, C. Zhang, D. Huang, B. Shao, C. Zhou,
2230   Y. Yang, Y. Liu, H. Guo, W. Xiong, L. Lei, S. Liu, H. Yi, S. Chen and X. Tang,
2231   *Appl. Catal. B-Environ.*, 2020, **273**, 119051.

2232   208. V. Tran, R. Soklaski, Y. Liang and L. Yang, *Phys. Rev. B*, 2014, **89**,
2233   235319.

2234   209. B. Li, C. Lai, G. Zeng, D. Huang, L. Qin, M. Zhang, M. Cheng, X.
2235   Liu, H. Yi, C. Zhou, F. Huang, S. Liu and Y. Fu, *Small*, 2019, **15**, 1804565.

2236   210. H. U. Lee, S. C. Lee, J. Won, B.-C. Son, S. Choi, Y. Kim, S. Y. Park,
2237   H.-S. Kim, Y.-C. Lee and J. Lee, *Sci. Rep.*, 2015, **5**, 8691.

2238   211. Q. Zhang, S. Huang, J. Deng, D. T. Gangadharan, F. Yang, Z. Xu, G.
2239   Giorgi, M. Palummo, M. Chaker and D. Ma, *Adv. Funct. Mater.*, 2019, **29**,
2240   1902486.

212. Q. Li, Q. Zhou, L. Shi, Q. Chen and J. Wang, *J. Mater. Chem. A*, 2019, **7**, 4291-4312.

213. G. Zhou, J. Yang, X. Zhu, Q. Li, Q. Yu, W. El-alami, C. Wang, Y. She, J. Qian, H. Xu and H. Li, *J. Energy Chem.*, 2020, **49**, 89-95.

214. J. Li, P. Liu, H. Huang, Y. Li, Y. Tang, D. Mei and C. Zhong, *ACS Sustain. Chem. Eng.*, 2020, **8**, 5175-5183.

215. X. Wang, J. He, J. Li, G. Lu, F. Dong, T. Majima and M. Zhu, *Appl. Catal. B-Environ.*, 2020, **277**, 119230.

216. X. Zhu, S. Huang, Q. Yu, Y. She, J. Yang, G. Zhou, Q. Li, X. She, J. Deng, H. Li and H. Xu, *Appl. Catal. B-Environ.*, 2020, **269**, 118760.

217. J. Low, L. Zhang, T. Tong, B. Shen and J. Yu, *J. Catal.*, 2018, **361**, 255-266.

218. S. Iguchi, Y. Hasegawa, K. Teramura, S. Kidera, S. Kikkawa, S. Hosokawa, H. Asakura and T. Tanaka, *Sustain. Energ. Fuels*, 2017, **1**, 1740-1747.

219. Y. Yang, J. Wu, T. Xiao, Z. Tang, J. Shen, H. Li, Y. Zhou and Z. Zou, *Appl. Catal. B-Environ.*, 2019, **255**, 117771.

220. S. Kumar, M. A. Isaacs, R. Trofimovaite, L. Durndell, C. M. Parlett, R. E. Douthwaite, B. Coulson, M. C. Cockett, K. Wilson and A. F. Lee, *Appl. Catal. B-Environ.*, 2017, **209**, 394-404.

221. S. Tonda, S. Kumar, M. Bhardwaj, P. Yadav and S. Ogale, *ACS Appl. Mater. Interfaces*, 2018, **10**, 2667-2678.

222. Y. Wang, Z. Zhang, L. Zhang, Z. Luo, J. Shen, H. Lin, J. Long, J. C. Wu, X. Fu and X. Wang, *J. Am. Chem. Soc.*, 2018, **140**, 14595-14598.

223. W. Dai, J. Yu, Y. Deng, X. Hu, T. Wang and X. Luo, *Appl. Surf. Sci.*, 2017, **403**, 230-239.

224. H. Shi, S. Long, S. Hu, J. Hou, W. Ni, C. Song, K. Li, G. G. Gurzadyan and X. Guo, *Appl. Catal. B-Environ.*, 2019, **245**, 760-769.

225. H. Shi, S. Long, J. Hou, L. Ye, Y. Sun, W. Ni, C. Song, K. Li, G. G. Gurzadyan and X. Guo, *Chem.-Eur. J.*, 2019, **25**, 5028-5035.

226. W.-K. Jo, S. Kumar and S. Tonda, *Compos. Pt. B-Eng.*, 2019, **176**, 107212.

227. H. Guo, M. Chen, Q. Zhong, Y. Wang, W. Ma and J. Ding, *J. CO$_2$ Util.*, 2019, **33**, 233-241.

Journal of Materials Chemistry A Accepted Manuscript

2275   228. N. Ojha, A. Bajpai and S. Kumar, *Catal. Sci. Technol.*, 2019, **9**, 4598-
2276   4613.

2277   229. J. Zhou, H. Wu, C.-Y. Sun, C.-Y. Hu, X.-L. Wang, Z.-H. Kang and
2278   Z.-M. Su, *J. Mater. Chem. A*, 2018, **6**, 21596-21604.

2279   230. P. Seeharaj, P. Kongmun, P. Paiplod, S. Prakobmit, C. Sriwong, P.
2280   Kim-Lohsoontorn and N. Vittayakorn, *Ultrason. Sonochem.*, 2019, **58**, 104657.

2281   231. A. Kumar, G. Sharma, M. Naushad, T. Ahamad, R. C. Veses and F.
2282   J. Stadler, *Chem. Eng. J.*, 2019, **370**, 148-165.

2283   232. J. O. Olowoyo, M. Kumar, B. Singh, V. O. Oninla, J. O. Babalola, H.
2284   Valdés, A. V. Vorontsov and U. Kumar, *Carbon*, 2019, **147**, 385-397.

2285   233. N. Sadeghi, S. Sharifnia and T.-O. Do, *J. Mater. Chem. A*, 2018, **6**,
2286   18031-18035.

2287   234. Y. Liang, W. Wu, P. Wang, S.-C. Liou, D. Liu and S. H. Ehrman,
2288   *Nano Res.*, 2018, **11**, 4049-4061.

2289   235. D. Mateo, J. Albero and H. García, *Appl. Catal. B-Environ.*, 2018,
2290   **224**, 563-571.

2291   236. D. Mateo, J. Albero and H. García, *Energy Environ. Sci.*, 2017, **10**,
2292   2392-2400.

2293   237. J. M. Thomas, R. Raja and D. W. Lewis, *Angew. Chem. Int. Ed.*, 2005,
2294   **44**, 6456-6482.

2295   238. B. Qiao, A. Wang, X. Yang, L. F. Allard, Z. Jiang, Y. Cui, J. Liu, J.
2296   Li and T. Zhang, *Nat. Chem.*, 2011, **3**, 634.

2297   239. Y. Yang, G. Zeng, D. Huang, C. Zhang, D. He, C. Zhou, W. Wang,
2298   W. Xiong, B. Song, H. Yi, S. Ye and X. Ren, *Small*, 2020, **16**, 2001634.

2299   240. S. Ding, M. J. Hülsey, J. Pérez-Ramírez and N. Yan, *Joule*, 2019, **3**,
2300   2897-2929.

2301   241. J. Di, C. Chen, S.-Z. Yang, S. Chen, M. Duan, J. Xiong, C. Zhu, R.
2302   Long, W. Hao and Z. Chi, *Nat. Commun.*, 2019, **10**, 1-7.

2303   242. Y. Wang, J. Mao, X. Meng, L. Yu, D. Deng and X. Bao, *Chem. Rev.*,
2304   2018, **119**, 1806-1854.

2305   243. T. Tong, B. Zhu, C. Jiang, B. Cheng and J. Yu, *Appl. Surf. Sci.*, 2018,
2306   **433**, 1175-1183.

2307   244. C. Gao, S. Chen, Y. Wang, J. Wang, X. Zheng, J. Zhu, L. Song, W.

2308   Zhang and Y. Xiong, *Adv. Mater.*, 2018, **30**, 1704624.

2309   245.   P. Zhou, Y. Chao, F. Lv, J. Lai, K. Wang and S. Guo, *Sci. Bull.*, 2020,
2310   **65**, 720-725.

2311   246.   J. Di, C. Chen, S.-Z. Yang, S. Chen, M. Duan, J. Xiong, C. Zhu, R.
2312   Long, W. Hao, Z. Chi, H. Chen, Y.-X. Weng, J. Xia, L. Song, S. Li, H. Li and
2313   Z. Liu, *Nat. Commun.*, 2019, **10**, 2840.

2314   247.   L. Shi, X. Ren, Q. Wang, Y. Li, F. Ichihara, H. Zhang, Y. Izumi, L.
2315   Ren, W. Zhou, Y. Yang and J. Ye, *Small*, 2020, **n/a**, 2002356, DOI:
2316   https://doi.org/10.1002/smll.202002356.

2317   248.   R. Zhang, P. Li, F. Wang, L. Ye, A. Gaur, Z. Huang, Z. Zhao, Y. Bai
2318   and Y. Zhou, *Appl. Catal. B-Environ.*, 2019, **250**, 273-279.

2319   249.   K. Homlamai, T. Maihom, S. Choomwattana, M. Sawangphruk and
2320   J. Limtrakul, *Appl. Surf. Sci.*, 2020, **499**, 143928.

2321   250.   C. Liu, B. Yang, E. Tyo, S. Seifert, J. DeBartolo, B. von Issendorff,
2322   P. Zapol, S. Vajda and L. A. Curtiss, *J. Am. Chem. Soc.*, 2015, **137**, 8676-8679.

2323   251.   G. Gao, Y. Jiao, E. R. Waclawik and A. Du, *J. Am. Chem. Soc.*, 2016,
2324   **138**, 6292-6297.

2325   252.   H. Zhang, J. Wei, J. Dong, G. Liu, L. Shi, P. An, G. Zhao, J. Kong,
2326   X. Wang and X. Meng, *Angew. Chem. Int. Ed.*, 2016, **55**, 14310-14314.

2327   253.   M. Wang, J. Liu, C. Guo, X. Gao, C. Gong, Y. Wang, B. Liu, X. Li,
2328   G. G. Gurzadyan and L. Sun, *J. Mater. Chem. A*, 2018, **6**, 4768-4775.

2329   254.   W. Shi, X. Guo, C. Cui, K. Jiang, Z. Li, L. Qu and J.-C. Wang, *Appl.*
2330   *Catal. B-Environ.*, 2019, **243**, 236-242.

2331   255.   W. Tu, Y. Xu, J. Wang, B. Zhang, T. Zhou, S. Yin, S. Wu, C. Li, Y.
2332   Huang and Y. Zhou, *ACS Sustain. Chem. Eng.*, 2017, **5**, 7260-7268.

2333   256.   J. Di, C. Chen, C. Zhu, P. Song, J. Xiong, M. Ji, J. Zhou, Q. Fu, M.
2334   Xu and W. Hao, *ACS Appl. Mater. Interfaces*, 2019, **11**, 30786-30792.

2335   257.   M. Tahir, B. Tahir, M. Nawawi, M. Hussain and A. Muhammad, *Appl.*
2336   *Surf. Sci.*, 2019, **485**, 450-461.

2337   258.   Y. Xu, F. Ge, Z. Chen, S. Huang, W. Wei, M. Xie, H. Xu and H. Li,
2338   *Appl. Surf. Sci.*, 2019, **469**, 739-746.

2339   259.   A. Tabib, W. Bouslama, B. Sieber, A. Addad, H. Elhouichet, M. Férid
2340   and R. Boukherroub, *Appl. Surf. Sci.*, 2017, **396**, 1528-1538.

2341   260. Y. Wang, S. Zhao, Y. Zhang, J. Fang, Y. Zhou, S. Yuan, C. Zhang
2342   and W. Chen, *Appl. Surf. Sci.*, 2018, **440**, 258-265.

2343   261. T. He, C. Zhang, L. Zhang and A. Du, *Nano Res.*, 2019, **12**, 1817-
2344   1823.

2345   262. Y. Zheng, J. Dong, C. Huang, L. Xia, Q. Wu, Q. Xu and W. Yao, *Appl.*
2346   *Catal. B-Environ.*, 2020, **260**, 118220.

2347   263. C. Zhang, C. Lai, G. Zeng, D. Huang, L. Tang, C. Yang, Y. Zhou, L.
2348   Qin and M. Cheng, *Biosens. Bioelectron.*, 2016, **81**, 61-67.

2349   264. M. Sun, B. Lei, J. Li, P. Chen, Y. Zhang and F. Dong, *Nanoscale*,
2350   2019, **11**, 20562-20570.

2351   265. F. Li, P. Zhu, S. Wang, X. Xu, Z. Zhou and C. Wu, *RSC Adv.*, 2019,
2352   **9**, 20633-20642.

2353   266. C. Yu, H. He, Q. Fan, W. Xie, Z. Liu and H. Ji, *Sci. Total Environ.*,
2354   2019, **694**, 133727.

2355   267. C. Feng, L. Tang, Y. Deng, G. Zeng, J. Wang, Y. Liu, Z. Chen, J. Yu
2356   and J. Wang, *Appl. Catal. B-Environ.*, 2019, **256**, 117827.

2357   268. C. Bie, B. Zhu, F. Xu, L. Zhang and J. Yu, *Adv. Mater.*, 2019, **31**,
2358   1902868.

2359   269. W. Wang, Z. Zeng, G. Zeng, C. Zhang, R. Xiao, C. Zhou, W. Xiong,
2360   Y. Yang, L. Lei and Y. Liu, *Chem. Eng. J.*, 2019, **378**, 122132.

2361   270. J. Li, P. Yan, K. Li, J. You, H. Wang, W. Cui, W. Cen, Y. Chu and F.
2362   Dong, *J. Mater. Chem. A*, 2019, **7**, 17014-17021.

2363   271. D. Tan, J. Zhang, J. Shi, S. Li, B. Zhang, X. Tan, F. Zhang, L. Liu, D.
2364   Shao and B. Han, *ACS Appl. Mater. Interfaces*, 2018, **10**, 24516-24522.

2365   272. C. Huang, C. Chen, M. Zhang, L. Lin, X. Ye, S. Lin, M. Antonietti
2366   and X. Wang, *Nat. Commun.*, 2015, **6**, 7698.

2367   273. W. Che, W. Cheng, T. Yao, F. Tang, W. Liu, H. Su, Y. Huang, Q.
2368   Liu, J. Liu and F. Hu, *J. Am. Chem. Soc.*, 2017, **139**, 3021-3026.

2369   274. Y. Huang, D. Li, Z. Fang, R. Chen, B. Luo and W. Shi, *Appl. Catal.*
2370   *B-Environ.*, 2019, **254**, 128-134.

2371   275. K. Wang, J. Fu and Y. Zheng, *Appl. Catal. B-Environ.*, 2019, **254**,
2372   270-282.

2373   276. A. J. Meier, A. Garg, B. Sutter, J. N. Kuhn and V. R. Bhethanabotla,

2374   *ACS Sustain. Chem. Eng.*, 2018, **7**, 265-275.

2375   277. W. Shi, F. Guo, H. Wang, M. Han, H. Li, S. Yuan, H. Huang, Y. Liu
2376   and Z. Kang, *Appl. Catal. B-Environ.*, 2017, **219**, 36-44.

2377   278. A. A. Umar, E. Rahmi, A. Balouch, M. Y. A. Rahman, M. M. Salleh
2378   and M. Oyama, *J. Mater. Chem. A*, 2014, **2**, 17655-17665.

2379   279. S. Liu, J. Yu and M. Jaroniec, *Chem. Mater.*, 2011, **23**, 4085-4093.

2380   280. N. Zhang, C. Gao and Y. Xiong, *J. Energy Chem.*, 2019, **37**, 43-57.

2381   281. M. Shen, L. Zhang, M. Wang, J. Tian, X. Jin, L. Guo, L. Wang and J.
2382   Shi, *J. Mater. Chem. A*, 2019, **7**, 1556-1563.

2383   282. J. Xiong, J. Di, J. Xia, W. Zhu and H. Li, *Adv. Funct. Mater.*, 2018,
2384   **28**, 1801983.

2385   283. J. Di, X. Zhao, C. Lian, M. Ji, J. Xia, J. Xiong, W. Zhou, X. Cao, Y.
2386   She and H. Liu, *Nano Energy*, 2019, **61**, 54-59.

2387   284. J. Low, J. Yu, M. Jaroniec, S. Wageh and A. A. Al‐Ghamdi, *Adv.*
2388   *Mater.*, 2017, **29**, 1601694.

2389   285. Z. Kong, X. Chen, W.-J. Ong, X. Zhao and N. Li, *Appl. Surf. Sci.*,
2390   2019, **463**, 1148-1153.

2391   286. W.-K. Jo, S. Kumar, S. Eslava and S. Tonda, *Appl. Catal. B-Environ.*,
2392   2018, **239**, 586-598.

2393   287. J. Sun, H. Zhang, L.-H. Guo and L. Zhao, *ACS Appl. Mater. Interfaces*,
2394   2013, **5**, 13035-13041.

2395

A table of contents entry
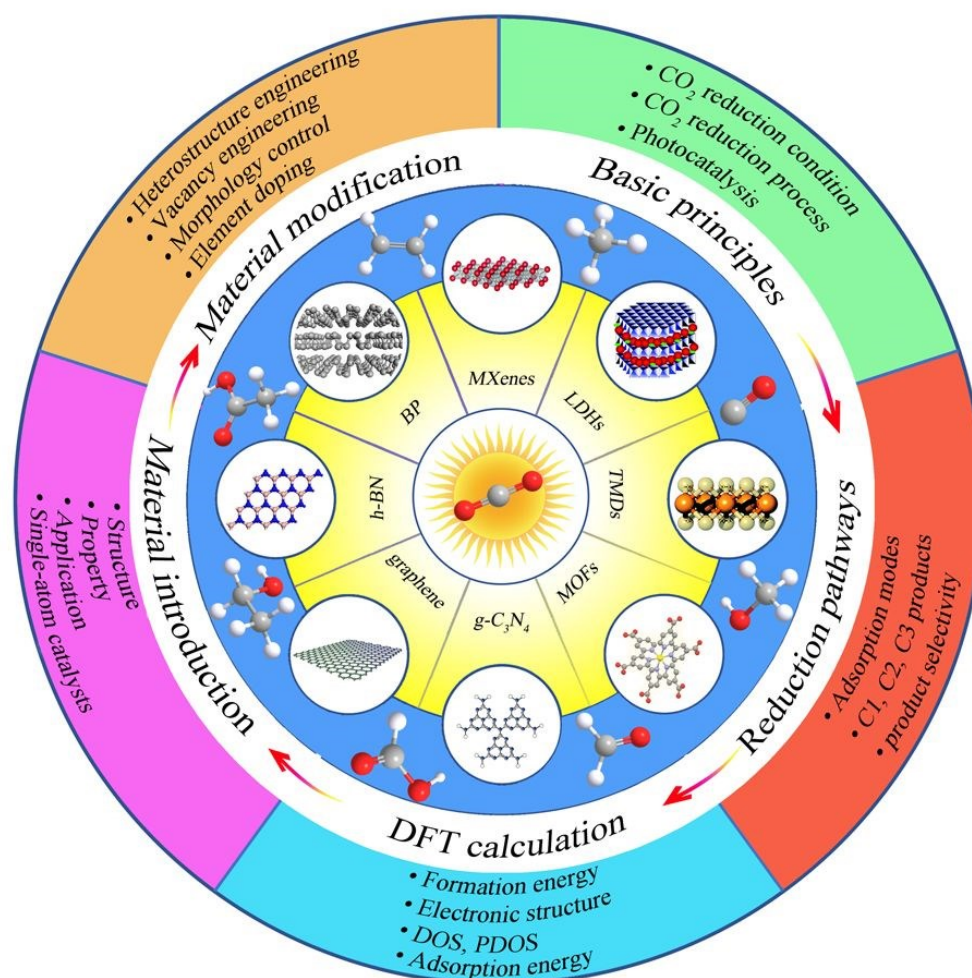
Graphical Abstract

This review systematically summarizes the recent advances in two-dimensional nanomaterials for photocatalytic reduction of CO_2 and its related mechanisms.